C. R. Physique 20 (2019) 92–128

Contents lists available at ScienceDirect

Comptes Rendus Physique

www.sciencedirect.com

The new International System of Units / Le nouveau Système international d'unités

The ampere and the electrical units in the quantum era

L'ampère et les unités électriques à l'ère quantique

Wilfrid Poirier*, Sophie Djordjevic, Félicien Schopfer, Olivier Thévenot

Laboratoire national de métrologie et d'essais, 29, avenue Roger-Hennequin, 78197 Trappes, France

ARTICLE INFO

Article history:
Available online 6 May 2019

Keywords:
Quantum electrical standards
Josephson effect
Quantum Hall effect
Single-electron tunneling
Volt
Ohm
Ampere

Mots-clés :
Étalons électriques quantiques
Effet Josephson
Effet Hall quantique
Effet tunnel monoélectronique
Volt
Ohm
Ampère

ABSTRACT

By fixing two fundamental constants from quantum mechanics, the Planck constant h and the elementary charge e, the revised "Système international" (SI) of units endorses explicitly quantum mechanics. This evolution also highlights the importance of this theory that underpins the most accurate realizations of the units. From 20 May 2019 onwards, the new definitions of the kilogram and of the ampere, based on fixed values of h and e, respectively, will particularly impact the electrical metrology. The Josephson effect (JE) and the quantum Hall effect (QHE), used to maintain voltage and resistance standards with unprecedented reproducibility since 1990, will henceforth provide realizations of the volt and the ohm without the uncertainties inherited from the older electromechanical definitions. More broadly, the revised SI will support the exploitation of quantum effects to realize the electrical units, to the benefit of end-users. Here, we review the state-of-the-art of quantum standards and discuss further applications and perspectives in electrical metrology.

RÉSUMÉ

En fixant deux constantes fondamentales de la mécanique quantique, la constante de Planck h et la charge élémentaire e, le « Système international » (SI) d'unités révisé prend explicitement en considération la mécanique quantique. Cette évolution souligne également l'importance de cette théorie, qui sous-tend les réalisations les plus exactes des unités. À partir du 20 mai 2019, les nouvelles définitions du kilogramme et de l'ampère, établies à partir des valeurs fixées de h et de e, respectivement, auront un impact particulier sur la métrologie électrique. L'effet Josephson (JE) et l'effet Hall quantique (QHE), utilisés pour conserver les étalons de tension et de résistance avec une reproductibilité sans précédent depuis 1990, permettront désormais de réaliser le volt et l'ohm sans les incertitudes héritées des anciennes définitions électromécaniques. De manière plus générale, le SI révisé soutiendra l'exploitation des effets quantiques pour réaliser les unités électriques, et ce,

* Corresponding author.
E-mail address: wilfrid.poirier@lne.fr (W. Poirier).

https://doi.org/10.1016/j.crhy.2019.02.003

au bénéfice des utilisateurs. Nous passons en revue ici l'état de l'art actuel des étalons quantiques et discutons les nouvelles applications et perspectives en métrologie électrique.

Table 1
Definitions of the kilogram, the ampere, the volt, the ohm and the farad before 20 May 2019.

Units	Definitions
kilogram (kg)	The kilogram is the unit of mass; it is equal to the mass of the international prototype of the kilogram.
ampere (A)	The ampere is that constant current which, if maintained in two straight parallel conductors of infinite length, of negligible circular cross-section, and placed 1 m apart in vacuum, would produce between these conductors a force equal to 2×10^{-7} newton per meter of length.
volt (V)	The volt is the potential difference between two points of a conducting wire carrying a constant current of 1 ampere, when the power dissipated between these points is equal to 1 watt.
ohm (Ω)	The ohm is the electric resistance between two points of a conductor when a constant potential difference of 1 volt, applied to these points, produces in the conductor a current of 1 ampere, the conductor not being the seat of any electromotive force.
farad (F)	The farad is the capacitance of a capacitor between the plates of which there appears a potential difference of 1 volt when it is charged by a quantity of electricity of 1 coulomb.

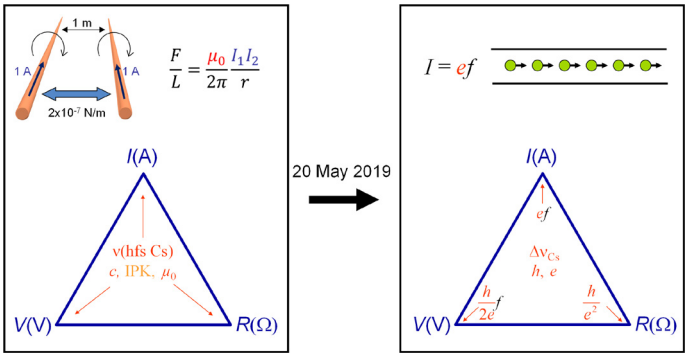

Fig. 1. Top left: schematic of the ampere definition based on Ampere's force law and μ_0. Bottom left: illustration of the link between the electrical units and the unperturbed ground-state hyperfine transition frequency of the cesium 133 atom (noted ν(hfs Cs) before 20 May 2019), IPK (International Prototype of the Kilogram), c (light velocity in vacuum), and μ_0 (magnetic constant of vacuum). Top right: schematic of the ampere definition based on the elementary charge e. Bottom right: illustration of the link of electrical units to $\Delta\nu_{Cs}$ (notation that replaces ν(hfs Cs) after 20 May 2019), h (Planck constant), and e (the elementary charge), where f is the frequency.

1. Ampere definition: from electromechanics to quantum mechanics

1.1. Ampere and the hierarchy of electrical units

In 1948, a new definition of the unit of electrical current, based on Ampere's force law, was established on the occasion of the 9th General Conference of Weight and Measurements (CGPM). Funded on the theory of electromagnetism, this definition, reported in Table 1, fixes the exact value of the attractive force experienced by two current carrying wires in an ideal situation (Fig. 1, left). Doing so, the value of the magnetic constant of vacuum $\mu_0 = 4\pi \times 10^{-7}$ N/A^2 is fixed. It was confirmed in the "Système international d'unités" [1], adopted at the 11th CGPM, and maintained since then [2]. Let us remark that this definition therefore bounds the unit ampere to the unit newton, hence to the kilogram, the meter, and the second. It results that all electrical units depend on the mechanical units, as highlighted by the definitions in Table 1 and illustrated by Fig. 1 (left).

The ampere definition describes a though experiment, and the closest implementation of this experiment is the ampere balance [3]. It consists in comparing the weight of a mass in the gravitational field with the magnetic force that is exerted between two coils supplied by a current. The accuracy of the ampere achieved using the ampere balance was limited by the measurement of the mechanical dimensions from which the electromagnetic force is computed. Relative measurement uncertainties [3] were not better than a few parts in 10^6.

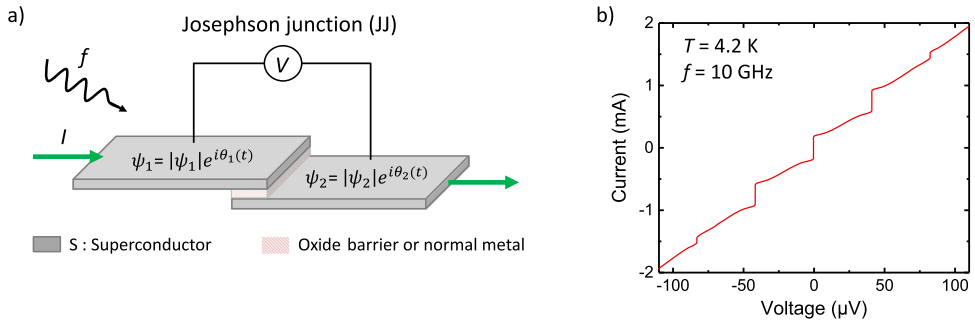

Fig. 2. (a) Schematic of a Josephson junction formed by two superconducting electrodes (S) separated by an oxide barrier (I) or a thin layer of normal metal (N), irradiated by an external microwave source of frequency f. (b) I–V characteristic of two SINIS Josephson junctions in series at 4.2 K and submitted to an external frequency of 10 GHz. Shapiro steps appear in the I–V characteristic at multiple integer of $2f/K_J \sim 40$ μV.

An alternative route [4–7] for improving the accuracy of realization of electrical units was to implement the farad instead of the ampere by exploiting the link of the electric constant of vacuum ϵ_0 to μ_0 and the velocity of light in vacuum $c^2 = 1/\mu_0\epsilon_0$. The farad can indeed be accurately realized from ϵ_0 and the meter using a calculable standard of capacitance [8,4,9,10]. This device is based on a robust theorem [11] derived by A. Thompson and D. Lampard, which stipulates that, in a cylindrical system made of four electrodes of infinite lengths, the two linear cross-capacitances are linked by a universal relationship only dependent on the exact electric constant ϵ_0. For a device based on four cylindrical electrodes, the linear cross-capacitance is equal to $\gamma = \frac{\epsilon_0 \ln(2)}{\pi} \simeq 1.95$ pF/m. The interest of this route was reinforced when the velocity of light c was fixed at the value of 299 792 458 m·s^{-1} to define the meter from the second s in 1983. Doing so, ϵ_0 was also fixed at an exact value. Realizations of the farad using Thompson–Lampard calculable capacitance standards have been achieved with uncertainties [6,10,12] of a few parts in 10^8. The ohm was then realized from impedance comparisons. To complete the chain of electrical units, the volt was also realized from ϵ_0 and mechanical units using the volt balance [13,14]. This experiment compares the weight of a mass in the gravitational field with the electrostatic force occurring between the two electrodes of a capacitance between which a voltage is applied. So, the volt was realized with uncertainties of a few parts in 10^7. Until today, realization uncertainties of the electrical units have hardly changed. Although the Josephson effect and the quantum Hall effect have revolutionized the traceability of voltage and resistance measurements, the realizations of the volt and of the ohm have remained limited by the electromagnetic definition of the ampere. The adoption at the 26th CGPM of the revised SI [15–18] based on constants of nature, and particularly the new definition of the ampere based on the elementary charge will disconnect the electrical units from the mechanical ones (Fig. 1, right). This evolution will rule out the previous limits and this will have a direct impact on the accuracy of the realizations of the electrical units from 20 May 2019, the date of implementation of the revised SI.

1.2. The quantum revolution

In the 20th century, quantum mechanics brings a new description of the reality, *i.e.* the physics of particles, fields, and solids. Relying on the indistinguishability of particles in quantum mechanics, the formalism of the second quantization was developed to describe many-body systems [19], in particular crystalline solids where electrons occupy Bloch states satisfying the crystal periodicity [20,21]. Beyond the description of energy bands, one famous success of the quantum theory of solids is the BCS (Bardeen–Cooper–Schrieffer) theory [22] of the superconductivity, which is explained by the condensation of Cooper pairs. This has opened the way to the discovery of the Josephson effect [23] a few years after. In the 1980s, the solid-state quantum physics is then used to describe electronic transport properties in small devices at low temperatures such as the quantization of the conductance in electronic conductors [24,25], the wave function localization by disorder [26, 27], and the Coulomb blockade [28]. The first two are essential for the description of the quantum Hall effect [29], while the last underpins the single electron tunneling [30].

1.3. The Josephson effect

The ac Josephson effect has been predicted by Brian Josephson in 1962 [31]. It manifests itself as quantized voltage steps in the dc current–voltage (I–V) characteristic of two weakly coupled superconductors submitted to a microwave irradiation of frequency f (Fig. 2a). First demonstrated by Shapiro in 1963 [32], the quantized steps appear at $V_n = nf/K_J$, where n is an integer and $K_J \equiv 2e/h$ is the Josephson constant (Fig. 2b).

Josephson equations. The Josephson effects are a consequence of the existence of a macroscopic coherent quantum state in the superconductors. The BCS theory [22] states that, due to a weak attractive interaction, the electrons near the Fermi surface bind into Cooper pairs, and form a condensate sharing a macroscopic wave function $\psi = |\psi| e^{i\theta}$. The macroscopic properties of the superconducting state like the Meissner effect or the quantization of flux are related to the existence of

the phase θ of the macroscopic wave function, which is maintained over macroscopic distances and hence is responsible for the long-range order. The BCS ground state is a phase coherent linear combination of states with different number of pairs, in which the phase and the number of pairs are related by an uncertainty relation. The macroscopic number of pairs participating in the superconducting state explains the well-defined phase. The Josephson effects appear when the phase locking of the pairs is weakened, *i.e.* when Cooper pairs can be transferred between the two superconducting regions called a Josephson junction (JJ).

Considering a tunnel junction between two superconducting electrodes, Josephson showed, by using second-order perturbation theory in the tunneling Hamiltonian, that a current of Cooper pairs flows in the junction and is related to the phase difference $\varphi = \theta_2 - \theta_1$ of the superconducting wavefunctions on each side of the tunnel barrier (Fig. 2a):

$$I_s = I_c \sin\varphi \tag{1}$$

where I_c is the critical current. This equation states that a dc supercurrent flows with no voltage drop when the phases are time independent.

The ac Josephson effect relates the time dependence of the phase φ to the voltage drop V between the two superconductors:

$$\frac{d\varphi}{dt} = \frac{2eV}{\hbar} \tag{2}$$

Combining the two Eqs. (1) and (2), the supercurrent oscillates at a frequency $f_J = \frac{2eV}{h}$ in the presence of a voltage difference. It can be interpreted as the emission of a photon of energy hf_J when the pair undergoes the energy change of $2eV = 2\Delta\mu$ (where $\Delta\mu$ is the electrochemical potential difference between the two superconductors).

Observation of the ac Josephson effect. In order to observe this effect, Josephson proposed to modulate the Josephson oscillation frequency by biasing the junction with a dc voltage and an external microwave voltage of frequency f, such that $V(t) = V_{dc} + V_{ac}\cos(2\pi f t)$. In that case, the Josephson current can be analyzed in terms of Bessel functions. At the condition, $V_{dc} = n\frac{\hbar}{2e}f$, the current has a dc component that extends over an amplitude $\Delta I_n = 2I_c|J_n(2eV_{ac}/hf)|$, where J_n is the nth order Bessel function. Hence the synchronization of the Josephson oscillation with the external frequency gives rise to constant voltage steps in the dc I–V characteristic, as illustrated in Fig. 2b.

Moreover, it is important to note that the time integral of a voltage pulse $V(t)$ across a Josephson junction, $\int V\,dt = n\frac{h}{2e}$, is quantized in multiples of the quantum of flux in the superconductor $\Phi_0 = h/2e = 2.067 \times 10^{-15}$ V·s^{-1}, so that the Shapiro steps, $V_n \equiv n\Phi_0 f$, can be interpreted as n quantized voltage pulses per period of the external signal. Furthermore, when biased by a current pulse of appropriate amplitude and width, a voltage pulse of quantized area can be generated. We will see in Section 2.1.3 that the precise control of the timing of individual pulses is another way to synthesize quantized voltages.

Dynamics of the Josephson junctions. To describe the dynamics of a realistic Josephson junction (JJ), current components other than the supercurrent must be taken into account. It is usually done in the frame of the resistively and capacitively shunted junction (RCSJ) model or Stewart–McCumber model [33,34], where the JJ is represented by an ideal Josephson element, obeying Eqs. (1) and (2), which is shunted by a resistance R and a capacitance C, as depicted in Fig. 3a. In the presence of an external current source, the bias current, I, is equal to the sum of the currents in the three parallel channels. It results that the behavior of the JJ is governed by the following second-order non-linear equation for φ:

$$I = \frac{\hbar C}{2e}\frac{d^2\varphi}{dt^2} + \frac{\hbar}{2eR}\frac{d\varphi}{dt} + I_c\sin\varphi \tag{3}$$

For small phase differences ($\varphi \ll 1$), $\sin\varphi \backsim \varphi$; the problem becomes linear and similar to a parallel RLC resonator, where the Josephson element can be identified with the kinetic inductance $L_J = \hbar/2eI_c$. The resonant angular frequency of the circuit is $\omega_p = 2\pi f_p = (L_J C)^{-1/2}$, where f_p is the plasma frequency. Another important parameter is the characteristic angular frequency $\omega_c = 2\pi f_c = R/L_J = \frac{2e}{\hbar}I_c R$. The quality factor Q is given by $Q = \omega_p RC$. The latter is related to the well-known McCumber parameter β by $Q^2 = \beta$. By noting that Eq. (3) for the phase is similar to the equation of the damped motion of a particle in a tilted washboard potential (the capacitance and the resistance playing the role of the mass and the damping term respectively), β is often used to characterize the damping of the JJ: $\beta \leq 1$ corresponds to the case of overdamped JJ and $\beta \gg 1$ to the case of underdamped JJ.

The I–V characteristics under microwave irradiation can be calculated by assuming that the junction is driven by a current source with dc and rf components: $I = I_0 + I_1\sin 2\pi f$. The amplitude of the constant-voltage steps, ΔI_n, can be expressed in terms of Bessel functions, as in the case of a voltage-biased JJ, if the rf voltage across the JJ is approximately sinusoidal, *i.e.* when most of the rf current flows in the linear elements rather than in the Josephson element. These limiting cases are useful for the design of the different Josephson voltage standards (see Section 2.1) [37,36,38]; however, in most of the realistic cases, numerical calculations are needed to reproduce the wide variety of experimental I–V characteristics

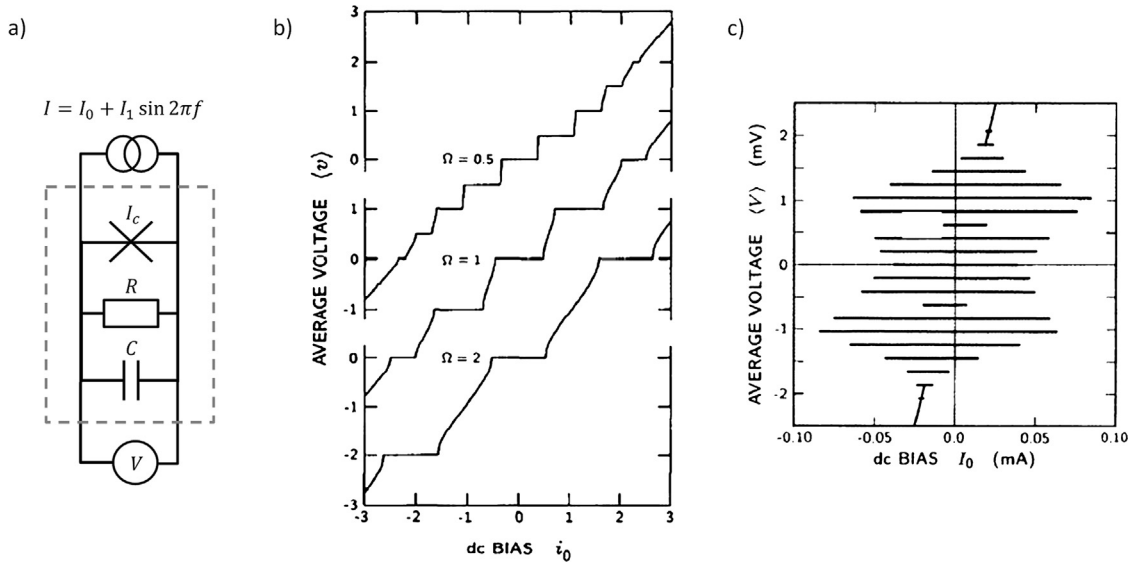

Fig. 3. I–V characteristics calculated within the Stewart–McCumber model: a) Schematic diagram of the current driven, resistively and capacitively shunted junction (RCSJ) model. b) Three I–V characteristics calculated in the limit of the resistively shunted junction model (RSJ) ($C = 0$ and $\beta = 0$). The y-axis is the average voltage in units of the characteristic voltage I_cR, and the x-axis is the dc current relative to I_c ($i_0 = I_0/I_c$). The three different curves correspond to three values of $\Omega = f/f_c = 0.5, 1$ and 2 for three values $i_1 = I_1/I_0 = 1.19, 1.70$, and 3.00, chosen respectively to simultaneously maximize the widths of the $n = 0$ and $n = 1$ steps. Reprinted from ref. [35], with the permission of AIP. c) I–V characteristic calculated in the limit of highly hysteretic JJ for $\beta = 200$ ($I_c = 0.2$ mA, $R = 100\ \Omega$, $C = 20$ pF, $I_1 = 16$ mA, $f_1 = 100$ GHz). Zero-current crossing steps are visible. Adapted from ref. [36].

under microwave irradiation illustrated in Fig. 3b and Fig. 3c. For overdamped JJs, the displacement current in the capacitance can be neglected, the I–V characteristics are non-hysteretic as demonstrated in the simulations done by Kautz [35] (Fig. 3b). There, the rf components are adjusted to optimize simultaneously the amplitude of the $n = 0$ and $n = 1$ steps. For underdamped JJ, the I–V characteristics can be highly hysteretic with the first few constant-voltage steps crossing the zero-current axis if the current through the capacitance is the dominant one, as illustrated in Fig. 3c [36].

Universality of the Josephson effect. Although the prediction of the Josephson effects was done for tunnel junctions, they can be observed for a very wide range of 'weak links'. The universality of the relation has been tested early after the discovery of the effect at some parts in 10^8 [39]. These measurements were improved in the 1980s by Tsai and coworkers [40] and reached a relative uncertainty of 2 parts in 10^{16} by comparing different types of junction (Nb–Cu–Nb junction to an In microbridge). The lowest uncertainty has been achieved with two similar junctions to 3 parts in 10^{19} [41]. This gives a very high confidence that the correction to the frequency-to-voltage relation might be very small if any. In parallel, several theoretical works justified the universal character of the relation in a superconducting ring interrupted by a barrier [42–44] and the absence of corrections to a level of 10^{-20} [45].

Towards the Josephson voltage standards. Since a Josephson junction acts as a perfect frequency-to-voltage converter based on fundamental constants, it was soon proposed to use these steps to improve the voltage standards [46–48], taking advantage of the high accuracy of time references. Today, microwave sources can be referenced and locked to atomic clocks to a level of a few parts in 10^{11}. However, the very small value of the flux quantum fixes the scale of the Shapiro steps to 20 μV at 10 GHz for a single junction. This low value is an obstacle to the development of practical voltage standards for which outputs of 1 V to 10 V are desirable. This challenge has been addressed by the successful development of highly-integrated series arrays of underdamped or overdamped Josephson junctions, which will be described in section 2.1.

1.4. The quantum Hall effect

1.4.1. The effect and its physics

The quantum Hall effect [29], discovered by K. von Klitzing in 1980, occurs in a two-dimensional electron gas (2DEG), like a Hall bar (see Fig. 4a), under a perpendicular magnetic field. As reported in Fig. 4b, it manifests itself by a quantization of the transverse resistance R_H at values R_K/i, where i is an integer and $R_K \equiv h/e^2$ is the von Klitzing constant. Simultaneously, the longitudinal resistance forms minima, $R_{xx} \sim 0$, revealing that the 2DEG is in a dissipationless state.

In a perpendicular magnetic field, the classical motion of an electron of charge $(-e)$ moving in a two-dimension (2D) space is a cyclotron motion that drifts under the application of an electric field. The resistivity tensor is given by:

$$\rho_{xx} = \frac{m^*}{n_s e^2 \tau} \quad \text{and} \quad \rho_{xy} = \frac{B}{n_s e} \tag{4}$$

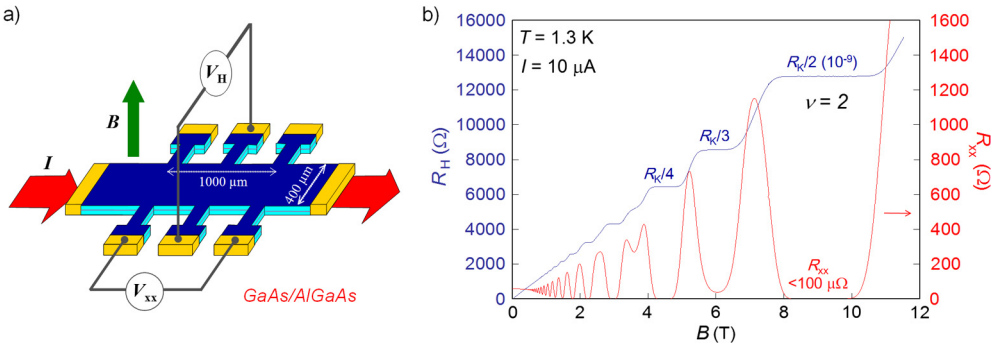

Fig. 4. (a) Schematic of an eight-terminal Hall bar based on a GaAs/AlGaAs heterostructure. (b) Hall resistance, R_H, and longitudinal resistance, R_{xx}, as a function of the magnetic induction B at $T = 1.3$ K.

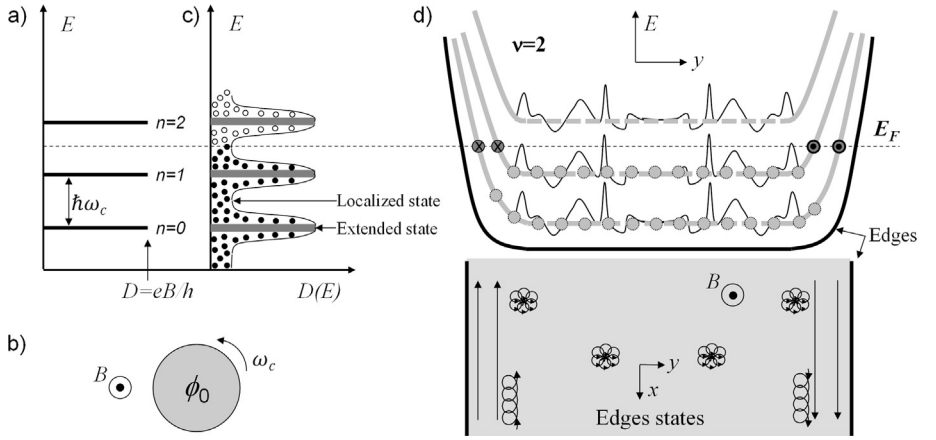

Fig. 5. (a) Quantization of the density of states D(E) in Landau levels in a ballistic 2D conductor. (b) Illustration of the quantization of the cyclotron motion. (c) Density of states in a disordered 2D conductor. (d) Device with edges in the QHE regime (at $\nu = 2$). Landau levels bent by the confining potential (top). Schematic of two edge states and localized states in real space (bottom).

where n_s is the carrier density, m^* is the effective mass, and τ is the scattering time. This classical model explains the Hall effect observable at low magnetic field or high temperature. Moreover, it emphasizes that the Hall resistance of 2D conductors is independent of the dimensions, *i.e.* scale invariant. On the other hand, neither the quantization of the Hall resistance nor the cancellation of the longitudinal resistivity are predicted. To explain these two features of the QHE, a quantum mechanics description must be considered.

Several review papers [49–52] or books [53–56] about the QHE physics can be consulted. The Hamiltonian of a free electron in two dimensions (2D) in the presence of a magnetic field (potential vector A) is given by:

$$H = \frac{1}{2m^*}(P + eA)^2 = \hbar\omega_c(a^+a + 1/2) \tag{5}$$

where $\omega_c = eB/h$ is the cyclotron pulsation and a is a scaling operator obeying $[a^+, a] = 1$. This hamiltonian, gauge invariant, is that of an harmonic oscillator whose energy spectrum is quantized in Landau levels (LL) (Fig. 5a) at values given by:

$$\epsilon_n = \hbar\omega_c(n + 1/2) \tag{6}$$

where n is an integer. The cyclotron motion is quantized (Fig. 5b) and the energy spectrum is highly degenerate with regards to the center of guidance of the cyclotron orbit. It results that the density of states for each LL is eB/h (one spin value) and therefore is equal to the density of flux quanta $n_B = B/\phi_0$. Calculations show that each electron occupies a surface $2\pi l_B^2 = 1/n_B$ in real space, *i.e.* the area crossed by a flux quantum where $l_B = \sqrt{\hbar/eB}$ is the magnetic length. This explains the relationship $n_s = \nu n_B$ in quantized Hall states, where the LL filling factor ν is an integer. The electronic fluid is therefore incompressible and a high energy $\hbar\omega_c$ is required to add an electron.

To explain both the existence of a Hall resistance plateau and the drop to zero of the longitudinal resistance, disorder must be considered. It introduces a spatially varying potential that lifts the Landau level degeneracy (Fig. 5c). This leads to extended states in narrow energy bands centered around ϵ_n, and localized states at energies in between Landau levels. In the high magnetic field limit (or smooth potential), localized states correspond to closed equipotential lines around peaks or deeps of the potential, while delocalized states spread along equipotential lines in valleys of the potential, as illustrated in

Fig. 5d. Only delocalized states can carry current. By varying the LL filling factor ν (variation of B or n_s), the Fermi energy E_F can be continuously changed. While it is located at energies corresponding to localized states, the total net current, and thus the Hall resistance remain constant. Moreover, excitations towards extended states are blocked by the energy gap, which prevents any dissipation and leads to $R_{xx} \sim 0$. Let us note that residual dissipation exists at finite temperature due to conduction through localized states. As the filling factor ν moves closer to a LL energy, electrons experience a localization/delocalization [57,58] transition (divergence of the localization length), which is considered to be a quantum phase transition [59].

To explain the values, $h/\nu e^2$, at which the Hall resistance is quantized, let us consider a real device geometry with edges, as illustrated in Fig. 5d. The confining potential introduced by edges bends the Landau levels. At an integer ν value, the Fermi energy E_F in the bulk intercepts only localized states that do not carry any current. On the other hand, it intercepts LL extended states at edges, which defines an integer number ($\nu = 2$ in Fig. 5d) of one-dimensional (1D) states. The velocity group of these states is reversed from one device edge to the other. Thus, states with opposite momentum are spatially separated, which forbids electron backscattering. It results that these 1D-edges states are ballistic (their transmission is unity). From the scattering theory [24,60] of the electronic transport, the conductance of a 1D ballistic state (one spin) is known to be h/e^2. This is a direct consequence of the Pauli principle combined with the Heisenberg time-energy uncertainty principle [61]. The two-terminal conductance of a Hall conductor is then obtained by simply counting the number of edge-states. Besides, backscattering being canceled, dissipation can only occur in contacts. More generally, the conductance properties in the QHE regime of a system with contacts at given chemical potentials can be obtained from the occupation of edge states [49]. In this framework, the Landauer–Buttiker theory [62,63] describes the conductance of multi-terminals conductors and notably the Hall bar. It notably predicts that the QHE requires phase coherency of the wave-function only at the scale of l_B.

1.4.2. A universal and robust quantum effect

The QHE is a universal quantum effect, which means that the quantized Hall resistance is linked to h/e^2 independently of the two-dimensional conductor considered. The first explanation of the QHE, proposed by Laughlin in 1981, showed that the universal character of the QHE originates from the gauge invariance of the Hamiltonian [64]. More precisely, let us consider a closed 2D ribbon submitted to a perpendicular magnetic field and a transverse electric field. The system being invariant by application of a flux quantum through the ribbon (filled states are simply shifted by one unity if the Fermi energy is in between two Landau levels), the variation of energy ($\Delta U = eV$) has a purely electrostatic origin and is caused by the transfer of one electron from one edge of the ribbon to the other. The expression of the current, $I = \Delta U/\phi_0 = (e^2/h)V$, gave the first explanation of the universal quantized value [51]. This argument was then generalized by Thouless et al. showing that the Hall conductance is a topological invariant [65–67]. It was also demonstrated that neither electron–electron interaction [68] nor the gravitational field [69] leads to any correction. However, one work using quantum electrodynamic calculations reports on a correction to h/e^2 caused by a renormalization of the electric charge by the magnetic field. A tiny relative correction, αB^2, amounting to 10^{-21} for $B = 20$ T, is predicted [70].

The universality and the reproducibility [71] of the von Klitzing constant R_K were proved by showing the agreement of the quantized Hall resistance measured in several two-dimensional semiconductors with relative uncertainties down to a few 10^{-11}. Different devices by the nature of the 2DEG (silicon–MOSFET [72,73], GaAs/AlGAs [74], InGaAs/InP [75], graphene [76,77]), by their electronic properties (carrier density, electronic mobility, filling factor) [73,78,79], and their geometry (Hall bar size) [80] were tested.

1.5. Single-electron tunneling current sources

Single-electron pumps. In the 1990s, the possibility to manipulate a single electron charge has been demonstrated [81] in mesoscopic conductors. Some of these devices, called single-electron pumps, have enabled the control of the transfer of electrons one by one at a rate fixed by an external frequency f_P [82–84], resulting in a current $I = Q f_P$, where $Q \equiv e$. Fig. 6a shows a current step at a value of 1.6 pA that is observed in the I–V characteristic of such a device operating at a frequency of 10 MHz.

The operation of single-electron pumps is based on the manifestation of the charge quantization in a small metallic island isolated by tunnel barriers of capacitance C and resistance R, where Coulomb blockade manifests itself [86]. The transfer of electrons one by one occurs if: 1) the charging energy e^2/C prohibiting the addition of a second electron, as illustrated in Fig. 6b, is larger than the thermal energy $k_B T$ (this requires very low operating temperatures and small tunnel barrier capacitances) and 2) the electron state has an energy thickness δE much smaller than e^2/C, *i.e.* $\delta E \ll e^2/C$. Considering the charging time of the island of the order of RC and the energy-time Heisenberg uncertainty principle, one deduces $\delta E \sim h/(RC)$, which leads to a tunnel resistance $R \gg h/e^2$.

First single-electron tunneling (SET) pumps [82] consisted of several (at least two) small metallic islands in series isolated by tunnel junctions. Each island is capacitively coupled with a voltage generator (gate voltage) synchronized to f_P, which is used to control its charge state. By adjusting carefully the amplitude and the phase of the gate voltages, $n_Q e$ charges can be transferred from island to island at each pumping cycle, where n_Q is the number of charges. This principle is described in Fig. 6c. The output current delivered by these devices is therefore ideally equal to $I_P = n_Q e f_P$. A current step forms by varying the polarization voltage of the pump V_P, as reported in Fig. 6a.

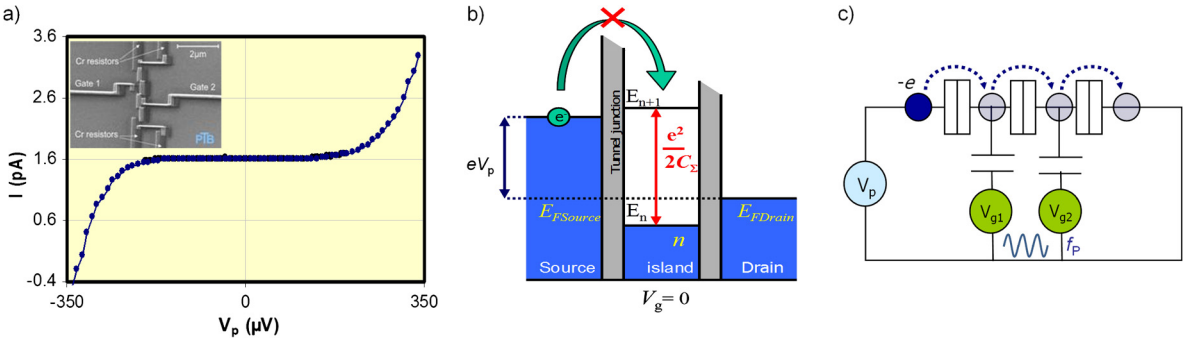

Fig. 6. (a) Example of a current *versus* voltage (I–V) curve showing a 1.6-pA current step obtained with a pumping frequency $f_P = 10$ MHz. SEM picture of a metallic pump fabricated at PTB (by courtesy of PTB). (b) Principle of Coulomb blockade in a single-electron transistor (SET): the charging energy $e^2/2C_\Sigma$ opposes to the addition of an extra electron. Adapted from ref. [85]. (c) Principle of the transfer one by one of electrons in a pump device based on three tunnel-junctions and two islands. The energy states in islands are controlled by AC gate voltages synchronized at a frequency f_P.

Accuracy of metallic single-electron pumps. In a 7-junction device, quantized currents of a few pA have been generated for frequencies in the MHz range and an error rate of charge transfer per cycle as low as 1.5×10^{-8} was measured [87]. Given the low current values, the accuracy of such devices was determined by measuring the voltage at the terminals of a calibrated (in terms of μ_0 or R_K) cryogenic capacitor charged with a precise number of electrons in terms of K_J [88]. The quantization of the current was demonstrated with a relative uncertainty of 9.2×10^{-7} for currents below 1 pA [89]. In a similar experiment, a relative uncertainty of 1.66×10^{-6} was reached with a 5-junction R-pump [90]. The limit in the uncertainty achieved comes from the small currents that theses metallic pumps can accurately generate. Large RC values and serialization of several junctions used to reduce co-tunneling events indeed result in a strong frequency dependence that prevents generating larger currents with accuracy [86,91]. As a trade-off between accuracy and increased current, several alternative quantum current sources have then been proposed [91–93]. They will be discussed in section 3.

1.6. Quantum standards in the SI based on the electromechanical definition of the ampere

The high reproducibility and universality of the JE and the QHE motivated their use to realize the units of voltage and resistance respectively. The development of high-quality 10-V Josephson arrays and GaAs/AlGaAs Hall bars on one side and accurate comparisons bridges on the other side have allowed metrologists, in the late 1980s, to perform accurate calibrations of voltage references and resistors from K_J and R_K, respectively, with relative uncertainties around 10^{-9}. A prerequisite before using the JE and the QHE in metrology was to link the Josephson voltage and the quantum Hall resistance to the volt and the ohm as defined in the SI. This means calibrating K_J and R_K in terms of SI units. In 1990, the Josephson effect and the quantum Hall effect were recommended by the CIPM to maintain the units of voltage and resistance in national metrology institutes (NMIs) and values for the two quantum constants were adopted: $K_J = K_{J-90} \times (1 \pm 4 \times 10^{-7})$ GHz/V [94] and $R_K = R_{K-90}(1 \pm 1 \times 10^{-7})$ Ω [95] where $K_{J-90} = 483\,597.9$ GHz/V and $R_{K-90} = 25\,812.807$ Ω. The uncertainties of determination of these two constants are much larger than the reproducibility of the quantum phenomena. This comes from the definition of the current unit based on Ampere's force law, which imposes the implementation of complex electromechanical experiments to measure K_J (the volt balance) and R_K (the Thompson–Lampard calculable capacitor).

To benefit even so from the high-reproducibility of the Josephson and quantum Hall effects for the traceability of the voltage and resistance measurements, the conventional exact values (without uncertainties), K_{J-90} and R_{K-90}, were recommended by the "Comité international des poids et mesures" (CIPM) [96] as the reference values in calibration certificates based on the implementation of these quantum effects. The voltage and the resistance measurements traceable to K_{J-90} and R_{K-90} give representations, and not realizations in the SI, of the volt and the ohm. It results that the current realized from $(K_{J-90}R_{K-90})^{-1}$ by application of Ohm's law from the representations of the volt and the ohm gives a representation of the ampere (not a realization). These decisions resulted in a major improvement of the reproducibility of the units of voltage and resistance, as realized by national metrology institutes (NMIs). This is highlighted by Fig. 7, which shows a reduction of the relative deviations in resistance measurements between NMIs, from about 10^{-6} before the use of the QHE a) down to 10^{-9} after its recommendation by the CIPM b). The exploitation of the JE led to a similar strong improvement.

However, this artifice, which makes the traceability of electrical measurements advantageous for end-users, is not applicable to experiments where realizations of units, and not representations, are required. This is notably the case of high-precision experiments involving both mechanical measurements and electrical measurements traced to quantum effects: it would indeed be inconsistent to drop out the uncertainties of K_J and R_K, the origin of which is mechanical. To illustrate this difficulty, one can evoke the realization of the farad either from μ_0 using the Thompson–Lampard calculable capacitor or from R_{K-90} using the QHE. Another example, discussed in subsection 4.1, is the Kibble balance experiment, which links the kilogram to electrical units. A main motivation and issue of the revised SI was to get rid of this artifice.

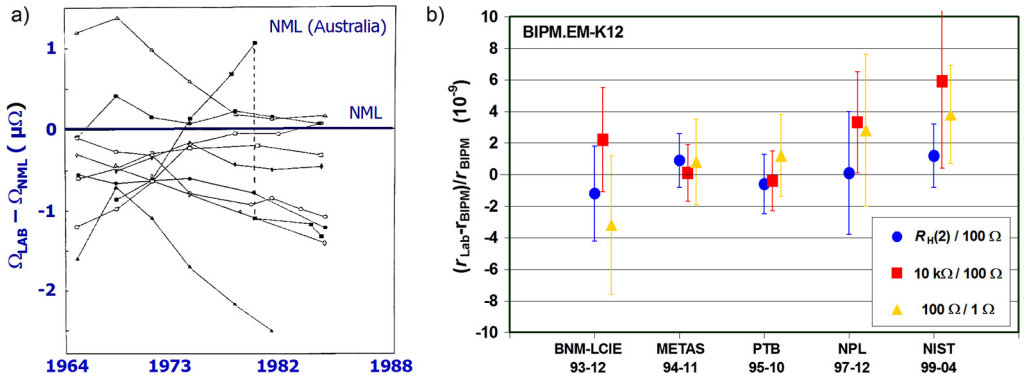

Fig. 7. (a) Deviation in μΩ between realizations of the ohm in several NMIs and NML (Australia) till 1988 [97]. (b) Relative deviations of resistance ratio measurements performed in different NMIs and in BIPM by using the QHE and modern resistance bridges [98]. Reprinted by permission of Springer Nature from ref. [99], ©2009.

Table 2
Definitions of the kilogram and the ampere associated with the fixing of exact values of h and e from 20 May 2019 onwards. The unperturbed ground-state hyperfine transition frequency of the cesium 133 atom $\Delta\nu_{Cs}$ is 9 192 631 770 Hz. Values [101] of h and e were established from the CODATA 2017 adjustment [102].

Units	Definitions
kilogram (kg)	The kilogram, symbol kg, is the SI unit of mass. It is defined by taking the fixed numerical value of the Planck constant h as $6.62607015 \times 10^{-34}$ when expressed in the unit J·s, which is equal to the $kg \cdot m^2 \cdot s^{-1}$, where the meter and the second are defined in terms of c and $\Delta\nu_{Cs}$.
ampere (A)	The ampere, symbol A, is the SI unit of electric current. It is defined by taking the fixed numerical value of the elementary charge e as $1.602176634 \times 10^{-19}$ when expressed in the unit C, which is equal to the A·s, where the second is defined in terms of $\Delta\nu_{Cs}$.

1.7. A new definition of the ampere from the elementary charge

1.7.1. The revised SI

The article "Redefinition of the kilogram: a decision whose time has come" by Mills et al. [15] in 2005 has not only initiated a cogitation about a redefinition of the kilogram without an artefact, but has also crystallized a consensus around a major evolution of the SI to overpass the limits imposed by the definitions of other units: the ampere, the kelvin, the mole. Concerning the ampere, the goal was to find a definition to fully benefit from the high reproducibility and universality of the quantum electrical standards. More generally, the ambition of the revised SI was to take into account modern physics, *i.e.* quantum physics and statistical physics and avoid definitions closely linked to given practical realizations. The revised SI based on fixed fundamental constants ($\Delta\nu_{Cs}$, c, h, e, k, K_{cd}) fulfills these requirements [18,100]. Electrical metrology is directly concerned by the definitions of the kilogram and the ampere based on the constants h and e respectively. They are presented in Table 2.

The setting of this revised SI follows many works aiming at improving the knowledge of fundamental constants before fixing their exact values. The goal was to reduce the measurement uncertainties, not only of c, h, e, and k, but also of the constants K_J, R_K, and Q in order to check the solid-state theory on which quantum electrical standards rely.

1.7.2. Determinations of R_K and α

The von Klitzing constant R_K can be measured through a comparison with the impedance $1/(2\pi f C)$ using a quadrature bridge, where f is the operation frequency and C is a capacitance calibrated from the Thompson–Lampard calculable capacitor that was described before. It is interesting to compare the determinations of R_K with measurements of h/e^2 in order to test the QHE theory. It is equivalent to compare the determinations of the fine structure constant $\alpha = \frac{\mu_0 c}{2(h/e^2)}$ with the estimations $\alpha = \frac{\mu_0 c}{2R_K}$. Determinations of α can be obtained from measurements of h/m_{at} [m_{at} is an atomic mass (cesium or rubidium atoms)] by atomic interferometry, or measurements of the abnormal magnetic moment of the electron combined with quantum electrodynamic calculations. The results from [103], reported in Fig. 8a, are in agreement with the estimations from R_K, including that of LNE measured with a relative uncertainty of 5.3×10^{-8} using a specific five-electrode calculable capacitor [6]. It results that $R_K = \frac{h}{e^2}(1 + \epsilon_K)$ with $\epsilon_K = (2.2 \pm 1.8) \times 10^{-8}$. This confirms the QHE theory, furthermore supported by universality tests that show that R_K is independent of the 2D material with uncertainties down to a few 10^{-11}. From all data, an accurate value of α is deduced [102]: $\alpha^{-1} = 137.035999139 \times (1 \pm 2.3 \times 10^{-10})$.

1.7.3. Determinations of K_J and h

The K_J constant was initially determined using the volt balance. The uncertainty of measurement of K_J was improved using the Kibble balance (a watt balance) and the R_K value. This experiment consists in measuring the mechanical power

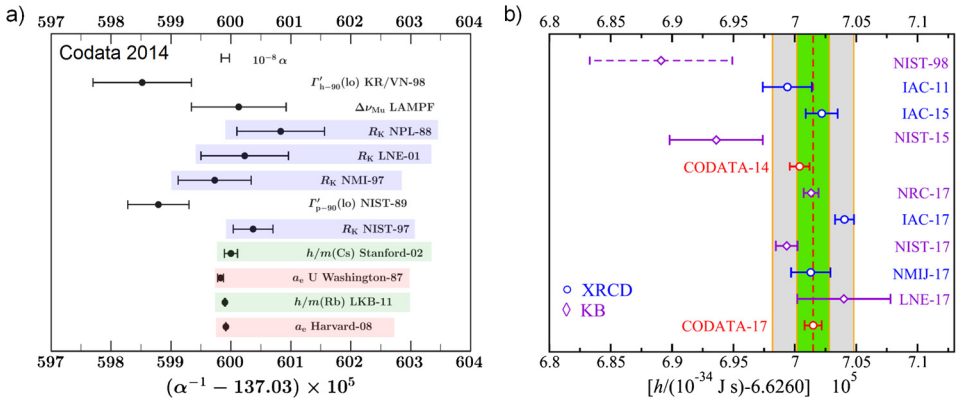

Fig. 8. (a) Determinations of the fine structure constant α: from R_K (highlighted in blue), from h/m by atomic interferometry (highlighted in green), and from the abnormal magnetic moment of the electron a_e using quantum electrodynamic calculations (highlighted in red). Adapted from ref. [103]. (b) Determinations of the Planck constant h using a Kibble balance (KB) or a silicon sphere (XRCD). From ref. [102].

of a mass m moving at velocity v under the gravitational field g in terms of an electric power in a coil calibrated from $1/R_K K_J^2$, which is an estimate of the Planck constant h. The Kibble balance therefore establishes a relationship between the kilogram and h. Its advantage is that the watt does not depend on the ampere's definition, contrary to the volt. This allows us to overcome some technical difficulties, for example the geometric calibration of the coil. Comparing K_J value to its theoretical expectation requires the knowledge of $2e/h$. The latter constant can be determined from h/e^2 and the determination of h from the Avogadro constant N_A. The Planck constant can indeed be deduced from the relationship $h = \frac{cA_r(e)M_u\alpha^2}{2R_\infty N_A}$, where $A_r(e)$ is relative atomic mass of the electron, M_u is the molar mass constant and R_∞ is the Rydberg constant. The Avogadro constant N_A can be determined from the number of atoms in a silicon sphere of volume V_{sphere} and mass m_{sphere}, according to $N_A = \frac{M_{Si}V_{sphere}}{\sqrt{8}d_{220}^3 m_{sphere}}$, where M_{Si} is the silicon molar mass and d_{220} is the inter-atomic distance measured by X-ray diffraction. Here, one can note that the mass can be realized from N_A. Testing the agreement of K_J with $2e/h$ is as comparing determinations of h using the Kibble balance (assuming that QHE and JE theories are valid) and determinations from N_A. Analysis from the CODATA 2014 group demonstrated the absence of significant disagreement between the two determinations of h, reported in Fig. 8b. It was deduced that $K_J = \frac{2e}{h}(1+\epsilon_J)$ with $\epsilon_J = (-0.9 \pm 1.5) \times 10^{-8}$. This result and the universality tests of the JE show that the JE theory could be adopted. The last adjustment of constants carried out by the CODATA 2017 group [102], who considered new results, determined an accurate value of the Planck constant equal to $h = 6.626070150 \times 10^{-34}(1 \pm 1.0 \times 10^{-8})$ J·s. From this value and that of α, the value of the elementary charge obtained is $e = 1.6021766341 \times 10^{-19}\,(1 \pm 5.2 \times 10^{-9})$ C.

1.7.4. Closure of the metrological triangle

This experience, illustrated in Fig. 9a, consists in comparing the realization of the ampere from the frequency by implementing SET devices on one side and by applying Ohm's law to quantum voltage and resistance standards on the other one [30,85]. It leads to the determination of the product of constants $R_K K_J Q$, which is theoretically equal to 2 if $R_K = h/e^2$, $K_J = 2e/h$, and $Q = e$. This is a fundamental test of the consistency of the quantum solid-state physics, where one of the issues is to check that the quasi-particles either handled in the SET quantum dot, or flowing along the sample QHE edge or in the Cooper pair have the same elementary charge. Any deviation from the expected value would question a part of quantum mechanics. In practice, this direct comparison implementing the three quantum standards together has never been performed. Instead, the current generated by SET devices was measured by using a secondary resistor (or capacitor) calibrated from R_K, whose voltage at its terminals was compared to a Josephson voltage reference. Among the many works that have reported measurements of the output current of SET devices, only three of them have claimed the closure of the metrological triangle [89,105,106]. The main reason is that determining $R_K K_J Q$ requires that the expected number of charges n_Q is really transferred with accuracy at each cycle. Some authors consider that there is no proof of that for recent non-adiabatic SET devices, described in section 3.1, and that an independent measurement of n_Q is required to make a determination of Q. Thus, the three determinations were based on the use of metallic SET pumps, the physics of which was well understood and, above all, it was demonstrated in a 7-junction device that the error rate of charge transfer per cycle was as low as 1.5×10^{-8} [87]. Moreover, some quantization criteria, such as observation of a linear frequency dependence of the current and of a minimization of co-tunneling events by setting the biasing voltage, could be used to confirm the quantization state. Using a measurement method based on the charging of a calibrated cryogenic capacitor, research works [89] and [106] achieved closure of the metrological triangle with relative uncertainties of 9.2×10^{-7} and 1.66×10^{-6}, respectively. In work [105] from the LNE, the SET device current is amplified using a CCC [107] before measurement (Fig. 9b), and the uncertainty achieved is 1.3×10^{-5}. Although confirming solid-state physics, these works have not contributed to an estimation of the elementary charge e from R_K and K_J in the CODATA calculations because of the too large uncertainties achieved.

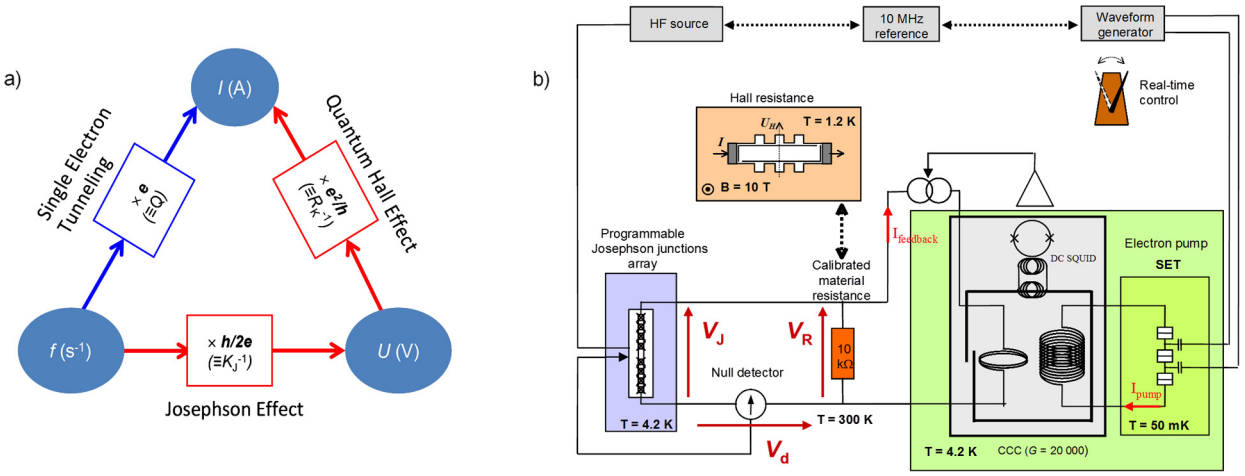

Fig. 9. (a) Illustration of the metrological triangle [30] and realization of the current I from frequency f, either by using the relation $I = Qf$ in the single-electron tunneling effect, or by using Ohm's law associated with the Josephson and the quantum Hall effects, $I = n(R_K K_J)^{-1} f$, where n is an integer. Adapted from ref. [104]. (b) Schematic of the LNE experiment to close the metrological triangle [85,105]. The current generated by a metallic pump I_{pump} is amplified by a factor 20 000 using a cryogenic current comparator (CCC). This amplified current feeds a calibrated resistor from the QHE. The voltage drop V_R at resistance terminals is measured by comparison with a Josephson reference voltage V_J. Adapted from ref. [105].

1.7.5. Impact of the new definition of the ampere

Exact values of h and e, chosen to establish the new SI definitions and reported in Table 2, were obtained by truncating the digits of the values determined in the previous SI. One advantage of the new definitions is that they do no specify any given realization. The value of the elementary charge expressed in coulomb, *i.e.* in ampere·second, simply means that the electrical current corresponds to a fixed flux value of elementary charges per time unit. Thus, any experiment based on the handling of elementary charges can, in principle, constitute a realization of the ampere. Besides, let us note that the definitions of all others electrical units have not changed in the revised SI. Following the verification of the quantum theories of the JE and the QHE with lower uncertainties, and to some extent of the single-electron tunneling effect, the relationships $K_J = \frac{2e}{h}$, $R_K = \frac{h}{e^2}$ and $Q = e$ are adopted in the revised SI. It results that the JE, the QHE and the SET effect are recommended experiments to realize the volt, the ohm, and the ampere. Fig. 1 (right) illustrates the link of these three units to h, e, and $\Delta\nu_{Cs}$. The constants being exact, the uncertainty of realization of units comes from the implementation of the quantum phenomena, and no more from the definition of the ampere itself. Recommendations for the *mise en pratique* of the electric units were written (draft [108] for Appendix 2 of the SI Brochure for the "Revised SI"). Here are reported those concerning the volt, the ohm, and the ampere.

Practical realization of the volt, V. The volt, V, can be realized from K_J using the Josephson effect. Although the $2e/h$ value can be used, a truncated value with 15 significant digits is recommended: $K_J = 483\,597.848416984$ GHz·V^{-1}. This value is lower than the value K_{J-90} by a relative amount of 106.665×10^{-9}. As a consequence, the numerical value of a voltage measured in terms of the new SI volt is larger than the value measured in terms of K_{J-90} by the same amount.

Practical realization of the ohm, Ω. a) The ohm, Ω, can be realized from R_K by using the quantum Hall effect in a manner consistent with the CCEM Guidelines [109]. Although the h/e^2 value can be used, a truncated value with 15 significant digits is recommended: $R_K = 25\,812.8074593045$ Ω. This value is larger than the value R_{K-90} by a relative amount of 17.793×10^{-9}. As a consequence, the numerical value of a resistance measured in terms of the new SI ohm is larger than the value measured in terms of R_{K-90} by the same amount; or b) by comparing an unknown resistance to the impedance of a known capacitance using, for example, a quadrature bridge, where, for example, the capacitance has been determined by means of a calculable capacitor and the value of the electric constant of vacuum $\epsilon_0 = 1/\mu_0 c^2$. In the revised SI, the magnetic constant of vacuum has no longer the exact value $4\pi \times 10^{-7}$ N/A^2. It is obtained from the fine structure constant value $\mu_0 = 2\alpha/ce^2$. The value determined from the CODATA 2017 adjustment is $\mu_0 = 4\pi[1 + 2.0(2.3) \times 10^{-10}] \times 10^{-7}$ N/A^2 = $12.5663706169(29) \times 10^{-7}$ N/A^2. It results that the value of ϵ_0 is no longer exact either. Its relative uncertainty is equal to that of μ_0, since c is fixed.

Practical realization of the ampere, A. a) The ampere can be realized by using Ohm's law, the unit relation A = V/Ω, and using practical realizations of the SI derived units the volt V and the ohm Ω, based on the Josephson and quantum Hall effects, respectively;
or
b) by using the relation $I = C\mathrm{d}U/\mathrm{d}t$, the unit relation A = F·V/s, and practical realizations of the SI derived units the volt V and the farad F and of the SI base unit second s;

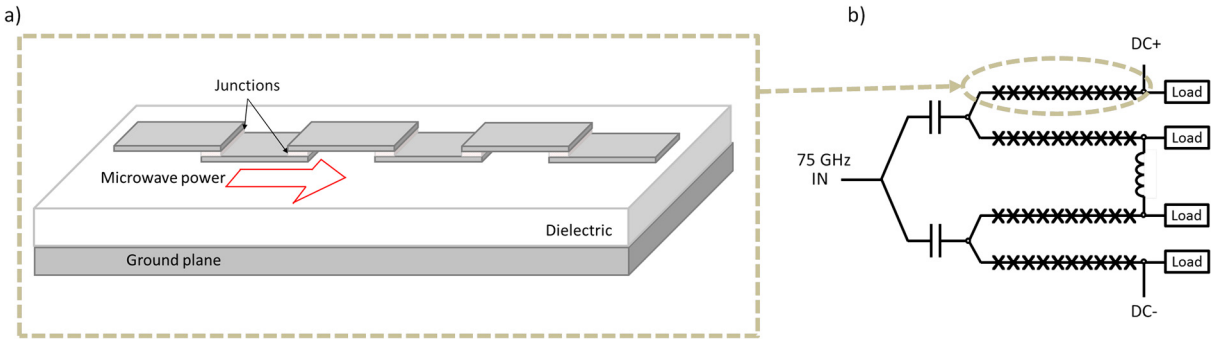

Fig. 10. Array of Josephson junctions. (a) Series of Josephson junctions introduced in a microstrip transmission line. The junctions are distributed in the microstrip over a superconducting ground plane, separated from the strip by a dielectric layer. (b) Schematic of the circuit of a typical Josephson voltage standard: to increase the number of JJ while limiting the effect of rf power attenuation in the transmission line, the JVS is formed of parallel series arrays terminated by matched loads that absorb the rf power and avoid reflections. A network of low- and high-pass filters splits the microwave power into parallel paths (here four), and allows all junctions to be connected in series at dc. Inspired from [113].

or
c) by using a single electron transport (SET) or similar device, the unit relation A = C/s, the value of e given in the definition of the ampere and a practical realization of the SI base unit second s. However, SET implementations still have technical limitations and often larger relative uncertainties than some other competitive techniques.

Mises en pratique based on quantum electrical standards were also recommended for the units coulomb, farad, and watt [108]. Generally, the revised SI promotes quantum solid-state physics. This is to sustain the further development of the quantum electrical standards and their applications.

2. The volt and the ohm from quantum standards

2.1. The quantum voltage standard

Introduction. Nowadays, in NMIs, coexist three generations of state-of-the-art Josephson voltage standards (JVS): the conventional and programmable Josephson voltage standards (CJVS and PJVS), and the Josephson arbitrary waveform synthesizers (JAWS or ACJVS). These JVS are very complex superconductive circuits with thousands of junctions in series. The development of JVS had to overcome several difficulties concerning the quality of the JJ (homogeneity of the junction parameters over large areas of the order of the cm^2, stability of the material, high yield), the optimization of the microwave design, and the design of the bias electronics. Not only, at each generation, the number of junctions and the complexity of the circuit have increased, but also the domain of applications.

The first generation was dedicated to dc voltage metrology. The main achievement of these standards is the increase of the voltage output from a few millivolts [47,110] to 10 V [111,112] and the establishment of the basis of the present standard volt conservation to a few parts in 10^{10}. The PJVS have opened the way to the rapid dc voltage selection and to low-frequency ac applications. Finally, JAWS are achieving the mutation towards programmability and higher frequencies by allowing the generation of arbitrary waveforms with fundamental accuracy up to the MHz range. Several review papers on JVS have been published covering all the aspects of the Josephson voltage standards [112,37,36,113–116]. Here we will present the state of the art of the three generations of JVS.

2.1.1. Conventional devices

Principle. The CJVS are based on the idea proposed by Levinsen in 1977 [117] to use the zero-crossing steps shown in Fig. 3c corresponding to $\beta \geq 100$. First, there are no stable regions between the first steps, this ensures the quantization of the voltage. Second, all the steps can be selected with the same bias current ($I \sim 0$), and the array can be disconnected from the bias source during the measurements. This relaxes, to some extent, the need of perfectly identical JJ parameters in the arrays, and for this reason it allowed the fabrication of the first 10-V arrays of JJ [111,112].

Junction. SIS (Superconducting/Insulator/Superconductor) junctions are fabricated with $Nb/Al_2O_3/Nb$ thin film structures [118], which ensure clean interfaces and thin insulating junction barrier. Niobium (Nb) is mechanically and chemically stable, preventing the Josephson arrays from aging problems. Moreover, the critical temperature of Nb of 9 K allows working in liquid helium at 4.2 K [115]. The junctions are planar junctions of width w and length l made by the superposition of two superconducting films separated by the insulating barrier. They are imbedded in the microstrip of a superconducting microstrip-transmission line, as illustrated in Fig. 10a. The choice of the Josephson junction parameters w, l, and I_c as well as that of the operating frequency f can be determined within the RSCJ model (Section 1.3 and Fig. 10) with the aim to increase the stability of phase-lock against thermal noise and chaos, and to avoid any spatial dependence of the junction

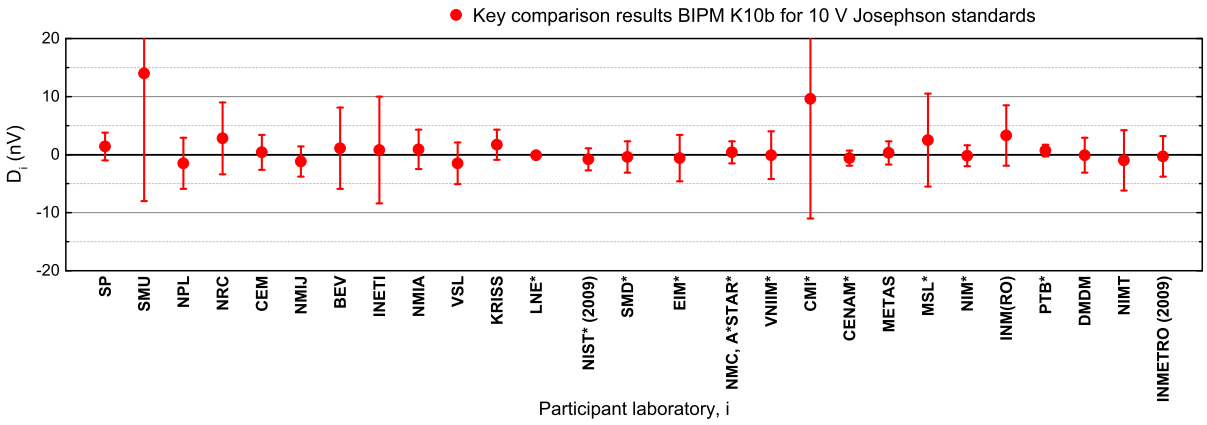

Fig. 11. Results [121] of the key comparison BIPM.EM-K10.b, SIM.EM.BIPM-K10.b and K10.b.1, COOMET.EM.BIPM-K10.b for 10-V Josephson standards, expressed in terms of degrees of equivalence. The degree of equivalence is given by a pair of terms, $[D_i, U_i]$, where D_i is the result of the measurement carried out by laboratory i expressed as the difference from the BIPM value, and U_i is the expanded uncertainty, $U_i = ku_i$, where $k = 2$ is the coverage factor and u_i the combined uncertainty.

phase over the junction area. For a detailed discussion on the subject, see refs. [37,36]. Typical parameters for the junctions are $w = 30$ µm, $l = 18$ µm corresponding to a critical current of 110 µA, and working frequencies are around 75 GHz [113].

Microwave circuit. Typical 10-V Josephson voltage standards are composed of about 14 000 to 20 000 Josephson junctions [119,120]. To reach 10 V, high-order constant voltage steps are exploited (typically, at 10 V, a JVS of 14 000 JJ works in average on the voltage step $n = 5$). A homogeneous rf power distribution for all the junctions is a key element for proper operation of the JVS; hence, the problems of rf power attenuation and reflections should be circumvented. The rf power attenuation along a series array limits the number of junctions in one array to about few thousands. To reach more than 10 000 JJ, several arrays are needed. This is realized by connecting series arrays in a series/parallel circuit as shown in Fig. 10b. This circuit allows splitting the microwave power into parallel paths while maintaining a dc path. The reflections are avoided by a matched load at the end of each series array.

Measurement system and applications. The measurement system is composed of the microwave source phase locked to a 10-MHz frequency referenced to an atomic clock through a GPS receiver, a bias electronics which allows selecting the zero-crossing steps, an oscilloscope to visualize the steps and to optimize the microwave power and frequency. Once the step is selected, the array is disconnected from the bias source. The CJVS are used for the calibration of the 1.018-V and 10-V outputs of Zener-diode-based dc reference standards used in the traceability chain and for the calibration of the gain and linearity of high-precision digital voltmeters. Fig. 11 presents the results of the international key comparison BIPM EM K10b [121]. It shows that, for most of the participants, the degree of equivalence, which is defined as the voltage difference with respect to the BIPM value associated with the expanded uncertainty U_i corresponding to a coverage factor $k = 2$, is below 5 parts in 10^{10} [122] and some are at a few parts in 10^{11} [123]. The wide dissemination of CJVS is ensured by the commercialization of these standards by two high-tech companies specialized in superconducting electronics [124,125].

2.1.2. PJVS at 10 V or more

Principle. Josephson voltage standards based on zero-crossing steps are not satisfying for programmable applications due to the difficulty to select a precise voltage step number n, and because of the susceptibility to noise-induced spontaneous transitions. To circumvent the problem, in 1995, Hamilton et al. [126] proposed to use overdamped junctions for which each bias current value corresponds to a single voltage value (Fig. 12a). He also suggested to transform the array into a "digital-to-analogue converter (DAC) of fundamental accuracy" by dividing a series array of N_J junctions into segments containing different numbers of JJ, as depicted in Fig. 12b. Each segment is current biased on one of the three constant voltage steps $n = -1, 0$, or $+1$, such that the output voltage can take any value between $\pm N_J \Phi_0 f$ by increment of the voltage of the smallest segment. Most of the 1-V arrays were subdivided in segments with a number of JJ following a binary sequence [127]. On the other hand, 10-V arrays, depending on the junction technology, can have very different sequences [128–130]. The programmability is possible thanks to a computer-controlled bias source. An ac voltage $V_{out}(t)$ can be generated by biasing sequentially different segments so that the output signal is a stepwise approximated waveform, as sketched in Fig. 12c.

Junctions and microwave circuit. The PJVS technology has evolved during about 15 years. For a historical overview of the development, the reader can consult recent reviews [115,116]. The current technology is based on SNS (superconducting–normal metal–superconducting) junctions, which are intrinsically overdamped junctions ($\beta \leq 1$). Kautz [38] showed that the

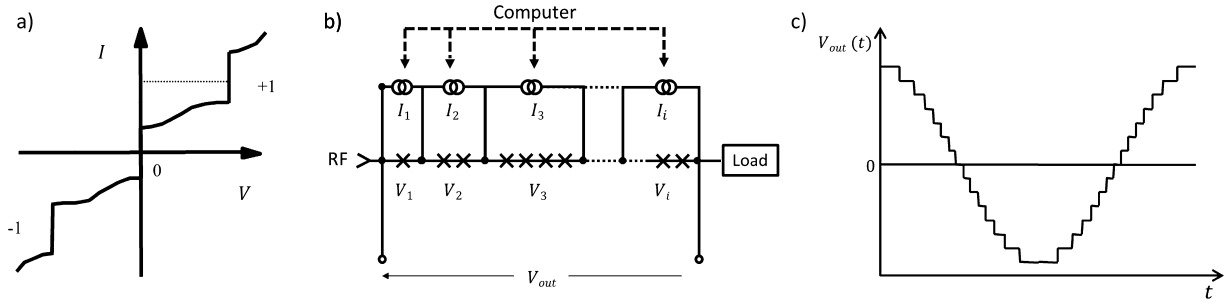

Fig. 12. Programmable Josephson voltage standards (PJVS) principle: a) I–V characteristic of a non-hysteretic Josephson junction ($\beta \leq 1$) under microwave irradiation, showing the three constant voltage steps $n = \pm 1, 0$ used in PJVS. b) Principle of the digital-to-analog converter based on a Josephson array [126]. Here the array is divided in i segments containing a number of JJ following a binary sequence. Each of the segments is biased by a computer-controlled current source. c) AC voltage generation: the output voltage $V_{\mathrm{out}}(t)$ of the PJVS is a stepwise approximated waveform.

Table 3
Main characteristics of the 10-V PJVS arrays developed by PTB, NIST, and NMIJ.

Characteristic	PTB [129]	NIST [132,130]	NMIJ [134,135]
Voltage	10 V	10 V	17 V
Frequency	70 GHz	18.3 GHz	16 GHz
Junctions	69 632	268 800	524 288
Material	$Nb/Nb_xSi_{1-x}/Nb$	$Nb/Nb_xSi_{1-x}/Nb$	$NbN/TiN_x/NbN$
Temperature	4.2 K	4.2 K	9.8 K
Stacks	1	3	2
Transmission line	Microstrip	Coplanar waveguide	Coplanar waveguide
Parallel arrays	128	32	64

high critical currents (in the mA range) of SNS junctions provide good immunity to thermal and electrical noise and that the frequency of operation should be very close to the characteristic frequency, $f_c = \frac{2e}{h} I_c R$, in order to obtain simultaneously the maximum amplitude for the voltage steps $n = \pm 1, 0$.

Among the three Institutes that fabricate 10-V PJVS, (NIST, PTB, and NMIJ/AIST), NIST and PTB are using $Nb/Nb_xSi_{1-x}/Nb$ junctions first developed at NIST [131]. Despite the same material, the arrays operate at very different frequencies, 18 GHz at NIST [132] and 70 GHz at PTB (Fig. 13a) [129]. The operating frequency is adjusted by tuning the I_cR_n product by changing both the thickness of the barrier and by varying the Nb content of the amorphous Nb_xSi_{1-x} by a few percent. The choice of NMIJ is to use $NbN/TiN_x/NbN$ junctions benefiting from the higher critical temperature of NbN at 16 K in order to fabricate PJVS able to operate at a temperature above 4.2 K in cryocoolers.

The use of Nb_xSi_{1-x} and TiN_x enables the vertical stacking of the JJ. Double and triple stacked JJ are currently used in the 10-V PJVS from NIST and NMIJ, to limit the size of the array while increasing the number of JJ to compensate for the reduction of the operating frequency. PTB could achieve 20 V [133] with a double stack. The two different domains of operating frequency lead to different microwave designs: at 70 GHz, the microstrip transmission line of the CJVS has been adapted, while in the 20 GHz range, coplanar waveguides (CPW) are used. Table 3 summarizes the parameters of the different 10-V PJVS.

Measurement set-up and applications. The accuracy of 10-V PJVS has been demonstrated by comparison to 10-V CJVS; no significant difference between the voltage standards were measured within 1.2 part in 10^{10} [136] and 2.6 parts in 10^{10} [137] ($k = 2$). The recent comparison of two cryocooled 10-V PJVS [138] illustrates the advantages of the PJVS over the CJVS. The complete automation and synchronization of both systems allow voltage reversals over very long measurement times (28 h) and enable the use of a very sensitive null detector. The authors have measured the voltage difference at 10 V between the two systems with a relative combined uncertainty of 2.9 parts in 10^{11} ($k = 2$). Today, PJVS tend to replace CJVS not only for the calibration of Zener dc references, but also for the calibration of the gain and linearity of high-precision digital voltmeters through automated measurements [139,140].

For low-frequency ac applications (< 1 kHz), the generation of stepwise approximated waveforms has been used to calibrate ac–dc thermal converters; however, the transients, *i.e.* the unquantized parts of the signal between two quantized voltage levels of the waveform, contribute to the uncertainty and are difficult to handle [141]. Despite this, uncertainties of the order of 1 part in 10^6 have been reported [142,143].

Today, the PJVS are mainly used with sampling techniques (for review [116,144]): the stepwise waveform is compared with an unknown ac signal using a fast analogue-to-digital converter (ADC) replacing the null detector used in dc voltage comparisons (differential sampling or ac quantum voltmeter [145,146,116,144]) as depicted in Fig. 13b or by alternately measuring both signals with the same ADC [147,148,144]. This comparison is done only when the voltage of the array

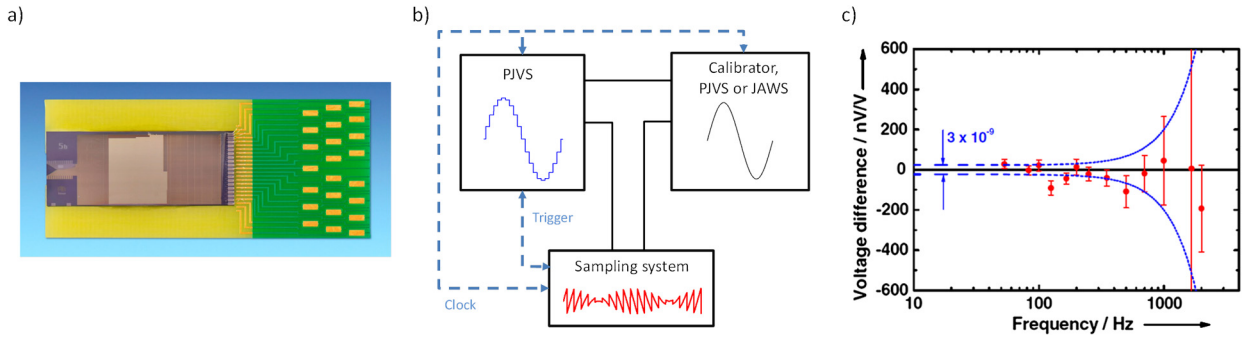

Fig. 13. (a) Photograph of a 10 V programmable Josephson voltage standard (PJVS) operating at 70 GHz (by courtesy of PTB). (b) Principle of the differential sampling technique with a PJVS. A stepwise sinusoidal waveform is compared with an unknown ac signal using a fast analogue-to-digital converter (ADC) replacing the null detector used in dc voltage comparisons. (c) Comparison of two 4-sample waveforms ($[0, +V_{max}, 0, -V_{max}]$) generated by two 10-V PJVS using a sampling voltmeter. From ref. [116].

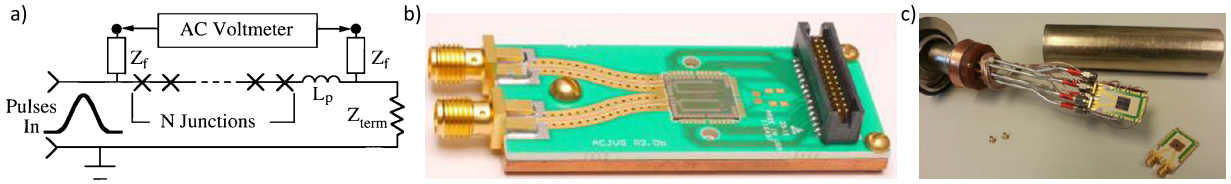

Fig. 14. (a) Principle of pulse-driven arrays: a series array of N Josephson junctions distributed along a wide bandwidth transmission line is biased by current pulses that generate quantized voltage pulses with a time-integrated area Φ_0 at each junction. A pulse train of frequency f generates an average voltage $N\Phi_0 f$ across the array, which is measured at the low-pass-filtered output of the array. An arbitrary waveform can be generated by gating the input pulse train with a long digital word generator. ©1998 IEEE. Reprinted, with permission, from ref. [157]. (b) Photograph of the NISTS's new 1-V JAWS package. ©2016 IEEE. Reprinted, with permission, from ref. [158]. (c) Photograph of the PTB's 8-channel cryoprobe. From ref. [159].

is on a quantized plateau of the stepwise approximated waveform. However, as the frequency is increased, the length of each plateau is reduced (for a given number of samples) and this limits the accuracy above a few kHz. Fig. 13c shows the comparison of two 4-sample waveforms generated by two 10-V PJVS showing an agreement of the voltage standards, below 400 Hz, within the type-A uncertainty of 3 part in 10^9 [116]. Comparing two waveforms by differential sampling rather than by sampling them successively by the same sampler reduces the errors due to the gain and the non-linearity of the ADC at the expense of the necessity to lock the PJVS, the ac source and the ADC to a common frequency reference. Indeed, any phase jitter from the ac-source or the ADC is detrimental in terms of uncertainties. The performance of the differential sampling systems (at 7 or 10 VRMS) have been studied in different laboratories [146,149,146,150,151,140]. Today, liquid cryogen-free PJVS systems have been demonstrated [152–154], and fully automated systems are available from NIST and Supracon. A very interesting application of PJVS was suggested for impedance ratio measurements based on two PJVS systems generating square waves: the Josephson two-terminal-pair impedance bridge [155]. The recent variants of impedance bridges (see section 4.2) are set up with pulse-driven arrays, which generate pure sinusoidal waveforms (see section 2.1.3).

2.1.3. JAWS: pulse driven arrays

Principle. To resolve the problem of transients in the generation of ac signals based on PJVS, Benz et al. proposed in 1996 [156] to bias the array by a train of short current pulses generated by a pulse generator as depicted in Fig. 14a. For a given pulse area, each JJ generates a quantized voltage pulse. The array then acts as a pulse quantizer transferring a single flux quantum Φ_0 for each input pulse (see section 1.3). The voltage across the array is determined by the repetition rate f (Fig. 14a), which can be modulated to generate arbitrary waveforms. As the pulses can be generated at a very high speed ($\sim$ 15 GHz) compared to the frequency of the desired signal (in the MHz range), generating arbitrary waveforms can be dealt with oversampling techniques. In particular, noise shaping techniques using delta-sigma modulation algorithms [160] can be applied to push most of the quantization noise to high frequencies. By this way, pulse sequences corresponding to pure sine wave can be determined with extremely low distortion [158]. Most of the difficulties lie in the way to generate the bipolar pulses at a rate of $\sim 15 \times 10^9$ pulses per second and to ensure that the pulses propagate with low distortion in the transmission line, such that each bias pulse generates one quantized voltage output pulse for all the junctions. For more details on JAWS, the reader can consult recent reviews [116,144].

The denomination of the pulse-driven technique depends on the domain of application (ACJVS for pure sinewaves generation or QVNS for quantum voltage noise source for a pseudo-random noise source used in electrical based thermometry, see section 4.3). Today, due to the high complexity of these systems, only NIST and PTB are developing JAWS systems; however, they have established close collaborations with several groups [161–164].

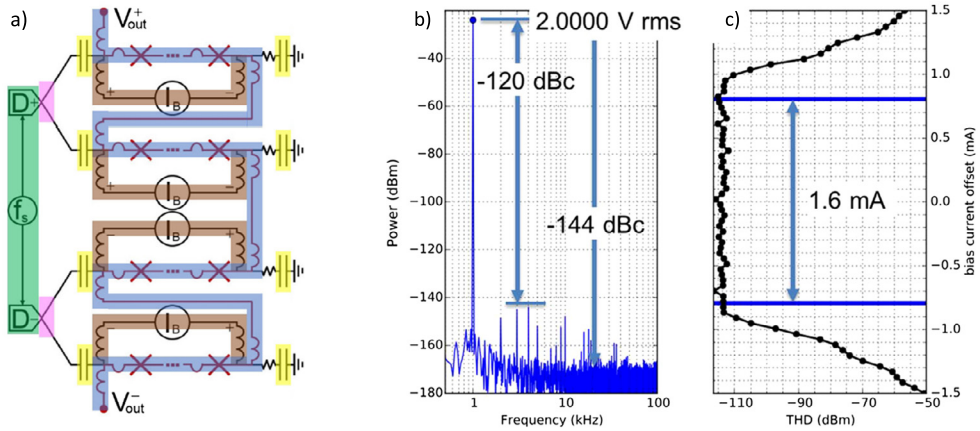

Fig. 15. (a) Schematic of the 1-V JAWS chip from NIST showing the series parallel connection of four JJ arrays fed with only two pulse generator channels (green), thanks to on-chip power splitters (Wilkinson dividers) (pink) [166]. Arrays are capacitively coupled with the pulse generator channels via inside–outside dc blocks (yellow). This filters the low-frequency components of the pulse train and avoids common-mode voltage on the load. In order to restore the complete pulse spectrum in the array and therefore improve the operating margins, floating low-frequency current sources (in brown) bias each array via inductive taps. The total quantized low-frequency voltage is obtained by connecting the arrays in series via inductive taps. From ref. [144]. (b) Digitally sampled spectral measurement showing a low-distortion JAWS output voltage with an rms magnitude of 2 V. ©2016 IEEE. Reprinted, with permission, from ref. [158]. (c) Total harmonic distortion (THD) versus dither offset current showing the 1.6 mA operating current range. ©2016 IEEE. Reprinted, with permission, from ref. [158].

Junctions, microwave circuit, bias techniques and applications. The junctions used for JAWS are SNS junctions based on the same technology used for PJVS ($Nb/Nb_xSi_{1-x}/Nb$) optimized around 20 GHz [131,165]. Double or triple stacked [166,159] junctions are used. The maximum output is lower than for PJVS, but recently several breakthroughs have been reported [159,167,168,158,166]. The main difficulty lies in the broadband nature of the pulses, which have significant power at frequencies up to 30 GHz [166], and which are very sensitive to non-linearities in the coplanar waveguide. Many techniques have been adapted from the PJVS arrays to improve the propagation of the pulses in the transmission lines [166,169]. In addition, pulse generation methods have been optimized over more than 15 years [170–172].

Recently, the two groups of NIST and PTB have demonstrated rms amplitudes up to 3 V. Kieler et al. could reach an rms voltage of 1 V by summing the voltages of eight arrays (on four separate chips) for a total of 63 000 JJs [159,167]. Each array is connected to a separate channel of an eight-channel ternary pulse pattern generator in order to minimize the pulse distortion. Fig. 14c shows the cryoprobe with the four chips. A direct comparison with a PJVS has demonstrated an agreement better than 1 part in 10^8 ($k = 1$) at 250 Hz [167]. Flower-Jacobs et al. [158] have demonstrated rms amplitudes of 2 V (Fig. 15a and Fig. 15b) [158] and recently even 3 V [173] in a cryocooler, by connecting two chips of four arrays (Fig. 15a) and two chips of eight arrays, respectively, for a total of 102 480 JJs and 204 960 JJs, respectively.

JAWS systems are mainly used for the calibration of thermal transfer standards with high input impedance in order to avoid loading the array output. However, direct calibration of thermal converters with lower impedance might be improved by using buffer [174] or transconductance amplifiers [175,176] similar to the ones developed for implementation with a PJVS [142,143]. Another challenge is to limit the major systematic error due to the voltage leads when measuring at frequencies up to 1 MHz [162,177]. JAWS systems allow one to test the non-linear behavior of electronic components by generating multi-tone waveforms [178,179]. Other applications concern Johnson noise thermometry (see section 4.3) and impedance bridges (see section 4.2).

2.2. The quantum Hall resistance standard

2.2.1. Usual QHR

Quantum Hall resistance standards [74,99,180] are usually based on Hall bars made of GaAs/AlGaAs heterostructures, the electronic properties of which are well adapted to the metrological application. The two-dimensional electron gas forms at the interface between two semiconductors having different electron doping and energy gaps (Fig. 16a). These heterostructures can be fabricated by molecular beam epitaxy (MBE) or metal organic chemical vapor deposition (MOCVD). For application to resistance metrology, carrier densities and electron mobilities in the ranges from 3×10^{15} to 5×10^{15} cm^2 and from 10 to 80 T^{-1}, respectively, are optimal. Samples are fabricated using usual lithography and etching techniques with a wide Hall bar geometry (typically 400 µm) characterized by two current contacts and usually three pairs of voltage terminals (Fig. 16b). The Hall bar design aims at optimizing contact surface, breakdown currents and edge state equilibrium. Contacts with the 2DEG are realized by annealing an AuGeNi deposit (diffusion of germanium).

The $\nu = 2$ Hall resistance plateau of usual QHRS is quantized to within one part in 10^9 at a magnetic induction of about 10 T, a temperature below 2 K and a measurement current below 100 µA (the breakdown current reaches a few hundreds of µA for best devices). As a result of many studies performed by metrologists, technical guidelines [109] concerning samples

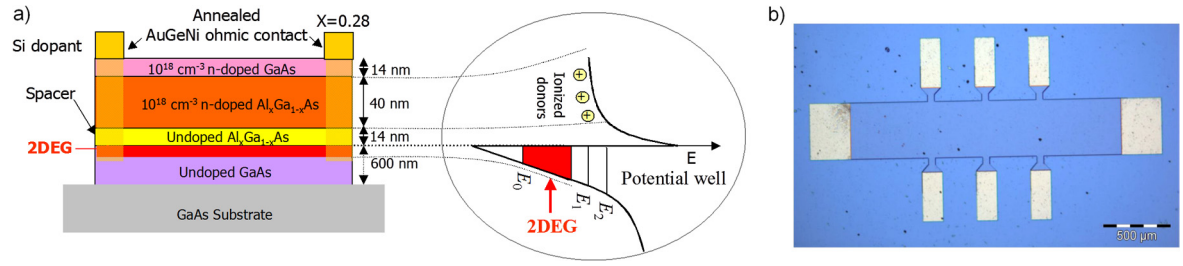

Fig. 16. (a) Typical GaAs/AlGaAs heterostructure used to form a two-dimensional electron gas (2DEG): layer stacking (left), energy bands, 2D subbands, and potential well (right). Reprinted by permission of Springer Nature from ref. [99], ©2009. (b) Optical picture of a typical device based on a 2DEG having a Hall bar geometry and eight terminals. Electrical contacts are made from annealed AuGeNi deposits (C2N/LNE).

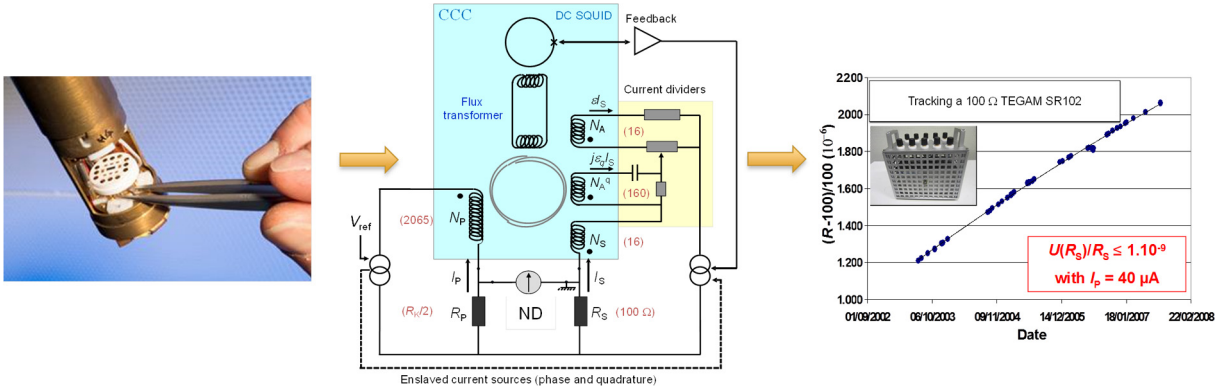

Fig. 17. Calibration of a resistor from the QHE: the resistance of a resistor (right) is compared to the quantized Hall resistance of a GaAs/AlGas device (left) using a CCC-based resistance bridge (center).

properties and characterizations have been recommended to check the quality of a QHR. The verification of some technical criteria ensures that the Hall resistance is accurately quantized: contact resistances below 10 Ω, longitudinal resistances below 100 µΩ, spatial homogeneity, insensitivity to the direction of the magnetic field...

The most accurate way to calibrate a resistance from $R_K/2$, described in Fig. 17, relies on a resistance bridge [74,99] based on a cryogenic current comparator (CCC) [181]. Briefly, the method consists in measuring the ratio of the two currents circulating through the resistors and generating at their terminals the same drop voltage. The current ratio is determined using the CCC, which is a perfect transformer operating in direct current. More precisely, this device can measure the ratio of two currents in terms of the ratio of the numbers of turns of the two windings through which circulate the two currents with a relative uncertainty below 10^{-10}. Its accuracy relies on a flux density conservation property of the superconductive toroidal shield (Meissner effect), in which superconducting windings are embedded. Owing to a flux detector based on a dc superconducting quantum interference device (SQUID), the current noise resolution of the CCC can be as low as 80 pA·turn/Hz$^{1/2}$ [182]. Recent resistance bridges [183–186,77] can calibrate a 100-Ω resistor from $R_K/2$ with a relative uncertainty of a few 10^{-10}. They are more sensitive, accurate, versatile, and automated than the first generation developed in the 1980s. In the revised SI, the reference value that must be used in resistance calibration certificate is $R_K = h/e^2$. It differs from the value R_{K-90}, so the numerical value of a resistance measured in terms of the new SI ohm is larger than the value measured in terms of R_{K-90} by a relative amount of 1.7793×10^{-8}.

2.2.2. Arrays

The perfect equipotentiality along edges and the quantization of any two-terminal resistance at R_H value are two fundamental properties of the QHE that can be exploited together to get rid of the resistance of the connections between multiply-connected Hall bars. More precisely, let us consider a Hall bar with a resistance r_1 connected in series with a current terminal. The two-terminal resistance, R_{2T}, equal to $R_H + r_1$, becomes $R_H + r_1 r_2/R_H$ if adding a connection to a second terminal at the same potential as that of the first terminal. The relative effect of series resistances, r, is reduced according to $(r/R_H)^n$, where n is the number of connections. The so-called multiple connection technique [187] can be used to realize arrays of QHRs extending the range of quantized resistance values. It was successfully used to realize array resistance standards having values [188–191] in the range from 100 Ω to 1.29 MΩ, quantized in terms of R_K to within a few parts in 10^9 (18a). Devices were based on several tenths of GaAs/AlGaAs Hall bars combined in series and/or in parallel using a triple or quadruple connection technique. The achievement of quantized arrays relies on GaAs/AlGaAs heterostructures having very homogeneous electronic density (to within a few percents), so that all Hall bars are quantized at same magnetic induction. Multiple interconnections require good ohmic contacts and perfect insulating layers (*i.e.* without pinholes) to electrically

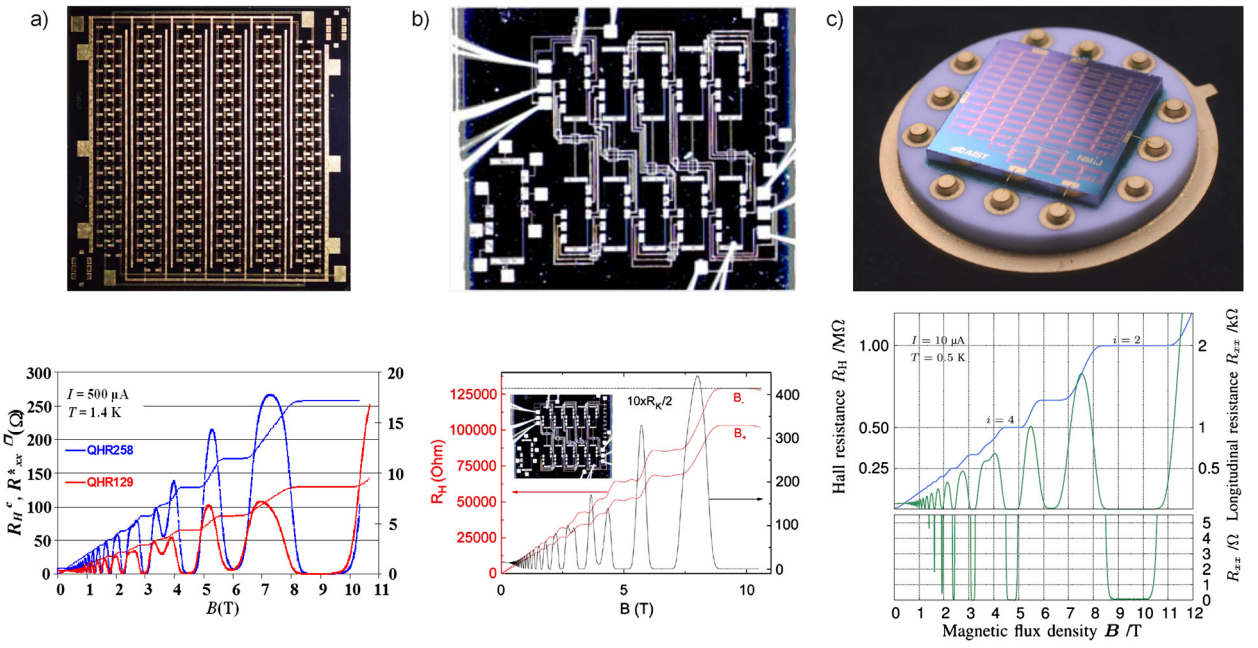

Fig. 18. (a) Top: picture of an array developed by LNE in collaboration with the "Laboratoire d'électronique de Philips": it is based on 100 Hall bars connected in parallel [189]. Bottom: magneto-resistance measurements carried out for arrays of $R_K/200$ (QHR129) and $R_K/100$ (QHR258) nominal values on the $\nu = 2$ plateau. (b) Top: picture of an array developed by PTB made of 10 Hall bars connected in series. Bottom: magneto-resistance measurements carried out for two magnetic field directions. ©2011 IEEE. Reprinted, with permission, from ref. [192]. (c) Top: picture of an array developed by NMIJ of nominal value close to 1 MΩ made of 88 Hall bars. Bottom: magneto-resistance measurements. ©2016 IEEE. Reprinted, with permission, from ref. [193].

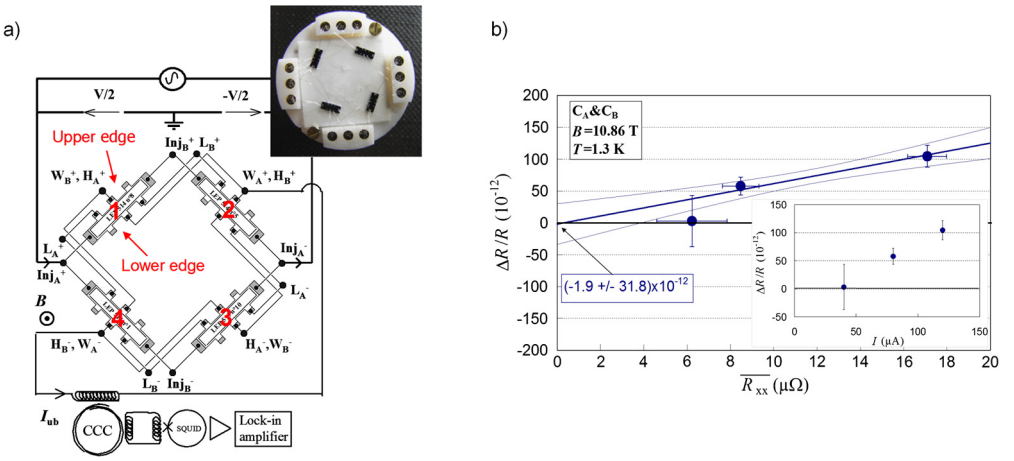

Fig. 19. (a) Scheme of the Wheatstone bridge based on the triple connection of four GaAs/AlGaAs (LEP514) Hall bars mounted on a single sample holder (picture). The unbalance current I_{ub} is measured using a CCC winding. (b) Extrapolation at zero dissipation ($\bar{R}_{xx} = 0$) of the relative deviation, $\Delta R/R$, of the quantized resistance of one standard from the others. One finds $\Delta R/R(\bar{R}_{xx} = 0) = (-1.9 \pm 31.8) \times 10^{-12}$. Reprinted from ref. [197], with the permission of AIP Publishing.

isolate different levels of connections. After these founding results by LNE, other NMIs undertook research to develop Hall bar arrays. PTB realized standards (Fig. 18b) made of ten Hall bars connected in series or in parallel [192,194]. NMIJ pursues the development of arrays to achieve not only resistance standards of 10 kΩ [195] and 1 MΩ [193] values (Fig. 18c), but also voltage dividers [196].

One particular array that can be implemented is the Wheatstone bridge, which is made of four Hall bars. Such a bridge was used to perform reproducibility tests of the QHE [71]. Fig. 19a shows a Wheatstone bridge mounted from four GaAs/AlGaAs Hall bars using a triple connection. The unbalance current of the bridge I_{ub} is related to the relative deviation of the quantized resistance $\Delta R/R$ of one standard from the others according to $\Delta R/R = 4I_{ub}/I$, where I is the biasing current of the bridge. Measuring I_{ub} using a sensitive CCC winding allowed the demonstration of the reproducibility of the quantized Hall resistance [197] with a record relative uncertainty of 3×10^{-11}, as shown in Fig. 19b.

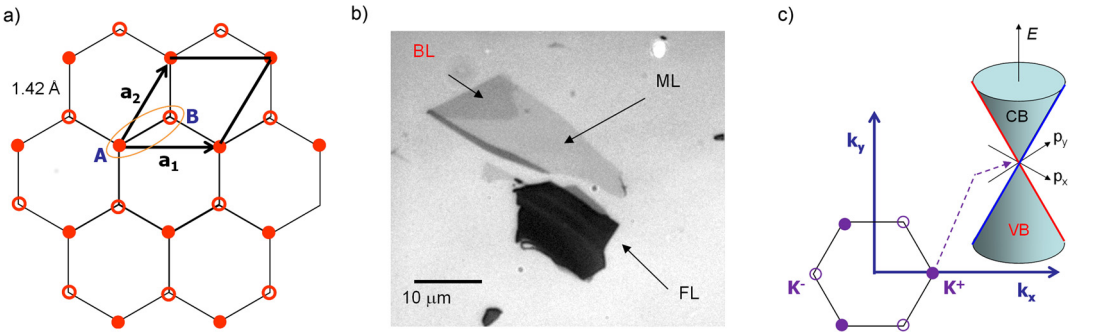

Fig. 20. (a) Honeycomb lattice of graphene with two atoms A and B per cell (a_1 and a_2 are base vectors). (b) Optical pictures of graphene flakes on top of a SiO_2/Si substrate: ML (monolayer), BL (bilayer), (FL) a few layers. (c) First Brillouin zone with two independent vertices: K^+ and K^- Dirac points. Conical energy spectrum around Dirac points.

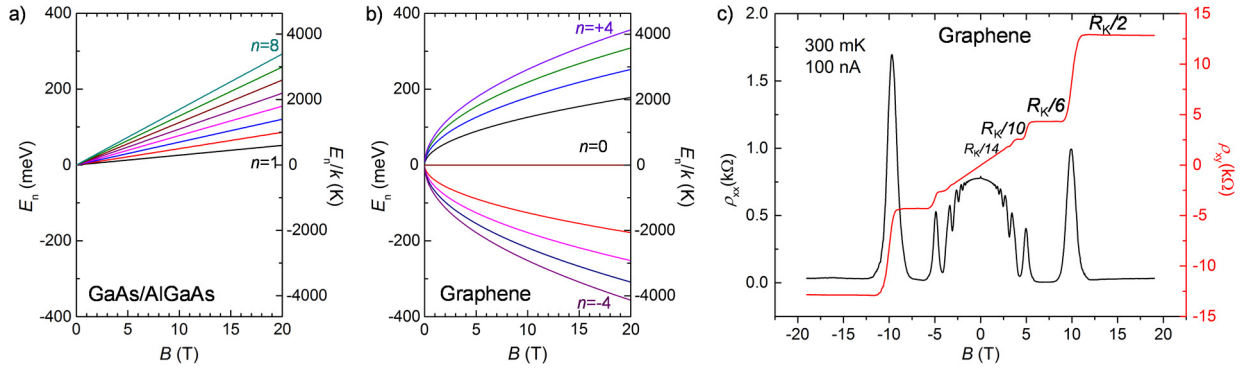

Fig. 21. Energy as a function of the magnetic induction B of Landau levels with index n in a) GaAs/AlGaAs ($n = 1{:}8$) and in b) graphene ($n = 0, \pm1, \pm2, \pm3, \pm4$). c) Hall resistivity ρ_{xy} and longitudinal resistivity ρ_{xx} as a function of B, measured in graphene grown on SiC by thermal decomposition with an electronic density of 1×10^{12} cm^{-2} and a mobility of 9000 cm^2·V^{-1}·s^{-1} [207].

2.2.3. *Graphene: towards a user-friendly standard*

Dirac physics. Graphene is a monolayer of carbon atoms crystallized (Fig. 20a) in a 2D honeycomb lattice. Fig. 20b shows optical pictures of graphene flakes of different numbers of layers. Its quantum electronic transport properties have been discovered [198] by Geim and Novoselov in 2004. Since then, based on the exceptional properties of graphene, not only electrical, but also mechanical, optical, thermal and chemical, many works have been carried out for fundamental research [199] and for industry applications [200] as well. Graphene is a gapless semiconductor with two valleys corresponding to the two independent vertices, called Dirac points, of the hexagonal Brillouin zone (Fig. 20c). At low energy around Dirac points, the energy spectrum [201] is conical and charge carriers behave as relativistic particles moving at Fermi velocity (Fig. 20c). Dirac physics [202,203] manifests itself and determines many properties including electronic transport: Berry's phase π, chirality (helicity is a good quantum number and is preserved in elastic scattering process), cancellation of backscattering at normal incidence, anti-localization. In addition, the absence of gap between the conduction and valence bands makes this material ambipolar: charge carriers can be either electrons or holes. One other emblematic property is a specific half-integer quantum Hall effect that was highlighted [204,205] right after the discovery of graphene. The energy spectrum [202,206] is quantized in Landau levels at energies given by:

$$\epsilon_n = \pm\sqrt{2e\hbar v_F^2 Bn} \tag{7}$$

where n is an integer value. The QHE in graphene differs from that in usual semiconductors by several peculiarities (Fig. 21a and Fig. 21b). The degeneracy of each Landau level is $4eB/h$ (spin and valley). The Landau level energy scales with $\sqrt{B}$ and the energy gaps depend on n. Moreover, a Landau level exists at zero energy and Hall plateaus occur at unusual filling factors $\nu = \pm(2n+1)$, *i.e.* at resistance values $R_H = \pm\frac{h}{e^2}\frac{1}{2(2n+1)}$, as can be observed in Fig. 21c. Lift of spin and valley degeneracy leads to the observation [208] of plateaus at other filling factors values such as $\nu = 0, \pm1, \pm4$. The Coulomb interaction is responsible for the manifestation of the fractional QHE [209,210] and also of ferromagnetic states [211,206, 212] that lift the $n = 0$ Landau level degeneracy [208,213,214].

Advantage for metrology. One specific property of the integer QHE, of strong interest for metrology, is that the energy gap ΔE in between the two first Landau levels is much larger in graphene than in GaAs/AlGaAs heterostructures for accessible

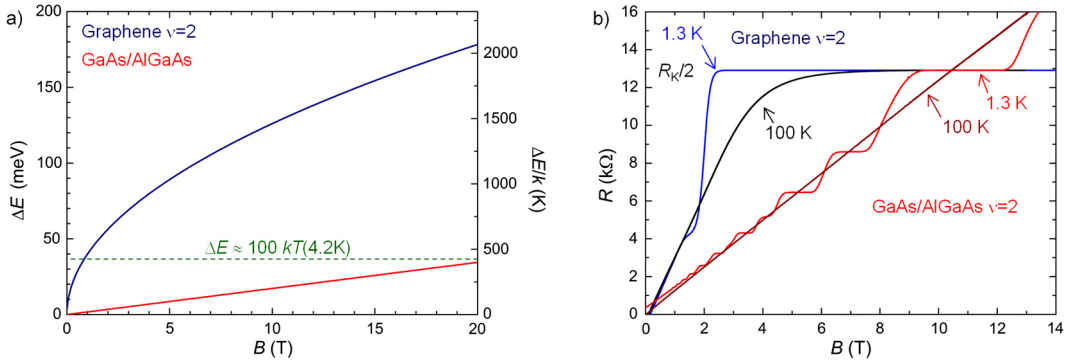

Fig. 22. (a) Energy gap between the two first Landau levels protecting the Hall plateau at $\nu = 2$ in graphene and between two nearest Landau levels in GaAs/AlGaAs (whatever their indexes) as a function of B. The energy level corresponding to 420 K is represented: it fixes the empirical minimum gap ensuring accurate Hall resistance quantization to within 10^{-9} at 4.2 K. (b) Hall resistance as a function of B, at two temperatures 1.3 K and 100 K, in a graphene device obtained by hydrogen/propane CVD on SiC [77] and in a typical GaAs/AlGaAs device used in metrology.

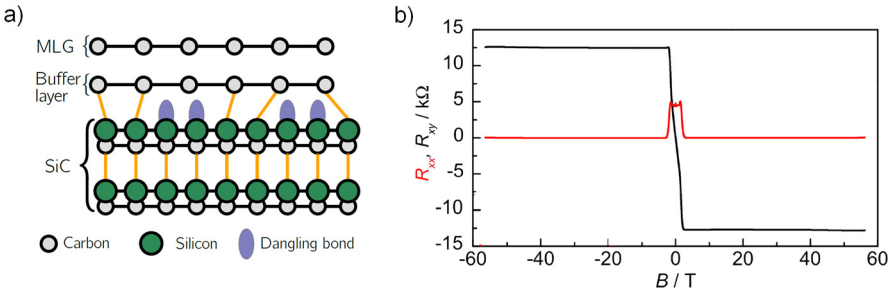

Fig. 23. (a) Structural model of a monolayer graphene (MLG) on SiC after growth on the Si-terminated face. The graphene is growing on top of the $(6\sqrt{3} \times 6\sqrt{3})R30°$ reconstructed interface layer, also called buffer layer. Only one atom over three of this layer is bonded to the substrate. From ref. [224], with permission of Fabien Lafont. (b) Measurements of the longitudinal resistance (R_{xx}, red) and of the Hall resistance (R_{xy}, black) in the in epitaxial graphene on SiC performed in pulsed magnetic field at $T = 2$ K. An exceptionally wide Hall plateau quantized at $R_K/2$ value is observed. From ref. [226].

magnetic fields, as shown in Fig. 21a. This explains the QHE robustness in graphene that has allowed the observation of the Hall resistance quantization at $\nu = 2$, even at room temperature [215]. Fig. 22b, which shows a $\nu = 2$ Hall resistance plateau measured in a graphene-based Hall bar that remains much wider at $T = 100$ K than the one usually measured in a GaAs/AlGaAs device at $T = 1.3$ K, also highlights this robustness. More precisely, the empirical criterion, $\Delta E > 100$ kT, which is roughly valid for GaAs/AlGaAs material in conditioning the Hall resistance quantization, would indicate that an accuracy of 10^{-9} could be achieved in graphene at 4.2 K from only 0.8 T. These energy considerations have motivated [99,216] the development of a graphene-based quantum resistance standard able to operate in more easy and accessible experimental conditions than its GaAs/AlGaAs counterpart.

Development of the graphene-based quantum Hall resistance standard: state of the art. Considering the great promise of graphene for developing a user-friendly quantum Hall resistance standard, research works started shortly after the first observations [204,205] of the QHE in graphene. The first precise measurements [217,218] of the quantized Hall resistance were carried out in 2008 by VSL, the Dutch metrology institute with samples from Geim and Novoselov's group, made of graphene obtained by exfoliation of graphite using the original "scotch tape" technique and then deposited on SiO_2/Si substrates [219]. The accuracy was limited to 1.5×10^{-5}, mainly because of the high resistance of the metallic contacts. Further works [220, 221] in exfoliated graphene have shown that the small typical size of these devices and the extreme sensitivity of graphene electronic properties to the close environment may impede the measurement of the Hall resistance quantization with accuracy in graphene. Using graphene on SiC produced in Linköping University, in Sweden, by thermal decomposition of the substrate, NPL performed, in 2010, the first demonstration that the Hall resistance can be quantized in graphene with the same accuracy as in GaAs/AlGaAs [222]. The agreement between Hall resistance measurement performed in both materials to within 8.7×10^{-11} is worth as one of the most precise QHE universality test [76,223]. Nevertheless, the experimental conditions of magnetic induction and temperature required for the graphene device were not competitive with those of typical GaAs/AlGaAs devices. The carrier density was too high to get the quantization of the $\nu = 2$ Hall resistance plateau, which is expected to be the most robust, at lower magnetic induction. This high doping results from a charge transfer caused by the coupling of the graphene layer with the SiC substrate *via* an interface layer, so-called buffer layer (Fig. 23a).

This interface layer, which only exists in case of graphene grown on the Si-terminated face of the SiC substrate [225], is electrically inactive, but can host a large density of localized donors. It acts as a charge carrier reservoir located very close to the graphene at a distance of about 0.3–0.4 nm. The charge transfer depends on the magnetic field: it exists

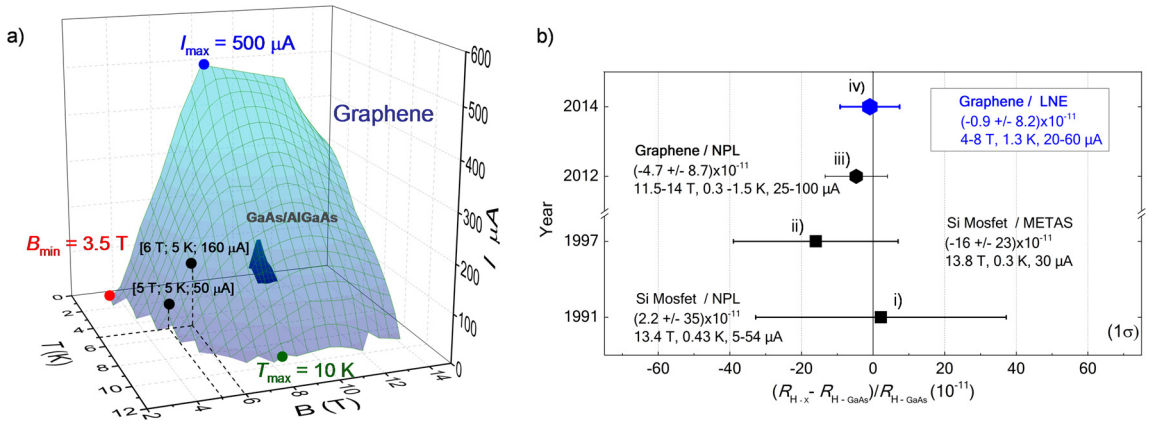

Fig. 24. (a) Experimental conditions of magnetic induction B, temperature T, and current I, under which a graphene device obtained by hydrogen/propane CVD on SiC exhibits quantization of the Hall resistance with an accuracy of 1×10^{-9} and better [77]. Two relaxed working points are pointed out. These conditions are compared with those typical (inner volume) that rules for a GaAs/AlGaAs device used as quantum Hall resistance standard. (b) Results of the most precise QHE universality tests, based on comparisons of the quantized Hall resistance in different materials with that realized in GaAs/AlGaAs: i) A. Hartland et al. [72], ii) B. Jeckelmann et al. [78], iii) T. J. B. M. Janssen et al. [223], and including the most recent and precise one realized with graphene, iv) Ribeiro-Palau et al. [77]. Experimental conditions of the Si-MOSFET and graphene devices compared to GaAs/AlGaAs devices are also indicated.

magnetic field intervals where the carrier density in graphene increases linearly with the magnetic field, which results in the pinning of the Landau level filling factor [227], particularly at $\nu = 2$. This pinning explains the broad magnetic field extension of the Hall resistance plateau observed in graphene on SiC (Fig. 23b). Besides, with the objective to increase the size of QHE graphene devices, LNE developed collaborations with CNRS–Institut Néel to exploit graphene grown by chemical vapor deposition on copper, which has also the advantage to be a scalable production technique that can be transferred to industry. In this work, it was demonstrated that, in case of polycrystalline samples, the Hall resistance quantization is not accurate in accessible conditions, because of grain boundaries short-circuiting the quantum Hall edge states [228]. Generally speaking, the different attempts show how much the material quality is crucial to achieve the goal of a graphene-based quantum Hall resistance standard operating in more accessible conditions.

One breakthrough [229,182] came from the use of samples made of graphene produced at CNRS–CRHEA by a hybrid technique [230] of hydrogen/propane CVD on SiC and processed at CNRS–C2N. In one (Fig. 22b) of these samples of moderate carrier density, 1.8×10^{11} cm^{-2}, and a relatively high mobility, 9400 cm^2·V^{-1}·s^{-1}, the quantization of the Hall resistance at $\nu = 2$ was demonstrated by LNE with state-of-the-art accuracy below 1×10^{-9}, at magnetic induction from 14 T down to 3.5 T, temperatures up to 10 K, or currents up to 0.5 mA [77]. This extended and relaxed range of experimental conditions, enabled by graphene, largely surpasses the conditions required by GaAs/AlGaAs devices, as shown in Fig. 24a. In addition, the studied graphene device demonstrates all the properties of a reliable primary quantum Hall resistance standard. Finally, the accuracy of the graphene device has been tested by comparison with a GaAs/AlGaAs device down to the record relative uncertainty of 8.2×10^{-11}. This led to the most precise QHE universality test [77] as highlighted in Fig. 24. After this demonstration, the efforts are now focused on improving the technology reliability: reproducibility, stability, control. One of the main issues is the control of the carrier density down to a low value, *i.e.* 5×10^{10} cm^{-2}, which is required to get operation of the graphene-based QHRS at very low magnetic induction, *i.e.* around 1 T, while keeping an excellent spatial homogeneity. This is a very big challenge, taking into account the gapless character of graphene and its sensitivity to the environment. Another issue concerns the identification of the key control parameter for robust and accurate Hall resistance quantization. In graphene grown on SiC, the buffer layer certainly plays an important role for these two issues [231]. Several current works address these points. On the one hand, PTB and NIST work to optimize the growth process to get high-quality reconstruction of the SiC surface [232,233]. On the other hand, RISE is developing a chemical gating technique to achieve low, homogeneous, and stable charge carrier density [234]. Considering the results demonstrated so far in graphene grown on SiC, researches are presently mainly focused on this material, but other routes still deserve to be explored. For example, graphene embedded in hexagonal boron nitride (h-BN) offers a better control of the environment, higher mobility, easier control of doping by electrostatic gating. Nevertheless, samples have smaller sizes and remain difficult to fabricate up to now.

To end, several extensions of graphene use in QHE metrology are also considered, where the material can provide the advantages of the low magnetic induction and high temperature operation, and even further ones. The first one is the development of a quantum Hall resistance standard operating in ac for impedance measurement traceability [235]. The second one is the realization of series arrays with more compact and less risky design, exploiting PN junctions, *i.e.* the ambipolarity of the material [236].

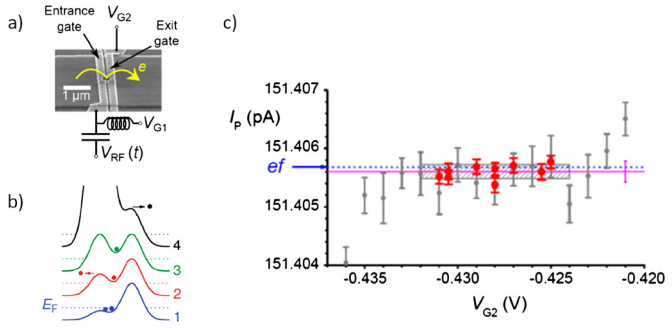

Fig. 25. (a) SEM picture of a current pump based on a quasi-1D GaAs wire with two gates at potentials V_{G1} and V_{G2}. (b) Electron transfer: four steps of modulation of V_{G1} potential at fixed V_{G2}. (c) Quantized current step obtained by varying V_{G2}. Adapted by permission of Springer Nature from ref. [254], ©2012.

3. The ampere realization from the elementary charge

3.1. Using new monoelectronic devices

Metallic electron pumps with fixed insulating barrier described previously are in the strong Coulomb blockade regime, where the tunnel barriers are highly resistive to ensure localized states, and where the tunneling is treated as a perturbation [91,86]. This regime is favorable to the precise transport of individual electrons. However, high tunnel barriers prevent the rapid loading of the electrons onto the metallic island, and thus, limit the operating frequency to preserve a low error rate due to missing electrons during the pumping cycle. As the corresponding output currents were too low (pA range) to realize a practical quantum current standard, several different systems have been investigated.

Among them is the hybrid superconducting normal metal turnstile [237] which shares the geometry of a single-electron transistor (SET), but follows the working principle of a normal turnstile [238]. It is made of a mesoscopic conducting island connected through tunnel junctions to two bulk electrodes, but for which the source and drain electrodes are superconducting (S). A gate voltage source is coupled capacitively with the central island of this SINIS structure and a small bias voltage is applied over the SET in order to define a preferred direction for single-electron tunneling. Under these conditions, for a normal SET, a gate span between different charge states always crosses regions where the current freely flows without control. However, in the hybrid SET, thanks to the presence of the superconducting gap $\triangle$ in the leads, and for bias voltages below $2\triangle/e$, these regions are suppressed. Then, an accurate quantized current can be generated by driving the SET between two adjacent charge states using a single ac gate voltage. An electron is transferred at each cycle of the driving frequency. This technique allowed the parallelization of ten turnstiles with an increased current up to 100 pA [239]. However, the limitation of the current level to 10 pA for a single aluminum-based SINIS turnstile [91], in order to reduce the errors due to high-order processes, limits drastically the metrological applications.

Most of the recent research has been concentrated on single-electron sources based on semiconductor quantum dots [240–247,254,248,249] (for a review, see [91,92]). These devices allow similar manipulation of individual electrons, but provide also the possibility to tune the barriers defining the dot by applying gate voltages. The pioneering work of Kouwenhoven et al. in 1991 demonstrated the transport of electrons through a quantum dot in GaAs/AlGaAs heterostructures by varying alternatively the height of the two barriers at a frequency f [84]. Very recent works [250–253] have improved the uncertainty in highly-controlled GaAs/AlGaAs and silicon quantum dots. Fig. 25a shows a SEM picture of a state-of-the-art single-electron device based on a quasi-1D GaAs wire, which was studied by Giblin et al. [254]. Fig. 25b illustrates the pumping scheme: it shows the evolution of the electrostatic potential and the electron transfer during the pumping cycle. The left barrier alone is modulated, the right barrier is set well above the Fermi energy to prevent electrons from escaping. To increase the working frequency, during the loading phase the left barrier is completely opened such that few electrons can be loaded on the dot. Then the left barrier is raised to isolate the dot, while some electrons tunnel back to the reservoir, leaving a unique electron in the dot. The barrier is raised until the potential is much higher than the right barrier, so that the trapped electron is ejected to the reservoir on the right side. The decay-cascade model [255,92] describes the process of back tunneling, and gives the framework for the understanding of the pumping cycle in a tunable barrier quantum dot. The single-electron transfer can be experimentally optimized by applying a non-sinusoidal signal to the gate V_{G1} [254] and a magnetic field B to obtain better electron confinement [256]. This non-adiabatic pumping cycle allows the control of the number of electrons pumped per cycle by varying the exit gate voltage V_{G2}. A quantized current step has been obtained by varying this parameter, as illustrated in Fig. 25c. At $T \leq 0.3$ K and $B \geq 14$ T, the quantization of the current was demonstrated with a relative measurement uncertainty of 1.2×10^{-6} at 150 pA ($f_P = 945$ MHz).

More recently, Stein and co-authors demonstrated the accuracy of a 96 pA current measured with an ultra-stable current amplifier. They reached a 1.6×10^{-7} relative combined uncertainty ($k = 1$) in a GaAs/AlGaAs device at $T = 0.1$ K and $B \geq 9.2$ T, ($f_P = 600$ MHz) [251]. The accuracy of single-electron pumping has also been improved recently in a metal-oxide-semiconductor silicon quantum dot driven by a 1-GHz sinusoidal wave in the absence of magnetic field, where a relative combined uncertainty of 2.7×10^{-7} ($k = 1$) [253] was achieved. Tunable barriers semiconductor pumps have improved the

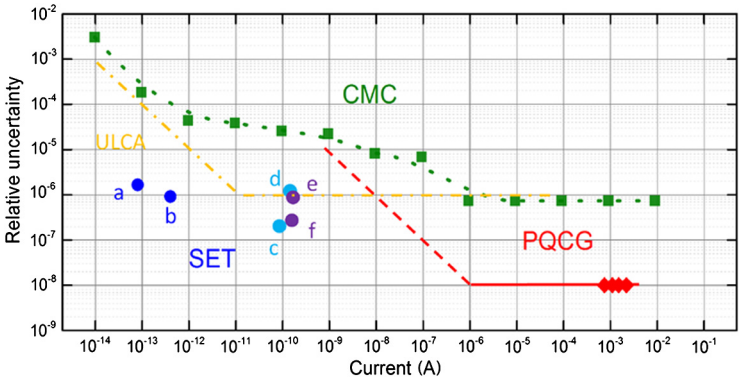

Fig. 26. Relative uncertainty for ampere traceability (measurement/generation). Uncertainties of SET devices (blue dots). Metallic SET: a [90], b [89]. GaAs SET: c [250], d [254]. Silicon SET: e [252], f [253]. Best calibration and measurement capabilities (CMCs) (green squares). From 10^{-14} up to 10^{-11} A by charging a capacitor ("Physikalisch-Technische Bundesanstalt"), from 10^{-10} up to 10^{-1} A by applying Ohm's law ("Laboratoire national de métrologie et d'essais") [260]. Uncertainties of the ULCA on a quarter (yellow dashed-dotted line) [261]. Uncertainty of the PQCG from 1 μA up to 10 mA (red line) and uncertainties demonstrated through comparisons in the milliampere range (red diamonds) [104]. Estimated uncertainty of the PQCG from 1 nA up to 1 μA (red dashed line). Uncertainties correspond to one standard deviation ($k = 1$).

uncertainties in the range below 1 nA as can be observed in Fig. 26. However, these new pumps do not yet constitute practical quantum current standards. A quantitative model of non-adiabatic effects in charge capture remains to be further developed [92]. Moreover, compared to QHR or JE standards, the amount of data confirming the robustness against variations of the operating parameters is low [251,253]. Quick characterizations that ensure that the quantification is at a certain level of uncertainty are still lacking.

To circumvent this difficulty, Fricke and co-authors have recently proposed self-referenced electron pumps equipped with a counting system of electron transfer errors based on additional quantum dots coupled with SET transistors [257,258]. In the meantime, there are attempts to use SET pumps, which are very low noise current source, for fundamental research in the field of single-electron optics [259].

3.2. Applying Ohm's law or charging capacitor

In NMIs, the traceability of current is realized by applying Ohm's law to secondary standards of voltage and resistance or charging a capacitor and calibrating the voltage at its terminals. Uncertainties claimed by NMIs in their best calibration and measurement capabilities (CMC), reported in Fig. 26, are not better than 10^{-6} above 1 μA, and are higher at lower current values [260]. Limitations come from the higher calibration uncertainties of secondary standards, although they are traceable to R_K and K_J constants, and the lack of sensitivity of the measurement methods below 1 μA. As shown in Fig. 26, the traceability of low currents was recently improved by an ultra-low current amplifier (ULCA) based on a more stable voltage to current converter [262,263,261]. This device demonstrated a better relative reproducibility over time: 10^{-7} over a week, a quarterly stability of 10^{-6} and a stability of 5×10^{-6} over a year. On the other hand, in the range of higher currents that covers the main calibration requests, no measurement improvement was expected until the development of a programmable quantum current generator.

3.3. The programmable quantum current generator

Very recently, a programmable quantum current generator (PQCG) based on the application of Ohm's law directly to the quantum voltage and resistance standards demonstrated quantized currents in terms of ef_J (f_J is a Josephson frequency) to within one part in 10^8 in the range from 1 μA up to a few mA [264,104]. This performance relies on the use of a cryogenic current comparator to detect and then amplify the current I_{PQCS} flowing in a QHR multiply-connected to a PJVS, as shown in Fig. 27a. The multiple (double in the figure) connection is used to drastically reduce the correction to the quantized current caused by the wire resistance: $I_{PQCS} = (U_J/R_H)(1-\alpha)$, where $U_J = n_J(h/2e)f_J$ is the Josephson voltage, n_J is the number of Josephson junction biased, $R_H = h/2e^2$ is the Hall resistance, and $\alpha \sim 2 \times 10^{-7} \pm 2.5 \times 10^{-9}$. Due to the chirality of the edge states in the QHE regime, the main part of the current I_{PQCS} circulates through a wire, while a minor part flows through the second wire. The total current is detected by two CCC windings of same number of turns N_{JK}, which are inserted in the two wires. A winding of number of turns N is connected to an external battery-powered current source delivering a current I_{PQCG}. The latter is servo-controlled by the CCC so that $N_{JK}I_{PQCS} - NI_{PQCG} = 0$. It results that the current of the generator is set to $I_{PQCG} = (N_{JK}/N)n_J ef_J(1-\alpha)$. Its amplitude can be modulated by varying either the gain $G = N_{JK}/N$ by four orders of magnitude or the number n_J between unity and several thousands or, more finely, the value of the frequency. An example of a sequence of on/off switching of the current (amplitude of ~ 1.1 mA) is given in Fig. 27b. The accuracy of the PQCG was determined in the milliampere range by comparing the voltage drop at the terminals of a 100-Ω resistor fed by the quantized current with a reference Josephson voltage. As shown in Fig. 27c, the PQCG current is quantized to its theoretical

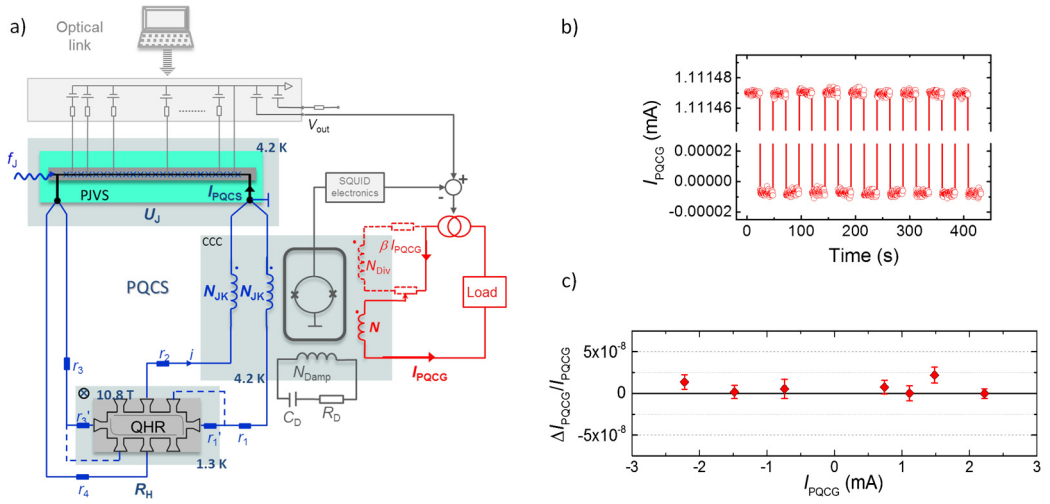

Fig. 27. (a) Schematic of the programmable quantum current generator (PQCG) developed by LNE: the current I_{PQCG} of the generator is servo-controlled by a CCC that detects and amplifies the current I_{PQCS} circulating through a QHR connected to a PJVS. (b) Sequence of switching on/off of the current I_{PQCG} generated by the PQCG (@ 1.1 mA). (c) Relative deviation $\Delta I_{PQCG}/I_{PQCG}$ of the current from its theoretical value in the milliampere range. From ref. [104].

value to within one part in 10^8 for current values between ± 2.2 mA. The relative standard deviation of the results amounts to 8×10^{-9} only. By principle, the current I_{PQCG} remains quantized with the same accuracy over the wide range of current values accessible by changing G, which is highly accurate and can span two orders of magnitude above or below the unity gain. Moreover, the relative current density noise S_I/I does not depend on G at a given value I_{PQCS}. Consequently, the PQCG can accurately generate currents with a combined relative measurement uncertainty of 10^{-8} in the whole range from 1 μA up to 10 mA, as illustrated in Fig. 26. A linear increase of the uncertainty is expected at lower currents.

This device provides an accurate realization of the new ampere definition. More fundamentally, the PQCG works as a multi-electron current pump. At each cycle of the external radio-frequency signal, n_J electrons are indeed transferred through the QHR device. This comes from the fact that a radio-frequency pulse irradiating the PJVS generates a quantized voltage pulse whose time-integral is equal to $n_J h/2e$. This results in a quantized current pulse corresponding to a total charge $n_J h/2e/(h/2e^2) = n_J e$. As discussed further below, this calls for considering the development of an AC quantum current source in future. Besides, the PQCG relies on an instrumentation yet available in NMIs equipped with a CCC resistance bridge and a PJVS. Thus, there is no additional cost for its realization.

As reported in Fig. 26, the PQCG improves the current traceability by two orders of magnitude. This new quantum current generator, which can be quickly validated by checking quantization criteria, was successfully used to calibrate a digital ammeter in ranges from 1 μA to 10 mA with a record uncertainty ($\sim 2 \times 10^{-7}$) only limited by the performance of the device itself.

Further reduction of uncertainty (down to 10^{-9}), extension of the current range and simplification are expected by implementing some improvements in the PQCG [104]. Moreover, the use of a graphene-based quantum Hall resistance standard will simplify its experimental conditions of operation. The PQCG should constitute a key element of the quantum calibrator based on a single cryogen-free system, described in section 4.4.

3.4. Future of the metrological triangle

Despite the adoption of the relationships $R_K = h/e^2$, $K_J = 2e/h$, and $Q = e$ in the revised SI, the metrological triangle experiment remains of fundamental and practical interest. Any highlighting of a discrepancy to the equation $R_K K_J Q = 2$ in the future would, of course, open a deep debate about quantum mechanics and would question the adoption of the individual relationships. Let us remember that tiny corrections (about 10^{-20} in relative value at 20 T) caused by a renormalization of the electron charge in the presence of a magnetic field have been predicted both for R_K and K_J by A.A. Penin [70,45] using quantum electrodynamics calculations. Regardless of such a hypothesis, this experiment keeps on being the best way to test the quantization of any single-electron pump.

3.5. A new ampere metrology

Current traceability is probably the field in electrical metrology where progress in accuracy will be the most important. As illustrated by Fig. 26, uncertainties of ampere realization have recently decreased by a factor of ten or one hundred in a range extending over more than 10 orders of magnitude. The PQCG offering highly-accurate current calibration, one can now consider the development of a new generation of stable transfer current source or ammeter. The ULCA [261] is an example of such a device. As shown in ref. [104], commercial digital precision multimeters operating in current mode could

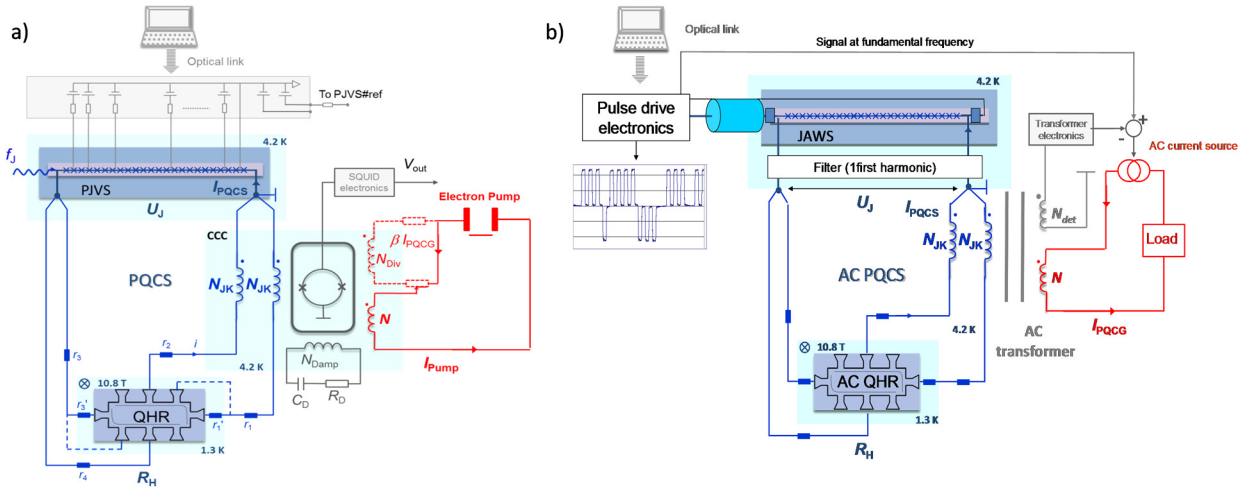

Fig. 28. (a) Principle of calibration of a current source (here, an electron pump) using a quantum ammeter. (b) Principle of a programmable quantum generator of alternating current.

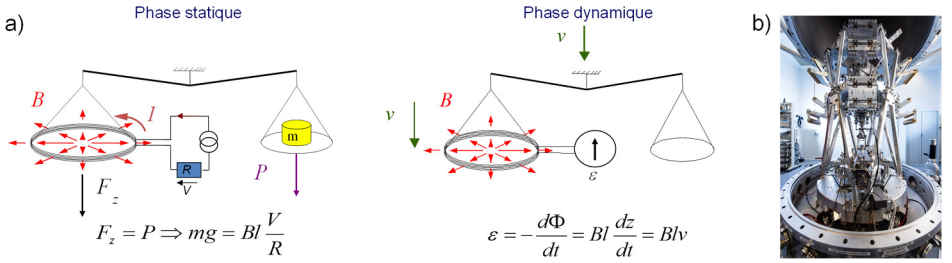

Fig. 29. a) Description of the two phases of the Kibble balance experiment. The mechanical power mgv is determined from the electrical power $\epsilon V/R$. b) Picture of the Kibble balance at LNE.

also constitute good transfer ammeters. A simplification and improvement of the traceability chain for current is therefore expected. This would benefit to the end-users by a reduction of uncertainty and a possible cost reduction.

The PQCG relies on the accurate exploitation by a CCC of a reference current I_{PQCS}. This principle is seminal and can be applied to other devices [264]. One can cite the quantum ammeter (Fig. 28a) based on the direct comparison of the current generated by a device under test (DUT) with the reference current. Ultra-accurate universality tests of the QHE can be performed by comparing, using the CCC, two reference currents obtained from the same Josephson voltage and two different quantum Hall resistors. Finally, the PQCG can be adapted to audio-frequency alternating current (Fig. 28b) by replacing the CCC by a magnetic transformer and the PJVS by a pulse-driven Josephson array. To conclude, the availability of a quantum current source opens the way to a renewed metrology of the ampere.

4. New applications of quantum standards

4.1. The Kibble balance or the quantum kilogram

One emblematic application of the quantum electrical standards, which stimulated the revolution of the SI [265], is the realization of the kilogram from the Planck constant h using a Kibble balance [266]. As yet mentioned, this experiment consists in measuring the mechanical power of a mass m moving at a velocity v under the gravitational acceleration g in terms of an electric power in a coil calibrated using the Josephson constant K_J and the von Klitzing constant R_K. In practice, this measurement has two phases (Fig. 29a): the mechanical force is first balanced by the magnetic force resulting from the circulation of a current I in a coil under a radial magnetic induction B in the static phase, the voltage at the terminal of the coil moving at a velocity v is then recorded in the dynamic phase. Measurements of both phases are combined to cancel the geometrical factor l of the coil used, which leads to the power comparison. Adoption of the theoretical relationships $K_J = 2e/h$ and $R_K = h/e^2$ in the SI provides a direct link between mass and Planck constant according to $m = h\frac{A}{4gv}$, where A is a quantity involving Josephson frequencies, the number of Josephson junctions, and the Hall plateau index. After participating in h determinations [102], it is now a question of using Kibble's balances, notably those having participated in the determination of h from NIST [267], NRC [268], and LNE (Fig. 29b) [269], to calibrate mass standards with a 10^{-8} relative uncertainty from the Planck constant value [101] $h = 6.62607015 \times 10^{-34}$ J·s. This extension of the application

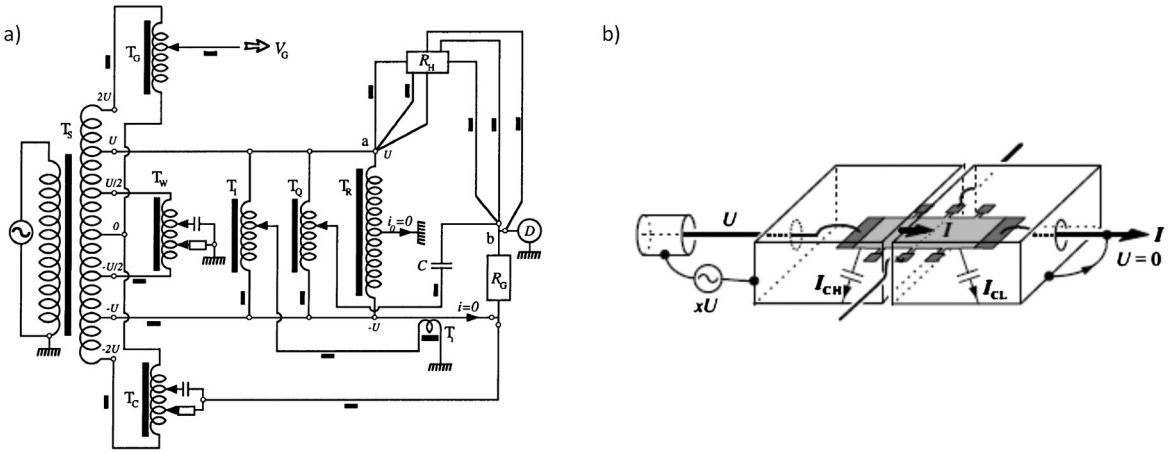

Fig. 30. (a) Schematic of a resistance bridge used in AC regime. ©2003 IEEE. Reprinted, with permission, from ref. [274]. (b) Double shielding of a Hall bar for operation in AC regime. Reproduced by permission of IOP publishing from ref. [273].

of solid-state quantum effects beyond electrical metrology is to benefit from the user-friendly graphene-based quantum resistance standard and cryogen-free cooling techniques.

4.2. Quantum impedance standard

The Hall resistance being expected [270,271] to remain quantized within one part in 10^9 at frequencies in the kilohertz range, an important field of research has therefore been to realize a quantum resistance standard operating in alternating current (AC). Targeted applications are traceability of AC resistance and more generally of impedances.

4.2.1. AC quantum Hall effect

The study and implementation of the AC QHE relies on the development of terminal-pair resistance bridges and quadrature bridges that are based on the coaxial measurement techniques [4]. As shown in Fig. 30a, specific techniques are used to preserve a perfect quantization of the Hall resistance. Firstly, the Hall bar is implemented using the multiple series connection technique. On the one hand, this technique cancels large quadratic frequency dependencies due to series inductance, but also simplifies the bridge since zero current requirement in the voltage arm of the QHR is automatically ensured [272, 274]. Given the high impedance of the shielding conductors connecting the QHR at low temperature, active equalizers are used to ensure a good coaxiality. Despite these precautions, several works have highlighted a residual deviation of the Hall resistance from its quantized value that linearly increases with frequency and measurement current [275]. This discrepancy, which can amount to about a few 10^{-8} at 1 kHz, is linearly coupled with the longitudinal resistance, as often observed in DC regime. Its origin is attributed to losses of AC charging current in internal capacitances of the Hall bar and in external capacitances of coupling with ground. However, it is possible to cancel its impact on the Hall resistance to within about one part in 10^9 per kilohertz by using a double-shielding technique [273] of the Hall bar, as described in Fig. 30b.

Given the robustness of the QHE in graphene, it was attractive to perform studies in graphene-based Hall bars. In 2014, Kalmbach and co-authors showed that large quantum Hall plateaus measured with alternating current were flat within one part in 10^7. Moreover, they measured an intrinsic frequency dependence similar in magnitude to that of GaAs devices [235]. Owing to graphene, a more user-friendly quantum standard for both resistance and impedance is therefore expected.

4.2.2. Impedance calibration

Operation of the QHE in AC regime at frequencies of a few kilohertz has opened up the way towards a quantum standard of impedance [276,277] linked to the constant R_K. In 2009, J. Schurr and B. Kibble [7] demonstrated a new way to realize the unit of farad by calibrating a capacitance from two quantum Hall resistances used in a quadrature bridge with a relative measurement uncertainty of 6×10^{-9}. This method provides a direct realization of the farad from R_K, which avoids an additional calibration step relying on calculable resistors [278,279]. However, the calibration of impedance requires very precise comparison bridges that are usually based on inductive voltage dividers (IVD) [4,280]. Even though they can reach uncertainties of a few parts in 10^9, their measurement capabilities are limited to pure impedances. Furthermore, the ratio of the measured impedances is restricted to a few fixed nominal ratios like 1:1 and 10:1. Finally, these impedance bridges require realizing a long and tedious calibration of the IVDs at each ratio and frequency used. The recent development of pulse-driven Josephson voltage standards [155,281,176] able to generate sine waves with high spectral purity, now makes possible the comparison of arbitrary impedances at the same level of uncertainty as the IVD's bridges over a wider frequency range. The ratio of the bridge is then defined by two pulse-driven Josephson series arrays adjustable in magnitude and phase offering very high accuracy, and the possibility to compare any kind of impedance at frequencies up to 40 kHz [282]. Using such a technology, S. Bauer and co-authors [283] performed the calibration of a capacitance from R_K: two pulse-driven

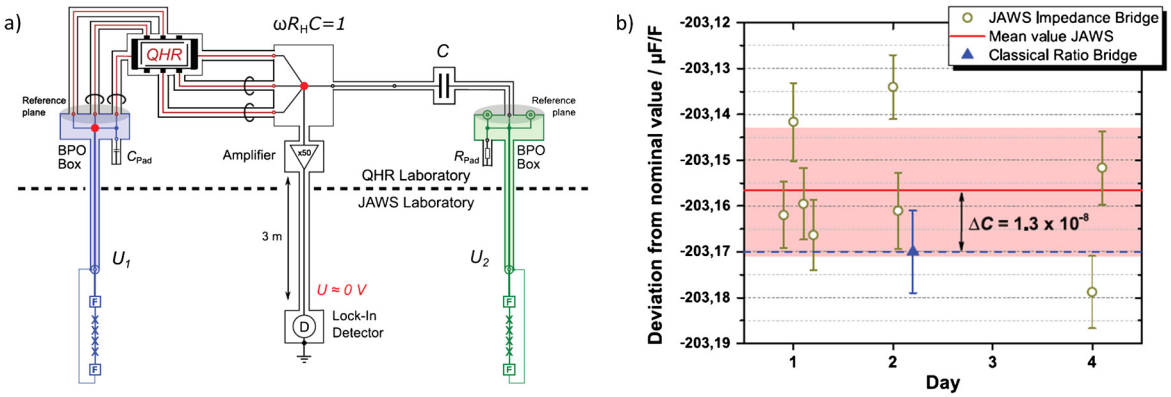

Fig. 31. (a) Schematic overview of the quadrature bridge for measuring a 10-nF capacitance standard from the quantum Hall resistance. The two reference voltages U_1 and U_2 defining the standard ratio of the bridge are provided by two pulse-driven Josephson voltage standards. (b) Comparison of the results obtained with the pulse-driven Josephson bridge (open circle) and with a classical impedance bridge (filled triangle). Error bars correspond to one standard deviation ($k = 1$). Reproduced by permission of IOP publishing from ref. [283].

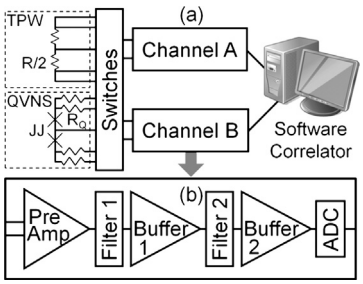

Fig. 32. Schematic of the QVNS–JNT cross-correlation electronics. (a) Two channels (A and B) of the correlator that simultaneously measure one of the two voltage sources. The switching network alternates between the two input signals. (b) Each channel consists of a series of amplifiers and filters, followed by an analogue-to-digital converter (ADC). The digitized signals from each channel are optically transmitted to the computer that performs the correlation analysis. Reproduced by permission of IOP publishing from ref. [289].

Josephson voltage standards and one quantum Hall resistor were involved in the experiment (Fig. 31a). They demonstrated an agreement of the measurements with those performed using classical bridges within about 1.3 parts in 10^8 (Fig. 31b). Further progress in the experimental conditions of operation of graphene-based QHE devices, *i.e.* reduction of the magnetic induction below 2 T, should allow in a near future that Josephson voltage standard and QHE devices could operate in the same cryogen-free cryostat. This would support the development of a user-friendly quantum standard ensuring impedance calibration in the whole complex plane.

4.3. Quantum electronic kelvin

Johnson noise thermometry (JNT) [284] is a primary thermometry based on the Johnson–Nyquist noise of a resistor R [285,286]. This noise results from the fluctuation–dissipation theorem, which predicts a relation between the resistance and the thermal voltage fluctuations in a conductor due to the random thermal motion of the electrons. For a temperature T, the mean-squared voltage noise is given by Nyquist's equation:

$$\overline{V_T^2} = 4kTR\Delta f \tag{8}$$

where k is the Boltzmann's constant and Δf is the bandwidth of the measurements.

Experimentally, the JNT is used to infer a temperature by comparing the mean-square noise voltage measured at the terminals of a first resistor at the unknown temperature and of a second resistor at a reference temperature. By this way, the calibration of the measurement chain, notably the bandwidth Δf, is circumvented. Due to the extremely small voltages, of only 1.2 nV/$\sqrt{\text{Hz}}$ for a resistance of 100 Ω at 273.16 K (triple point of water), cross-correlation techniques are used. Cross-correlation is needed because the small noise voltage is comparable to the noise of the low-noise amplifier. In 2003, Benz et al. [287,288] proposed to replace the reference calibrated resistor by a JAWS (Fig. 32). The requirements for the JAWS system in JNT experiment contrast with those in AC voltage metrology, where the challenge is to increase the output amplitude. Here, the JAWS system has been designed to produce multi-tone pseudo-noise waveforms with small (1 μV peak) voltage amplitudes (a few JJs) [289] approximately matched to the expected Johnson noise. The quantum voltage noise source (QVNS) is a comb of harmonic tones (MHz range), equally spaced in frequency, of identical amplitudes and random

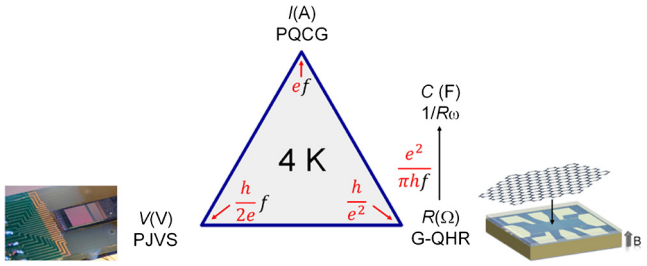

Fig. 33. Illustration of a quantum calibrator realizing the electrical units (A, V, Ω, F) from h, e, and the frequency f. It is based on a programmable Josephson voltage standard (PJVS) and a graphene-based quantum Hall resistance standard (G-QHR). The ampere is realized using the programmable quantum current generator (PQCG). The farad is realized from the G-QHR using a quadrature bridge.

relative phases [290]. The different improvements of the QVNS–JNT lead to high-precision temperature measurements, which were used to determine the Boltzmann's constant [289,291–293]. The lowest uncertainty with this technique was achieved by Qu et al. [293] with a relative uncertainty of 2.7 parts in 10^6.

4.4. The quantum calibrator

The quantum calibrator consists in a user-friendly device realizing accurately the main electrical units, *i.e.* the ampere, the volt, the ohm, and the farad from the Planck constant h and the elementary charge e only (Fig. 33). Until recently, this ambitious idea was facing several difficulties. The first one was that the relationships of the fundamental constants Q, K_J and R_K with h and e were spoiled by large uncertainties. The revised SI solves this problem. The second critical problem was that the three quantum devices used to realize the units were operating in very different experimental conditions, which forbade their implementation in a single cryostat: $T = 4.2$ K and $B = 0$ T for the Josephson array, $T < 2$ K and $B \sim 10$ T for the quantum Hall bar, and $T < 0.3$ K and $B \sim 10$ T for the recent SET devices. After the many works carried out in the last ten years, this difficulty is being solved. At first, it was demonstrated that a graphene-based quantum resistance standard can operate at a temperature $T \geq 4.2$ K and a magnetic induction $B \simeq 3.5$ T. These conditions are now closer from those required by a Josephson array. Second, the PQCG now offers a 10^{-8}-accurate realization of the ampere with adapted current values to calibrations centers that is only based on the Josephson and quantum Hall resistance standards. This avoids the supplementary experimental constraints imposed by SET devices, which besides have not yet managed to realize the ampere with the required accuracy and reproducibility. These results give hope that further progress, concerning the graphene growth for achieving an even lower operational magnetic field (hopefully less than 1 T) and some engineering works to screen small magnetic field, should allow the development of a device based on a Josephson array and a quantum Hall resistance standard only. The third difficulty was to realize the farad from the QHE operating in ac without referring to calculable coaxial resistors. Calibration in such way of a capacitance was demonstrated with a relative uncertainty of a few 10^{-9} using an adapted quadrature bridge. Finally, the availability of cryogen-free cryostats with a base temperature lower than 4.2 K makes easier and less-costly the operation of quantum devices. Thus, the quantum calibrator is no longer just an idea, but now becomes a project in many NMIs to support a high-accuracy dissemination of the electrical units towards the end-users.

5. Further perspectives

Advances in metrology have always closely followed the scientific and technological discoveries. Let us evoke recent works that could be promising for electrical metrology.

Mooij and Nazarov [294] suggested to use quantum phase slips in disordered superconducting nanowires to realize a quantized current source, which could produce larger currents. Phase slip events occur in low-dimension superconductors where thermodynamic fluctuations of the order parameter become significant. When a phase slip occurs at some point in the wire, the superconducting order parameter vanishes locally. The phase difference changes by 2π over the wire and this gives rise to a quantized voltage pulse. If the phase slips happen frequently, they produce a finite dc voltage or a finite resistance. Well below T_c, the phase of a homogeneous superconducting wire can slip by 2π due to quantum tunneling, a process analogous to Cooper-pair tunneling in Josephson junctions. The quantum phase-slip junction is formally the exact dual of the Josephson junction with respect to the exchange of the canonically conjugated quantum variables, phase, and charge. Hence, Eq. (3) can be rewritten for the charge instead of the phase by considering a dual circuit, where the capacitance and the resistance shunting the JJ are replaced by an inductance and a resistance in series with the quantum phase-slip junction. Mapping the problem of the Josephson junction, dual-Shapiro steps have been predicted in ultrathin superconducting nanowires with sufficiently high series resistance submitted to microwave irradiation. Although, very promising, these dual Shapiro steps have not been observed yet [295]. However, coherent quantum phase slips have been unambiguously observed by spectroscopy, in narrow nanowires of strongly disordered superconductors near the superconductor/insulator transition, integrated in a superconducting loop coupled with a coplanar resonator [296]. More recently, the dual of the SQUID has been demonstrated in a device that integrates several coherent quantum phase-slip junctions [297].

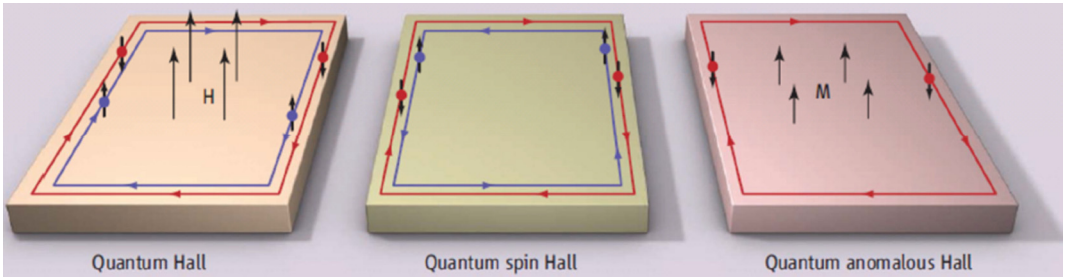

Fig. 34. Edge states in the three quantum Hall effects. The usual quantum Hall effect (left): electrons with opposite spin move in the same direction. The spin quantum Hall effect (center): electrons with opposite spin move in opposite directions. The anomalous quantum Hall effect (right): electrons moving along an edge have a defined spin direction (here spin down). From ref. [300]. Reprinted with permission from AAAS.

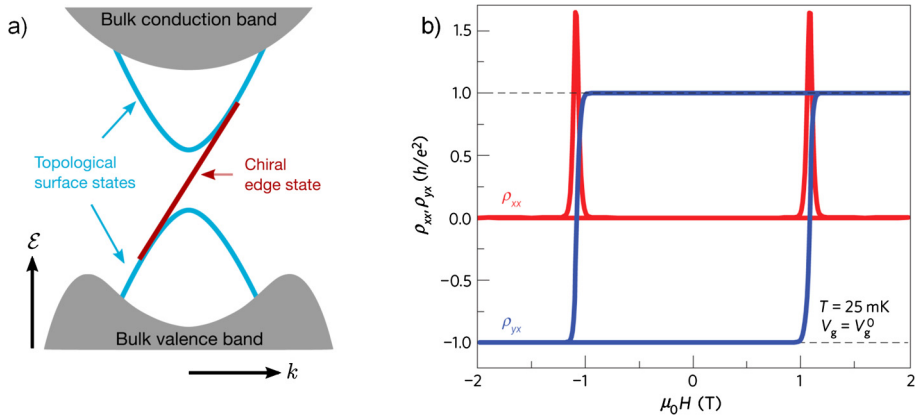

Fig. 35. (a) Schematic energy spectrum $\epsilon(k)$ of a FTI in the QAHE state. Reprinted with permission from ref. [303]. Copyright (2018) by the American Physical Society. (b) Observation of the QHAE in a 4-quintuple Layer of $(Bi_{0.29}Sb_{0.71})_{1.89}V_{0.11}Te_3$ at 25 mK. Longitudinal resistivity ρ_{xx} and transverse resistivity ρ_{xy} *versus* B at the charge neutrality point $V_g = V_g^0$. Reprinted by permission of Springer Nature from ref. [304], ©2015.

The observation of gigahertz quantized charge pumping in graphene quantum dots [298] and the recent discovery of superconductivity in magic-angle graphene superlattices [299] could enable the use of graphene as a common material platform for developing not only the QHR, but also voltage and current quantum standards. The ideal goal would even be to integrate several quantum standards on a single graphene chip, although this requires a magnetic field of operation of the QHE low enough to preserve the superconductivity in Josephson devices.

The discovery of the quantum anomalous Hall Effect (QAHE), which manifests itself by the Hall resistance quantization at zero magnetic field [300], opens another way to get in a single cryostat both the QHR and the Josephson array. Generally, the QHE relies on the existence of chiral edge states having opposite momentum on both sides of a sample, which suppresses electron backscattering, *i.e.* dissipation (Fig. 34, left). One fundamental question was to know whether dissipationless states can exist without a magnetic field. Following some theoretical predictions supporting this hypothesis [301], the discovery of the spin quantum Hall effect brought the demonstration of dissipationless edge states where electrons of opposite spin directions are counterpropagating as a result of a strong spin–orbit coupling [302] (Fig. 34, center). The QAHE corresponds to the fundamental state where only one spin direction edge-state is kept (Fig. 34, right), which can be achieved by introducing ferromagnetism. As described in Fig. 35a from ref. [303], the gapless chiral edge state is hosted in the exchange-induced gap in the Dirac spectrum of the topological surface states inside the 3D bulk gap. The Hall resistance is quantized for a Fermi level in the surface-state gap. This new quantum Hall effect was first observed in 2013 in a thin ferromagnetic topological insulator (FTI) [305]. Fig. 35b reports on the dependence of the Hall and longitudinal resistances as a function of the magnetic induction in a 4-quintuple layer of $(Bi_{0.29}Sb_{0.71})_{1.89}V_{0.11}Te_3$ at a temperature $T = 25$ mK. It shows a hysteresis cycle and flat Hall plateaus centered around $B = 0$ T. The quantization of the Hall resistance was demonstrated to within a few 10^{-4} at $B = 0$ T. A similar accuracy was obtained in ref. [306].

Accurate comparisons of the Hall resistances measured both in a FTI at zero magnetic field and in a GaAs-based reference standard were recently performed using a CCC-based resistance bridge. Actually, Fox and co-authors [303] have demonstrated the quantization of the Hall resistance with a relative uncertainty of about one part in 10^6 at a temperature of 21 mK for a measurement current of 100 nA in a top-gated 100-μm-wide Hall bar made of a 6-quintuple-layer sample of $Cr_{0.12}(Bi_{0.26}Sb_{0.62})_2Te_3$ grown on a GaAs substrate by molecular beam epitaxy (MBE). Limitations in temperature and current are explained by an effective energy gap much lower than expected and strong electron heating in bulk current flow, respectively. Götz and co-authors determined a relative discrepancy of $(0.17 \pm 0.25) \times 10^{-6}$ between the von Klitzing constant R_K and the quantized resistance measured, at a temperature of 20 mK and for currents lower than 10 nA, in a top-

gated 200-µm-wide Hall bar made of a 9-nm-thick film of the ferromagnetic topological insulator $V_{0.1}(Bi_{0.21}Sb_{0.79})_{1.9}Te_3$ grown by MBE on a hydrogen-passivated Si(111) substrate [307]. These recent results support the topological robustness of the QAHE and motivate further works to investigate its metrological application. Beyond, non-dissipative edge states at zero magnetic field in the QHAE instigate other interests, notably applications in low-consumption electronics.

Generally, electrical metrology looks after quantum effects, with a very rich physics, which are of interest not only for fundamental research, but also for applications. It turns out that the integration of quantum physics in the SI occurs simultaneously with an ambition of exploiting new quantum technologies in industry. It is about using individual particles, superposed coherent states or entangled states as a basis for a quantum computer, protected communications, and more sensitive detectors. In this context, new measurement methods will be needed. Their development can rely on the knowhow of NMIs in the field of quantum effects. As an example of new quantum technology, one can cite single-electron interferometers as local sensitive electromagnetic field detectors [308], for which expertise of NMIs in SET and QHE physics should constitute a clear support to their development and characterization.

6. Conclusions

The quantum voltage and resistance standards have greatly progressed since the discovery of the Josephson effect and of the quantum Hall effect. They have become pillars of the electrical metrology, allowing a traceability improvement for all basic electrical units, *i.e.* the volt, the ohm, the ampere, and the farad, but also the kilogram. This comes from the richness and universality of these two quantum phenomena. Pulse-driven Josephson arrays and graphene-based standards are recent examples of this fruitfulness for which short-term issues are the achievement in a reproducible way of 1-V and even 10-V pulse-driven voltage standards and of a stable low-magnetic field QHR, respectively. Quantum standards having reached a certain level of maturity, one of the future issues will be to combine them together to develop new applications. The development of the quantum standards of impedance and current based on Ohm's law illustrates this new research direction. The quantum calibrator probably constitutes an emblematic challenge because it is the key for disseminating electrical units closer to end-users. We have evoked some recent scientific discoveries able to support the development of this device. Beyond, national metrology institutes, as experts of measurements, should be associated with this ambition of developing new quantum technologies for industry. As always, success in this new metrological challenge would rely on a close collaboration between NMIs, academic laboratories, and relevant high-technology industries.

Acknowledgements

This work was supported by the Joint Research Projects 'e-SI-Amp' (15SIB08) and 'Sequoia' (17FUN04). It received funding from the European Metrology Programme for Innovation and Research (EMPIR), co-financed by the Participating States, and from the European Union's Horizon 2020 research and innovation programme. This work was supported by the French Agence Nationale de la Recherche (ANR-16-CE09-0016).

References

[1] BIPM, Resolutions of the CGPM: 11th meeting (11-20 October 1960). https://www.bipm.org/en/CGPM/db/11.
[2] BIPM, The International System of Units (SI) [8th edition, 2006; updated in 2014]. https://www.bipm.org/en/measurement-units.
[3] P. Vigoureux, A determination of the ampere, Metrologia 1 (1965) 3.
[4] S. Awan, B. Kibble, J. Schurr, Coaxial Electrical Circuits for Interference-Free Measurements, The Institution of Engineering and Technology, New York, 2011.
[5] G. Trapon, O. Thévenot, J.C. Lacueille, G. Genevès, Realization of the farad at bnm-lcie, in: CPEM 1998 Conf. Digest, 1998, p. 448.
[6] G. Trapon, O. Thévenot, J. Lacueille, W. Poirier, Determination of the von Klitzing constant R_K in terms of the BNM calculable capacitor – fifteen years of investigations, Metrologia 40 (2003) 159–171.
[7] J. Schurr, V. Burkel, B.P. Kibble, Realizing the farad from two ac quantum Hall resistances, Metrologia 46 (2009) 619.
[8] W. Clothier, A calculable standard of capacitance, Metrologia 1 (2) (1964) 35–56.
[9] F. Delahaye, A. Fau, D. Dominguez, M. Bellon, Absolute determination of the farad and the ohm, and measurement of the quantized Hall resistance $r_H(2)$ at lcie, IEEE Trans. Instrum. Meas. IM-36 (1987) 205.
[10] G.W. Small, B.W. Ricketts, P.C. Coogan, B.J. Pritchard, M.M.R. Sovierzoski, A new determination of the quantized Hall resistance in terms of the NML calculable cross capacitor, Metrologia 34 (1997) 241.
[11] A.M. Thompson, D.G. Lampard, A new theorem in electrostatics with applications to calculable standards of capacitance, Nature 177 (1956) 888–890.
[12] A. Jeffery, R.E. Elmquist, J.Q. Shields, L.H. Lee, M.E. Cage, S.H. Shields, R.F. Dziuba, Determination of the von Klitzing constant and the fine-structure constant through a comparison of the quantized Hall resistance and the ohm derived from the NIST calculable capacitor, Metrologia 35 (83) (1998).
[13] W. Clothier, G. Sloggett, H. Bairnsfather, M. Currey, D. Benjamin, A determination of the volt, Metrologia 26 (1989) 9–46.
[14] T. Funck, V. Sienknecht, Determination of the volt with the improved PTB voltage balance, IEEE Trans. Instrum. Meas. 40 (158) (1991).
[15] I.M. Mills, P.J. Mohr, T.J. Quinn, B.N. Taylor, E.R. Williams, Redefinition of the kilogram: a decision whose time has come, Metrologia 42 (2) (2005) 71–80.
[16] I.M. Mills, P.J. Mohr, T.J. Quinn, B.N. Taylor, E.R. Williams, Redefinition of the kilogram, ampere, kelvin and mole: a proposed approach to implementing CIPM recommendation 1, Metrologia 43 (2006) 227–246.
[17] M.J.T. Milton, J.M. Wiliams, S.J. Bennett, Modernizing the SI: towards an improved, accessible and enduring system, Metrologia 44 (2007) 356–364.
[18] BIPM, On the revision of the SI. Draft of the ninth SI Brochure, 2019. https://www.bipm.org/utils/en/pdf/si-revised-brochure/Draft-SI-Brochure-2019.pdf.
[19] G.D. Mahan, Many-Particles Physics, Springer US, New York, 1981.
[20] C. Kittel, Introduction to Solid State Physics, Wiley, New York, 1966.

[21] C. Kittel, Quantum Theory of Solids, Wiley, New York, 1987.
[22] J. Bardeen, L.N. Cooper, J.R. Schrieffer, Theory of superconductivity, Phys. Rev. 108 (1957) 1175.
[23] B. Josephson, Possible new effects in superconductive tunnelling, Phys. Lett. 1 (1962) 251.
[24] R. Landauer, Spatial variation of currents and fields due to localized scatterers in metallic conduction, IBM J. Res. Dev. 1 (1957) 223.
[25] B.J. van Wees, H.V. Houten, C.W.J. Beenakker, J.G. Williamson, L.P. Kouwenhoven, D.V. der Marel, C.T. Foxon, Quantized conductance of point contacts in a two-dimensional electron gas, Phys. Rev. Lett. 60 (1988) 848.
[26] P.W. Anderson, Absence of diffusion in certain random lattices, Phys. Rev. 109 (1958) 1492.
[27] E.A. Abrahams, P. Anderson, D.C. Licciardello, T.V. Ramakrishnan, Scaling theory of localization: absence of quantum diffusion in two dimensions, Phys. Rev. Lett. 42 (1979) 673.
[28] D.V. Averin, K.K. Likharev, Coulomb blockade of single-electron tunneling, and coherent oscillations in small tunnel junctions, J. Low Temp. Phys. 62 (1986) 345.
[29] K. von Klitzing, G. Dorda, M. Pepper, New method for high-accuracy determination of the fine-structure constant based on quantized Hall resistance, Phys. Rev. Lett. 45 (1980) 494.
[30] K.K. Likharev, A.B. Zorin, Theory of the Bloch-wave oscillations in small Josephson junctions, J. Low Temp. Phys. 59 (1985) 347.
[31] B.D. Josepshon, Phys. Rev. Lett. 1 (1962) 251.
[32] S. Shapiro, Josephson currents in superconducting tunneling: the effect of microwaves and another observations, Phys. Rev. Lett. 11 (1963) 80–82.
[33] W.C. Stewart, Current-voltage characteristics of Josephson junctions, Appl. Phys. Lett. 12 (8) (1968) 277–280, https://doi.org/10.1063/1.1651991.
[34] D.E. McCumber, Effect of ac impedance on dc voltage-current characteristics of superconductor weak-link junctions, J. Appl. Phys. 39 (7) (1968) 3113–3118, https://doi.org/10.1063/1.1656743.
[35] R.L. Kautz, Quasipotential and the stability of phase lock in nonhysteretic Josephson junctions, J. Appl. Phys. 76 (1994) 5538.
[36] R.L. Kautz, Noise, chaos, and the Josephson voltage standard, Rep. Prog. Phys. 59 (1996) 935.
[37] R.L. Kautz, Design and operation of series-array Josephson voltage standards, in: L. Crovini, T.J. Quinn (Eds.), Metrology at the Frontiers of Physics and Technology, North-Holland, Amsterdam, 1992, pp. 259–296.
[38] R.L. Kautz, Shapiro steps in large-area metallic-barrier Josephson junctions, J. Appl. Phys. 78 (9) (1995) 5811–5819, https://doi.org/10.1063/1.359644.
[39] J. Clarke, Experimental comparison of the Josephson voltage-frequency relation in different superconductors, Phys. Rev. Lett. 21 (1968) 1566–1569, https://doi.org/10.1103/PhysRevLett.21.1566, https://link.aps.org/doi/10.1103/PhysRevLett.21.1566.
[40] J.S. Tsai, A.K. Jain, J.E. Lukens, High-precision test of the universality of the Josephson voltage-frequency relation, Phys. Rev. Lett. 51 (1983) 316.
[41] A.K. Jain, J.E. Lukens, J.S. Tsai, Test for relativistic gravitational effects on charged particles, Phys. Rev. Lett. 58 (1987) 1165.
[42] F. Bloch, Simple interpretation of the Josephson effect, Phys. Rev. Lett. 21 (17) (1968) 1241–1243.
[43] F. Bloch, Josephson effect in a superconducting ring, Phys. Rev. B 2 (1970) 109.
[44] T.A. Fulton, Implications of solid-state corrections to the Josephson voltage–frequency relation, Phys. Rev. B 7 (3) (1973) 981–982.
[45] A.A. Penin, Measuring vacuum polarization with Josephson junctions, Phys. Rev. Lett. 104 (2010) 097003.
[46] B.N. Taylor, W.H. Parker, D.N. Langenberg, A. Denenstein, On the use of the ac Josephson effect to maintain standards of electromotive force, Metrologia 3 (4) (1967) 89, http://stacks.iop.org/0026-1394/3/i=4/a=001.
[47] B.F. Field, T.F. Finnegan, J. Toots, Volt maintenance at nbs via $2e/h$: a new definition of the NBS volt, Metrologia 9 (4) (1973) 155, http://stacks.iop.org/0026-1394/9/i=4/a=003.
[48] T. Witt, 100 Years of Superconductivity, Taylor and Francis, London, 2011.
[49] C.W.J. Beenakker, H. van Houten, Quantum transport in semiconductor nanostructures, Solid State Phys. 44 (1991) 1.
[50] K. von Klitzing, A personal view on the discovery. Physics and application of this quantum effect, in: Séminaire Poincaré 2: 25 Years of Quantum Hall Effect (QHE), 2004, p. 1.
[51] B. Douçot, V. Pasquier, Physics in strong magnetic field, in: Séminaire Poincaré 2: 25 years of Quantum Hall Effect (QHE), 2004, p. 17.
[52] M. Buttiker, S.E. Nigg, Role of coherence in resistance quantization, Eur. Phys. J. Spec. Top. 172 (2009) 247.
[53] M. Janben, O. Viehweger, Introduction to the Theory of the Integer Quantum Hall Effect, Wiley and Sons, New York, 1994.
[54] S.M. Girvin, The Quantum Hall Effect: Novel Excitations and Broken Symmetries, Springer Verlag and Les Éditions de physique, Paris, 1999.
[55] D. Yoshioka, The Quantum Hall Effect, Springer, 1998.
[56] M.O. Goerbig, P. Lederer, Lecture Notes: Introduction to the Quantum Hall Effects, University of Paris-11, 2006.
[57] B. Huckestein, Scaling theory of the integer quantum Hall effect, Rev. Mod. Phys. 67 (1995) 357.
[58] A. Pruisken, Universal singularities in the integral quantum Hall effect, Phys. Rev. Lett. 61 (1988) 1297.
[59] F. Evers, A. Mirlin, Anderson transitions, Rev. Mod. Phys. 80 (2008) 1355.
[60] R. Landauer, Electrical resistance of disordered one-dimensional lattices, Philos. Mag. 21 (2011) 863.
[61] D.C. Glattli, Quantum shot noise of conductors and general noise measurement methods, Eur. Phys. J. Spec. Top. 172 (2009) 163.
[62] M. Buttiker, Y. Imry, R. Landauer, S. Pinhas, Generalized many-channel conductance formula with application to small rings, Phys. Rev. B 31 (1985) 6207.
[63] M. Buttiker, Absence of backscattering in the quantum Hall effect in multiprobe conductors, Phys. Rev. B 38 (1988) 9375.
[64] R.B. Laughlin, Quantized Hall conductivity in two dimensions, Phys. Rev. B 23 (1981) 5632.
[65] Q. Niu, D.J. Thouless, Y. Wu, Quantized Hall conductance as a topological invariant, Phys. Rev. B 31 (1985) 3372.
[66] D.J. Thouless, Topological interpretations of quantum Hall conductance, J. Math. Phys. 35 (1994) 5362.
[67] G. Watson, Hall conductance as a topological invariant, Contemp. Phys. 37 (1996) 127.
[68] D.R. Yennie, Integral quantum Hall effect for nonspecialists, Rev. Mod. Phys. 59 (1987) 781.
[69] F.W. Hehl, Y.N. Obukhov, B. Rosenow, Is the quantum Hall effect influenced by the gravitational field?, Phys. Rev. Lett. 93 (2004) 096804.
[70] A.A. Penin, Quantum Hall effect in quantum electrodynamics, Phys. Rev. B 79 (2009) 113303, Erratum, Phys. Rev. B 81 (2010) 089902.
[71] F. Schopfer, W. Poirier, Testing universality of the quantum Hall effect by means of the Wheatstone bridge, J. Appl. Phys. 102 (2007) 054903.
[72] A. Hartland, K. Jones, J.M. Williams, B.L. Gallagher, T. Galloway, Direct comparison of the quantized Hall resistance in gallium arsenide and silicon, Phys. Rev. Lett. 66 (1991) 969.
[73] B. Jeckelmann, A.D. Inglis, B. Jeanneret, Material, device, and step independence of the quantized Hall resistance, IEEE Trans. Instrum. Meas. 44 (1995) 269.
[74] B. Jeckelmann, B. Jeanneret, The quantum Hall effect as an electrical resistance standard, Rep. Prog. Phys. 64 (2001) 1603.
[75] F. Delahaye, D. Domingez, F. Alexandre, J.-P. André, J.-P. Hirtz, M. Razeghi, Precise quantized Hall resistance measurements in GaAs/$Al_xGa_{1-x}As$ and $In_xGa_{1-x}As$/InP heterostructures, Metrologia 22 (1986) 103.
[76] T.J.B.M. Janssen, N. Fletcher, R. Goebel, J. Williams, A. Tzalenchuk, R. Yakimova, S. Kubatkin, S. Lara-Avila, V. Falko, Graphene, universality of the quantum Hall effect and redefinition of the SI system, New J. Phys. 13 (2011) 093026.
[77] R. Ribeiro-Palau, F. Lafont, J. Brun-Picard, D. Kazazis, A. Michon, F. Cheynis, O. Couturaud, C. Consejo, B. Jouault, W. Poirier, F. Schopfer, Quantum Hall resistance standard in graphene devices under relaxed experimental conditions, Nat. Nanotechnol. 10 (2015) 965–971.
[78] B. Jeckelmann, B. Jeanneret, D. Inglis, High-precision measurements of the quantized Hall resistance: experimental conditions for universality, Phys. Rev. B 55 (1997) 13124.

[79] B. Jeckelmann, A. Rüfenacht, B. Jeanneret, F. Overney, A. von Campenhausen, G. Hein, Optimization of qhe-devices for metrological applications, IEEE Trans. Instrum. Meas. 50 (2001) 218.
[80] B. Jeanneret, B. Jeckelmann, H.J. Buhlman, B. Houdré, M. Llegems, Influence of the device-width on the accuracy of quantization in the integer quantum Hall effect, IEEE Trans. Instrum. Meas. 44 (1995) 254.
[81] P. Lafarge, H. Pothier, E.R. Williams, D. Esteve, C. Urbina, M.H. Devoret, Direct observation of macroscopic charge quantization, Z. Phys. B, Condens. Matter 85 (3) (1991) 327–332, https://doi.org/10.1007/BF01307627.
[82] H. Pothier, P. Lafarge, C. Urbina, D. Estève, M.H. Devoret, Single-electron pump based on charging effects, Europhys. Lett. 17 (1992) 249.
[83] H. Pothier, Blocage de Coulomb et transfert d'électrons un par un, Ph.D. thesis, Université Paris-6, 1991.
[84] L. Kouwenhoven, A. Johnson, N. van der Varrt, C. Harmans, Quantized current in a quantum-dot turnstile using oscillating tunnel barriers, Phys. Rev. Lett. 67 (12) (1991).
[85] N. Feltin, F. Piquemal, Determination of the elementary charge and the quantum metrological triangle experiment, Eur. Phys. J. Spec. Top. 172 (2009) 267–296.
[86] H. Grabert, M.H. Devoret, Single Charge Tunneling Coulomb Blockade Phenomena in Nanostructures, NATO ASI Ser., Ser. B: Phys., vol. 294, Plenum Press, 1991.
[87] M.W. Keller, J.M. Martinis, N.M. Zimmerman, A.H. Steinbach, Accuracy of electron counting using a 7-junction electron pump, Appl. Phys. Lett. 69 (12) (1996) 1804–1806.
[88] M.W. Keller, A.L. Eichenberger, J.M. Martinis, N.M. Zimmermann, A capacitance standard based on counting electrons, Science 285 (1999) 1706.
[89] M.W. Keller, N.M. Zimmermann, A.L. Eichenberger, Uncertainty budget for the nist electron counting capacitance standard, eccs-1, Metrologia 44 (2007) 505.
[90] B. Camarota, H. Scherer, M.W. Keller, S.V. Lotkov, G. Willenberg, J. Ahlers, Electron counting capacitance standard with an improved five-junction R-pump, Metrologia 49 (2012) 8–14.
[91] J.P. Pekola, O.P. Saira, V. Maisi, A. Kemppinen, M. Möttönen, Y.A. Pashkin, D. Averin, Single-electron current sources: toward a refined definition of the ampere, Rev. Mod. Phys. 85 (2013) 1421–1472.
[92] B. Kaestner, V. Kashcheyevs, Non-adiabatic quantized charge pumping with tunable-barrier quantum dots: a review of current progress, Rep. Prog. Phys. 78 (2015) 103901.
[93] N.-H. Kaneko, S. Nakamura, Y. Okazaki, A review of the quantum current standard, Meas. Sci. Technol. 27 (2016) 032001.
[94] T.J. Quinn, News from the bipm, Metrologia 26 (1989) 69.
[95] CIPM, Use of the von Klitzing constant to express the value of a reference standard of resistance as a function of the quantum Hall effect, in: Procès-verbaux des séances du Comité international des poids et mesures, 89th Meeting, 2000, p. 101.
[96] T.J. Quinn, News from the BIPM, Metrologia 26 (1989) 69–74.
[97] E. Braun, in: L. Crovini, T.J. Quinn (Eds.), Proceedings of the International School of Physics Enrico Fermi, Course CX, Metrology at the Frontier of Physics and Technology, North-Holland, 1992, p. 211.
[98] BIPM, The BIPM key comparison database (KCDB), Key and supplementary comparisons (Appendix B), Comparison BIPM.EM-K12. https://kcdb.bipm.org.
[99] W. Poirier, F. Schopfer, Resistance metrology based on the quantum Hall effect, Eur. Phys. J. Spec. Top. 172 (2009) 207.
[100] BIPM, On the future revision of the SI, https://www.bipm.org/en/measurement-units/rev-si/.
[101] D.B. Newell, F. Cabiati, J. Fischer, K. Fujii, S.G. Karshenboim, H.S. Margolis, E. de Mirandés, P.J. Mohr, F. Nez, K. Pachucki, T.J. Quinn, B.N. Taylor, M. Wang, B.M. Wood, Z. Zhang, The codata 2017 values of h, e, k, and N_A for the revision of the SI, Metrologia 55 (2018) L13.
[102] P.J. Mohr, B.D. Newell, B.N. Taylor, E. Tiesinga, Data and analysis for the codata 2017 special fundamental constants adjustment, Metrologia 55 (2018) 125.
[103] P.J. Mohr, D.B. Newell, B.N. Taylor, Codata recommended values of the fundamental physical constants: 2014, Rev. Mod. Phys. 88 (2016) 035009.
[104] J. Brun-Picard, S. Djordjevic, D. Leprat, F. Schopfer, W. Poirier, Practical quantum realization of the ampere from the elementary charge, Phys. Rev. X 6 (2016) 041051, https://doi.org/10.1103/PhysRevX.6.041051.
[105] L. Devoille, N. Feltin, B. Steck, B. Chenaud, S. Sassine, S. Djordevic, O. Séron, F. Piquemal, Quantum metrological triangle experiment at LNE: measurements on a three-junction r-pump using a 20000:1 winding ratio cryogenic current comparator, Meas. Sci. Technol. 23 (2012) 124011.
[106] H. Scherer, B. Camarota, Quantum metrology triangle experiments: a status review, Meas. Sci. Technol. 23 (2012) 124010.
[107] S. Sassine, B. Steck, N. Feltin, L. Devoille, B. Chenaud, W. Poirier, F. Schopfer, G. Spengler, O. Séron, F. Piquemal, S. Lotkhov, The quantum metrology triangle experiment: quantization tests of an electron pump, Control. Autom. 21 (2010) 609.
[108] BIPM, Draft for Appendix 2 of the SI Brochure for the "Revised SI", Mise en pratique for the definition of the ampere and other electric units in the SI. https://www.bipm.org/utils/en/pdf/si-mep/MeP-a-2018.pdf.
[109] F. Delahaye, B. Jeckelmann, Revised technical guidelines for reliable dc measurements of the quantized Hall resistance, Metrologia 40 (2003) 217.
[110] T. Endo, M. Koyanagi, A. Nakamura, High-accuracy Josephson potentiometer, IEEE Trans. Instrum. Meas. 32 (1) (1983) 267–271, https://doi.org/10.1109/TIM.1983.4315056.
[111] F.L. Lloyd, C.A. Hamilton, J.A. Beall, D. Go, R.H. Ono, R.E. Harris, A Josephson array voltage standard at 10 V, IEEE Electron Device Lett. 8 (10) (1987) 449–450, https://doi.org/10.1109/EDL.1987.26690.
[112] R. Pöpel, The Josephson effect and voltage standards, Metrologia 29 (2) (1992) 153, http://stacks.iop.org/0026-1394/29/i=2/a=005.
[113] C.A. Hamilton, Josephson voltage standards, Rev. Sci. Instrum. 71 (10) (2000) 3611–3623, https://doi.org/10.1063/1.1289507.
[114] J. Kohlmann, R. Behr, T. Funck, Josephson voltage standards, Meas. Sci. Technol. 14 (8) (2003) 1216, http://stacks.iop.org/0957-0233/14/i=8/a=305.
[115] B. Jeanneret, S.P. Benz, Application of the Josephson effect in electrical metrology, Eur. Phys. J. Spec. Top. 172 (1) (2009) 181–206, https://doi.org/10.1140/epjst/e2009-01050-6.
[116] R. Behr, O. Kieler, J. Kohlmann, F. Müller, L. Palafox, Development and metrological applications of Josephson arrays at ptb, Meas. Sci. Technol. 23 (2012) 124002.
[117] M.T. Levinsen, R.Y. Chiao, M.J. Feldman, B.A. Tucker, An inverse ac Josephson effect voltage standard, Appl. Phys. Lett. 31 (11) (1977) 776–778, https://doi.org/10.1063/1.89520.
[118] M. Gurvitch, M. Washington, H. Huggins, J. Rowell, Preparation and properties of nb Josephson junctions with thin Al layers, IEEE Trans. Magn. 19 (3) (1983) 791–794, https://doi.org/10.1109/TMAG.1983.1062296.
[119] C.A. Hamilton, F.L. Lloyd, K. Chieh, W.C. Goeke, A 10-V Josephson voltage standard, IEEE Trans. Instrum. Meas. 38 (2) (1989) 314–316, https://doi.org/10.1109/19.192296.
[120] F. Müller, R. Pöpel, J. Kohlmann, J. Niemeyer, W. Meier, T. Weimann, L. Grimm, F.-W. Dunschede, P. Gutmann, Optimized 1 V and 10 V Josephson series arrays, IEEE Trans. Instrum. Meas. 46 (2) (1997) 229–232, https://doi.org/10.1109/19.571819.
[121] BIPM, The BIPM key comparison database (KCDB), Key and supplementary comparisons (Appendix B), Comparison BIPM.EM-K10.b. https://kcdb.bipm.org.
[122] B.M. Wood, S. Solve, A review of Josephson comparison results, Metrologia 46 (6) (2009) R13, http://stacks.iop.org/0026-1394/46/i=6/a=R01.
[123] S. Solve, R. Chayramy, S. Djorjevic, O. Séron, Comparison of the Josephson voltage standards of the LNE and the BIPM (part of the ongoing BIPM key comparison bipm.em-k10.b), Metrologia 46 (1A) (2009) 01002, http://stacks.iop.org/0026-1394/46/i=1A/a=01002.

[124] Hypres, https://www.hypres.com/hypres-primary-voltage-standard/.
[125] Supracon, http://www.supracon.com/en/standards.html.
[126] C.A. Hamilton, C.J. Burroughs, R.L. Kautz, Josephson d/a converter with fundamental accuracy, IEEE Trans. Instrum. Meas. 44 (2) (1995) 223–225, https://doi.org/10.1109/19.377816.
[127] S.P. Benz, C.A. Hamilton, C.J. Burroughs, T.E. Harvey, L.A. Christian, Stable 1 Volt programmable voltage standard, Appl. Phys. Lett. 71 (13) (1997) 1866–1868, https://doi.org/10.1063/1.120189.
[128] H. Yamamori, M. Ishizaki, A. Shoji, P.D. Dresselhaus, S.P. Benz, 10 V programmable Josephson voltage standard circuits using NbN/TiN_x/NbN/TiN_x/NbN double-junction stacks, Appl. Phys. Lett. 88 (4) (2006) 042503, https://doi.org/10.1063/1.2167789.
[129] F. Müller, R. Behr, T. Weimann, L. Palafox, D. Olaya, P.D. Dresselhaus, S.P. Benz, 1 V and 10 V SNS programmable voltage standards for 70 GHz, IEEE Trans. Appl. Supercond. 19 (3) (2009) 981–986, https://doi.org/10.1109/TASC.2009.2017911.
[130] C.J. Burroughs, P.D. Dresselhaus, A. Rüfenacht, D. Olaya, M.M. Elsbury, Y. Tang, S.P. Benz, Nist 10 V programmable Josephson voltage standard system, IEEE Trans. Instrum. Meas. 60 (7) (2011) 2482–2488, https://doi.org/10.1109/TIM.2010.2101191.
[131] B. Baek, P.D. Dresselhaus, S.P. Benz, Co-sputtered amorphous Nb_xSi_{1-x} barriers for Josephson-junction circuits, IEEE Trans. Appl. Supercond. 16 (4) (2006) 1966–1970, https://doi.org/10.1109/TASC.2006.881816.
[132] P.D. Dresselhaus, M.M. Elsbury, D. Olaya, C.J. Burroughs, S.P. Benz, 10 volt programmable Josephson voltage standard circuits using NbSi-barrier junctions, IEEE Trans. Appl. Supercond. 21 (3) (2011) 693–696, https://doi.org/10.1109/TASC.2010.2079310.
[133] F. Müller, T. Scheller, R. Wendisch, R. Behr, O. Kieler, L. Palafox, J. Kohlmann, Nbsi barrier junctions tuned for metrological applications up to 70 GHz: 20 V arrays for programmable Josephson voltage standards, IEEE Trans. Appl. Supercond. 23 (3) (2013) 1101005, https://doi.org/10.1109/TASC.2012.2235895.
[134] H. Yamamori, T. Yamada, H. Sasaki, A. Shoji, A 10 V programmable Josephson voltage standard circuit with a maximum output voltage of 20 V, Supercond. Sci. Technol. 21 (10) (2008) 105007, http://stacks.iop.org/0953-2048/21/i=10/a=105007.
[135] H. Yamamori, T. Yamada, H. Sasaki, A. Shoji, Improved fabrication yield for 10-V programmable Josephson voltage standard circuit including 524 288 NbN/TiN/NbN Josephson junctions, IEEE Trans. Appl. Supercond. 20 (2) (2010) 71–75, https://doi.org/10.1109/TASC.2010.2041349.
[136] S. Djordjevic, O. Séron, S. Solve, R. Chayramy, Direct comparison between a programmable and a conventional Josephson voltage standard at the level of 10 V, Metrologia 45 (4) (2008) 429, http://stacks.iop.org/0026-1394/45/i=4/a=008.
[137] Y. Tang, V.N. Ojha, S. Schlamminger, A. Rüfenacht, C.J. Burroughs, P.D. Dresselhaus, S.P. Benz, A 10 V programmable Josephson voltage standard and its applications for voltage metrology, Metrologia 49 (6) (2012) 635, http://stacks.iop.org/0026-1394/49/i=6/a=635.
[138] A. Rüfenacht, Y. hua Tang, S. Solve, A.E. Fox, P.D. Dresselhaus, C.J. Burroughs, R.E. Schwall, R. Chayramy, S.P. Benz, Automated direct comparison of two cryocooled 10 Volt programmable Josephson voltage standards, Metrologia 55 (4) (2018) 585, http://stacks.iop.org/0026-1394/55/i=4/a=585.
[139] H.E. van den Brom, E. Houtzager, G. Rietveld, R. van Bemmelen, O. Chevtchenko, Voltage linearity measurements using a binary Josephson system, Meas. Sci. Technol. 18 (11) (2007) 3316, http://stacks.iop.org/0957-0233/18/i=11/a=008.
[140] S. Chen, Y. Amagai, M. Maruyama, N. Kaneko, Uncertainty evaluation of a 10 V rms sampling measurement system using the ac programmable Josephson voltage standard, IEEE Trans. Instrum. Meas. 64 (12) (2015) 3308–3314, https://doi.org/10.1109/TIM.2015.2450355.
[141] C.J. Burroughs Jr., A. Rüfenacht, S.P. Benz, P.D. Dresselhaus, Systematic error analysis of stepwise-approximated ac waveforms generated by programmable Josephson voltage standards, IEEE Trans. Instrum. Meas. 58 (4) (2009) 761–767, https://doi.org/10.1109/TIM.2008.2007041.
[142] O. Seron, S. Djordjevic, I. Budovsky, T. Hagen, R. Behr, L. Palafox, Precision ac–dc transfer measurements with a Josephson waveform synthesizer and a buffer amplifier, IEEE Trans. Instrum. Meas. 61 (1) (2012) 198–204, https://doi.org/10.1109/TIM.2011.2157429.
[143] I. Budovsky, R. Behr, L. Palafox, S. Djordjevic, T. Hagen, Technique for the calibration of thermal voltage converters using a Josephson waveform synthesizer and a transconductance amplifier, Meas. Sci. Technol. 23 (12) (2012) 124005, http://stacks.iop.org/0957-0233/23/i=12/a=124005.
[144] A. Rüfenacht, N.E. Flowers-Jacobs, S.P. Benz, Impact of the latest generation of Josephson voltage standards in ac and dc electric metrology, Metrologia 55 (5) (2018) S152, http://stacks.iop.org/0026-1394/55/i=5/a=S152.
[145] R. Behr, L. Palafox, G. Ramm, H. Moser, J. Melcher, Direct comparison of Josephson waveforms using an ac quantum voltmeter, IEEE Trans. Instrum. Meas. 56 (2) (2007) 235–238, https://doi.org/10.1109/TIM.2007.891076.
[146] A. Rüfenacht, C.J. Burroughs, S.P. Benz, Precision sampling measurements using ac programmable Josephson voltage standards, Rev. Sci. Instrum. 79 (4) (2008) 044704, https://doi.org/10.1063/1.2901683.
[147] B. Jeanneret, F. Overney, A. Rüfenacht, The Josephson locked synthesizer, Meas. Sci. Technol. 23 (12) (2012) 124004, http://stacks.iop.org/0957-0233/23/i=12/a=124004.
[148] L. Palafox, G. Ramm, R. Behr, W.G.K. Ihlenfeld, H. Moser, Primary ac power standard based on programmable Josephson junction arrays, IEEE Trans. Instrum. Meas. 56 (2) (2007) 534–537, https://doi.org/10.1109/TIM.2007.891092.
[149] J. Lee, R. Behr, L. Palafox, A. Katkov, M. Schubert, M. Starkloff, A.C. Böck, An ac quantum voltmeter based on a 10 V programmable Josephson array, Metrologia 50 (6) (2013) 612, http://stacks.iop.org/0026-1394/50/i=6/a=612.
[150] W.G.K. Ihlenfeld, R.P. Landim, An automated Josephson-based ac-voltage calibration system, IEEE Trans. Instrum. Meas. 64 (6) (2015) 1779–1784, https://doi.org/10.1109/TIM.2014.2383092.
[151] Y. Amagai, M. Maruyama, T. Shimazaki, H. Yamamori, H. Fujiki, N. Kaneko, Characterization of high-stability ac source using ac-programmable Josephson voltage standard system, in: 2016 Conference on Precision Electromagnetic Measurements (CPEM 2016), Ottawa, July 10–15, 2016, pp. 1–2.
[152] T. Yamada, C. Urano, H. Nishinaka, Y. Murayama, A. Iwasa, H. Yamamori, H. Sasaki, A. Shoji, Y. Nakamura, Single-chip 10-V programmable Josephson voltage standard system based on a refrigerator and its precision evaluation, IEEE Trans. Appl. Supercond. 20 (1) (2010) 21–25, https://doi.org/10.1109/TASC.2009.2033939.
[153] A. Rüfenacht, L.A. Howe, A.E. Fox, R.E. Schwall, P.D. Dresselhaus, C.J. Burroughs, S.P. Benz, Cryocooled 10 V programmable Josephson voltage standard, IEEE Trans. Instrum. Meas. 64 (6) (2015) 1477–1482, https://doi.org/10.1109/TIM.2014.2374697.
[154] M. Schubert, M. Starkloff, K. Peiselt, S. Anders, R. Knipper, J. Lee, R. Behr, L. Palafox, A.C. Böck, L. Schaidhammer, P.M. Fleischmann, H.-G. Meyer, A dry-cooled ac quantum voltmeter, Supercond. Sci. Technol. 29 (10) (2016) 105014, http://stacks.iop.org/0953-2048/29/i=10/a=105014.
[155] J. Lee, J. Schurr, J. Nissila, L. Palafox, R. Behr, The Josephson two-terminal-pair impedance bridge, Metrologia 47 (2010) 453.
[156] S.P. Benz, C.A. Hamilton, A pulse-driven programmable Josephson voltage standard, Appl. Phys. Lett. 68 (22) (1996) 3171–3173, https://doi.org/10.1063/1.115814.
[157] S.P. Benz, C.A. Hamilton, C.J. Burroughs, T.E. Harvey, L.A. Christian, J.X. Przybysz, Pulse-driven Josephson digital/analog converter voltage standard, IEEE Trans. Appl. Supercond. 8 (2) (1998) 42–47, https://doi.org/10.1109/77.678440.
[158] N.E. Flowers-Jacobs, A.E. Fox, P.D. Dresselhaus, R.E. Schwall, S.P. Benz, Two-volt Josephson arbitrary waveform synthesizer using Wilkinson dividers, IEEE Trans. Appl. Supercond. 26 (6) (2016) 1–7, https://doi.org/10.1109/TASC.2016.2532798.
[159] O.F. Kieler, R. Behr, R. Wendisch, S. Bauer, L. Palafox, J. Kohlmann, Towards a 1 V Josephson arbitrary waveform synthesizer, IEEE Trans. Appl. Supercond. 25 (3) (2015) 1–5, https://doi.org/10.1109/TASC.2014.2366916.
[160] S. Pavan, R. Schreier, G. Temes, Understanding Delta–Sigma Data Converters, Wiley, New York, 1987.
[161] P.S. Filipski, H.E. van den Brom, E. Houtzager, International comparison of quantum ac voltage standards for frequencies up to 100 kHz, Measurement 45 (9) (2012) 2218–2225, https://doi.org/10.1016/j.measurement.2012.03.008, http://www.sciencedirect.com/science/article/pii/S0263224112001170.

[162] H.E. van den Brom, E. Houtzager, Voltage lead corrections for a pulse-driven ac Josephson voltage standard, Meas. Sci. Technol. 23 (12) (2012) 124007, http://stacks.iop.org/0957-0233/23/i=12/a=124007.
[163] T. Hagen, I. Budovsky, S.P. Benz, C.J. Burroughs, Calibration system for ac measurement standards using a pulse-driven Josephson voltage standard and an inductive voltage divider, in: 2012 Conference on Precision Electromagnetic Measurements, Wahington, DC, USA, July 1–6, 2012, pp. 672–673.
[164] A. Sosso, P. Durandetto, B. Trinchera, O. Kieler, R. Behr, J. Kohlmann, Characterization of a Josephson array for pulse-driven voltage standard in a cryocooler, Measurement 95 (2017) 77–81, https://doi.org/10.1016/j.measurement.2016.09.039, http://www.sciencedirect.com/science/article/pii/S0263224116305425.
[165] J. Kohlmann, O. Kieler, T. Scheller, B. Egeling, R. Wendisch, R. Behr, Series arrays of nbsi barrier Josephson junctions for ac voltage standards, in: 2016 Conference on Precision Electromagnetic Measurements (CPEM 2016), Ottawa, July 10–15, 2016, pp. 1–2.
[166] N.E. Flowers-Jacobs, S.B. Waltman, A.E. Fox, P.D. Dresselhaus, S.P. Benz, Josephson arbitrary waveform synthesizer with two layers of Wilkinson dividers and an FIR filter, IEEE Trans. Appl. Supercond. 26 (6) (2016) 1–7, https://doi.org/10.1109/TASC.2016.2582800.
[167] R. Behr, O. Kieler, J. Lee, S. Bauer, L. Palafox, J. Kohlmann, Direct comparison of a 1-V Josephson arbitrary waveform synthesizer and an ac quantum voltmeter, Metrologia 52 (4) (2015) 528, http://stacks.iop.org/0026-1394/52/i=4/a=528.
[168] S.P. Benz, S.B. Waltman, A.E. Fox, P.D. Dresselhaus, A. Rüfenacht, J.M. Underwood, L.A. Howe, R.E. Schwall, C.J. Burroughs, One-volt Josephson arbitrary waveform synthesizer, IEEE Trans. Appl. Supercond. 25 (2015) 1300108.
[169] P.D. Dresselhaus, M.M. Elsbury, S.P. Benz, Tapered transmission lines with dissipative junctions, IEEE Trans. Appl. Supercond. 19 (3) (2009) 993–998, https://doi.org/10.1109/TASC.2009.2019245.
[170] S.P. Benz, S.B. Waltman, Pulse-bias electronics and techniques for a Josephson arbitrary waveform synthesizer, IEEE Trans. Appl. Supercond. 24 (6) (2014) 1–7, https://doi.org/10.1109/TASC.2014.2338326.
[171] K. Zhou, J. Qu, S.P. Benz, Zero-compensation method and reduced inductive voltage error for the ac Josephson voltage standard, IEEE Trans. Appl. Supercond. 25 (5) (2015) 1–6, https://doi.org/10.1109/TASC.2015.2470684.
[172] J.A. Brevik, N.E. Flowers-Jacobs, A.E. Fox, E.B. Golden, P.D. Dresselhaus, S.P. Benz, Josephson arbitrary waveform synthesis with multilevel pulse biasing, IEEE Trans. Appl. Supercond. 27 (3) (2017) 1–7, https://doi.org/10.1109/TASC.2017.2662708.
[173] N.E. Flowers-Jacobs, S.B.W.A. Rüfenacht, A.E. Fox, J.A. Brevik, P.D. Dresselhaus, S.P. Benz, Three volt pulse-driven Josephson arbitrary waveform synthesizer, in: 2018 Conference on Precision Electromagnetic Measurements (CPEM 2018), Paris, July 8–13, 2018, pp. 1–2.
[174] B. Karlsen, K. Lind, H. Malmbekk, P. Ohlckers, Development of high precision voltage dividers and buffer for ac voltage metrology up to 1 mHz, in: 2016 Conference on Precision Electromagnetic Measurements (CPEM 2016), Ottawa, July 10–15, 2016, pp. 1–2.
[175] I. Budovsky, L. Palafox, 10 V transconductance amplifier for the comparison of Josephson standards and thermal converters, in: 2016 Conference on Precision Electromagnetic Measurements (CPEM 2016), Ottawa, July 10–15, 2016, pp. 1–2.
[176] L. Palafox, R. Behr, O. Kieler, J. Lee, I. Budovsky, S. Bauer, T. Hagen, First metrological applications of the ptb 1 V Josephson arbitrary waveform synthesizer, in: 2016 Conference on Precision Electromagnetic Measurements (CPEM 2016), Ottawa, July 10–15, 2016, pp. 1–2.
[177] H.E. van den Brom, D. Zhao, E. Houtzager, Voltage lead errors in an ac Josephson voltage standard: explanation in terms of standing waves, in: 2016 Conference on Precision Electromagnetic Measurements (CPEM 2016), Ottawa, July 10–15, 2016, pp. 1–2.
[178] R.C. Toonen, S.P. Benz, Nonlinear behavior of electronic components characterized with precision multitones from a Josephson arbitrary waveform synthesizer, IEEE Trans. Appl. Supercond. 19 (3) (2009) 715–718, https://doi.org/10.1109/TASC.2009.2019051.
[179] R. Behr, O. Kieler, B. Schumacher, A precision microvolt-synthesizer based on a pulse-driven Josephson voltage standard, IEEE Trans. Instrum. Meas. 66 (6) (2017) 1385–1390, https://doi.org/10.1109/TIM.2016.2619998.
[180] W. Poirier, F. Schopfer, J. Guignard, O. Thevenot, P. Gournay, Application of the quantum Hall effect to resistance metrology, C. R. Phys. 5 (2011) 171.
[181] I.K. Harvey, A precise low temperature dc ratio transformer, Rev. Sci. Instrum. 43 (11) (1972) 1626–1629.
[182] F. Lafont, R. Ribeiro-Palau, D. Kazazis, A. Michon, O. Couturaud, C. Consejo, T. Chassagne, M. Zielinski, M. Portail, B. Jouault, F. Schopfer, W. Poirier, Quantum Hall resistance standards from graphene grown by chemical vapour deposition on silicon carbide, Nat. Commun. 6 (2015) 6806.
[183] D. Drung, M. Götz, E. Pesel, J.-H. Storm, C. Assmann, M. Peters, T. Schurig, Improving the stability of cryogenic current comparator setups, Supercond. Sci. Technol. 22 (2009) 114004.
[184] C.A. Sanchez, B.M. Wood, A.D. Inglis, Ccc bridge with digitally controlled current sources, IEEE Trans. Instrum. Meas. 58 (2009) 1202.
[185] J.M. Williams, T.J.B.M. Janssen, G. Rietveld, E. Houtzager, An automated cryogenic current comparator resistance ratio bridge for routine resistance measurements, Metrologia 47 (2010) 167.
[186] W. Poirier, D. Leprat, F. Schopfer, Towards 10^{-10}-accurate resistance bridge at LNE, in: D. Allal, S. Djordjevic (Eds.), 2018 Conference on Precision Electromagnetic Measurements (CPEM 2018), Paris, July 8–13, 2018.
[187] F. Delahaye, Series and parallel connection of multiterminal quantum Hall-effect devices, J. Appl. Phys. 73 (1993) 7914.
[188] F. Piquemal, J. Blanchet, G. Geneves, J.-P. André, A first attempt to realize multiple-qhe devices series array resistance standards, IEEE Trans. Instrum. Meas. 48 (1999) 296.
[189] W. Poirier, A. Bounouh, K. Hayashi, F. Piquemal, G. Genevès, J.-P. André, Rk/100 and rk/200 quantum Hall array resistance standards, J. Appl. Phys. 92 (2002) 2844.
[190] A. Bounouh, W. Poirier, F. Piquemal, G. Genevès, J.-P. André, Quantum resistance standards with double 2DEG, IEEE Trans. Instrum. Meas. 52 (2003) 555.
[191] W. Poirier, A. Bounouh, F. Piquemal, J.-P. André, A new generation of qhars: discussion about the technical criteria for quantization, Metrologia 41 (2004) 285.
[192] J. Konemann, F.-J. Ahlers, E. Pesel, K. Pierz, H.W. Schumacher, Magnetic field reversible serial quantum Hall arrays, IEEE Trans. Instrum. Meas. 60 (2011) 2512.
[193] T. Oe, S. Gorwadkar, T. Itatani, N.-H. Kaneko, Development of 1 MΩ quantum Hall array resistance standards, IEEE Trans. Instrum. Meas. 66 (2016) 1475.
[194] J. Konemann, C. Leicht, F.-J. Ahlers, E. Pesel, K. Pierz, H.W. Schumacher, Investigation of serial quantum Hall arrays as a quantum resistance standard, J. Phys. Conf. Ser. 334 (2011) 012017.
[195] T. Oe, K. Matsuhiro, T. Itatani, S. Gorwadkar, S. Kiryu, N. Kaneko, New design of quantized Hall resistance array device, IEEE Trans. Instrum. Meas. 62 (2013) 1755.
[196] A. Domae, T. Oe, S. Kiryu, N.-H. Kaneko, Experimental demonstration of current dependence evaluation of voltage divider based on quantized Hall resistance voltage divider, IEEE Trans. Instrum. Meas. 99 (2017) 1.
[197] F. Schopfer, W. Poirier, Quantum resistance standard accuracy close to the zero-dissipation state, J. Appl. Phys. 114 (2013) 064508.
[198] K.S. Novoselov, A.K. Geim, S.V. Morozov, D. Jiang, Y. Zhang, S.V. Dubonos, I.V. Grigorieva, A.A. Firsov, Electric field effect in atomically thin carbon films, Science 306 (2004) 666.
[199] A.K. Geim, K.S. Novoselov, The rise of graphene, Nat. Mater. 6 (2007) 183.
[200] A.C. Ferrari, et al., Science and technology roadmap for graphene, related two-dimensional crystals, and hybrid systems, Nanoscale 7 (2015) 4598.
[201] P.R. Wallace, The band theory of graphite, Phys. Rev. 71 (1947) 622.
[202] A.H. CastroNeto, F. Guinea, N.M.R. Peres, K.S. Novoselov, A.K. Geim, The electronic properties of graphene, Rev. Mod. Phys. 81 (2009) 109.

[203] S.D. Sarma, S. Adam, E.H. Hwang, E. Rossi, Electronic transport in two-dimensional graphene, Rev. Mod. Phys. 83 (2011) 407.
[204] K.S. Novoselov, A.K. Geim, S.V. Morozov, D. Jiang, M.I. Katsnelson, S.V.D.I.V. Grigorieva, A.A. Firsov, Two-dimensional gas of massless Dirac fermions in graphene, Nature 438 (2005) 197.
[205] Y.B. Zhang, Y.W. Tan, H. Stormer, P. Kim, Experimental observation of the quantum Hall effect and Berry's phase in graphene, Nature 438 (2005) 201.
[206] M.O. Goerbig, Electronic properties of graphene in a strong magnetic field, Rev. Mod. Phys. 83 (2011) 1193.
[207] E. Pallecchi, F. Lafont, V. Cavaliere, F. Schopfer, D. Mailly, W. Poirier, A. Ouerghi, High Electron Mobility in Epitaxial Graphene on 4H-SiC(0001) via post-growth annealing under hydrogen, Sci. Rep. 4 (2014) 4558.
[208] Y. Zhang, Z. Jiang, J.P. Small, M.S. Purewal, Y.-W. Tan, M. Fazlollahi, J.D. Chudow, J.A. Jaszczak, H.L. Stormer, P. Kim, Landau-level splitting in graphene in high magnetic fields, Phys. Rev. Lett. 96 (2006) 136806.
[209] K.I. Bolotin, F. Ghahari, M.D. Shulman, H.L. Stormer, P. Kim, Observation of the fractional quantum Hall effect in graphene, Nature 462 (2009) 196.
[210] X. Du, I. Skachko, F. Duerr, A. Luican, E.Y. Andrei, Fractional quantum Hall effect and insulating phase of Dirac electrons in graphene, Nature 462 (2009) 192.
[211] K. Nomura, A.H. MacDonald, Quantum Hall ferromagnetism in graphene, Phys. Rev. Lett. 96 (2006) 256602.
[212] M. Kharitonov, Phase diagram for the $\nu = 0$ quantum Hall state in monolayer graphene, Phys. Rev. B 85 (2012) 155439.
[213] D.A. Abanin, K.S. Novoselov, U. Zeitler, P.A. Lee, A.K. Geim, L.S. Levitov, Dissipative quantum Hall effect in graphene near the Dirac point, Phys. Rev. Lett. 98 (2007) 196806.
[214] A.F. Young, C.R. Dean, L. Wang, H. Ren, P. Cadden-Zimansky, K. Watanabe, T. Taniguchi, J. Hone, K.L. Shepard, P. Kim, Spin and valley quantum Hall ferromagnetism in graphene, Nat. Phys. 8 (2012) 550.
[215] K.S. Novoselov, Z. Jiang, Y. Zhang, S.V. Morozov, H.L. Stormer, U. Zeitler, J.-C. Maan, G.S. Boebinger, P. Kim, A.K. Geim, Room-temperature quantum Hall effect in graphene, Science 315 (2007) 1379.
[216] W. Poirier, F. Schopfer, Can graphene set new standards?, Nat. Nanotechnol. 5 (2010) 171.
[217] F. Schopfer, W. Poirier, Graphene-based quantum Hall effect metrology, Mater. Res. Soc. Bull. 37 (2012) 1255.
[218] T.J.B.M. Janssen, A. Tzalenchuk, S. Lara-Avila, S. Kubatkin, V.I. Falko, Quantum resistance metrology using graphene, Rep. Prog. Phys. 76 (2013) 104501.
[219] A.J.M. Giesbers, G. Rietveld, E. Houtzager, U. Zeitler, R. Yang, K.S. Novoselov, A.K. Geim, J.-C. Maan, Quantum resistance metrology in graphene, Appl. Phys. Lett. 93 (2009) 222109.
[220] J. Guignard, D. Leprat, D.C. Glattli, F. Schopfer, W. Poirier, Quantum Hall effect in exfoliated graphene affected by charged impurities: metrological measurements, Phys. Rev. B 85 (2012) 165420.
[221] M. Woszczyna, M. Friedemann, M. Götz, E. Pesel, K. Pierz, T. Weimann, F.J. Ahlers, Precision quantization of Hall resistance in transferred graphene, Appl. Phys. Lett. 100 (2012) 164106.
[222] A. Tzalenchuk, S. Lara-Avila, A. Kalaboukhov, S. Paolillo, M.S. Syvajarvi, R. Yakimova, O. Kazakova, T.J.B.M. Janssen, V. Falko, S. Kubatkin, Towards a quantum resistance standard based on epitaxial graphene, Nat. Nanotechnol. 5 (2010) 186.
[223] T.J.B.M. Janssen, J.M. Williams, N.E. Fletcher, R. Goebel, A. Tzalenchuk, R. Yakimova, S. Lara-Avila, S. Kubatkin, V.I. Falko, Precision comparison of the quantum Hall effect in graphene and gallium arsenide, Metrologia 49 (2012) 294.
[224] F. Lafont, Quantum Hall Effect in Graphene for Resistance Metrology: Disorder and Quantization, PhD thesis, Université Paris Sud-Paris XI, 2015. https://hal.archives-ouvertes.fr/tel-01176183.
[225] C. Riedl, C. Coletti, U. Starke, Structural and electronic properties of epitaxial graphene on SiC(0001): a review of growth, characterization, transfer doping and hydrogen intercalation, J. Phys. D, Appl. Phys. 43 (2010) 374009.
[226] J.A. Alexander-Webber, J. Huang, D.K. Maude, T. Janssen, A. Tzalenchuk, V. Antonov, T. Yager, S. Lara-Avila, S. Kubatkin, R. Yakimova, R.J. Nicholas, Giant quantum Hall plateaus generated by charge transfer in epitaxial graphene, Sci. Rep. 6 (2016) 30296.
[227] T.J.B.M. Janssen, A. Tzalenchuk, R. Yakimova, S. Kubatkin, S. Lara-Avila, S. Kopylov, V.I. Falko, Anomalously strong pinning of the filling factor $\nu = 2$ in epitaxial graphene, Phys. Rev. B 83 (2011) 233402.
[228] F. Lafont, R. Ribeiro, Z. Han, S. Roche, V. Bouchiat, F. Schopfer, W. Poirier, Anomalous dissipation mechanism and Hall quantization limit in polycrystalline graphene grown by chemical vapor deposition, Phys. Rev. B 90 (2014) 115422.
[229] B. Jabakhanji, A. Michon, C. Consejo, W. Desrat, M. Portail, A. Tiberj, M. Paillet, A. Zahab, F. Cheynis, F. Lafont, F. Schopfer, W. Poirier, F. Bertran, P. Le Fèvre, A. Taleb-Ibrahimi, D. Kazazis, W. Escoffier, B.C. Camargo, Y. Kopelevich, J. Camassel, B. Jouault, Phys. Rev. B 89 (2014) 085422.
[230] A. Michon, S. Vézian, A. Ouerghi, M. Zielinski, T. Chassagne, M. Portail, Direct growth of few-layer graphene on 6H-SiC and 3C-SiC/Si via propane chemical vapor deposition, Appl. Phys. Lett. 97 (2010) 171909.
[231] J. Brun-Picard, R. Dagher, D. Mailly, A. Nachawaty, B. Jouault, A. Michon, W. Poirier, F. Schopfer, Quantum Hall resistance standard in graphene grown by CVD on SiC: state-of-the-art of the experimental mastery, in: D. Allal, S. Djordjevic (Eds.), 2018 Conference on Precision Electromagnetic Measurements (CPEM 2018), Paris, July 8–13, 2018.
[232] M. Kruskopf, D.M. Pakdehi, K. Pierz, S. Wundrack, R. Stosch, T. Dziomba, M. Götz, J. Baringhaus, J. Aprojanz, C. Tegenkamp, J. Lidzba, T. Seyller, F. Hohls, F.-J. Ahlers, H.W. Schumacher, Comeback of epitaxial graphene for electronics: large-area growth of bilayer-free graphene on SiC, 2D Mater. 3 (2016) 041002.
[233] Y. Yang, G. Cheng, P. Mende, I.G. Calizo, R.M. Feenstra, C. Chuang, C.-W. Liu, C.-I. Liu, G.R. Jones, A.R.H. Walker, R.E. Elmquist, Epitaxial graphene homogeneity and quantum Hall effect in millimeter-scale devices, Carbon 115 (2017) 229.
[234] H. He, K.H. Kim, A. Danilov, D. Montemurro, L. Yu, Y.W. Park, F. Lombardi, T. Bauch, K. Moth-Poulsen, T. Iakimov, R. Yakimova, P. Malmberg, C. Muller, S. Kubatkin, S. Lara-Avila, Uniform doping of graphene close to the charge neutrality point by polymer-assisted spontaneous assembly of molecular dopants, arXiv:1805.05644.
[235] C.-C. Kalmbach, J. Schurr, F.J. Ahlers, A. Muller, S. Novikov, N. Lebedeva, A. Satrapinski, Towards a graphene-based quantum impedance standard, Appl. Phys. Lett. 105 (2014) 073511.
[236] M. Woszczyna, M. Friedemann, T. Dziomba, T. Weimann, F.J. Ahlers, Graphene p–n junction arrays as quantum-Hall resistance standards, Appl. Phys. Lett. 99 (2011) 022112.
[237] J.P. Pekola, J.J. Vartiainen, M. Mottonen, O.P. Saira, M. Meschke, D.V. Averin, Hybrid single-electron transistor as a source of quantized electric current, Nat. Phys. 4 (2008) 120.
[238] L.J. Geerligs, V.F. Anderegg, P.A.M. Holweg, J.E. Mooij, H. Pothier, D. Esteve, C. Urbina, M.H. Devoret, Frequency-locked turnstile device for single electrons, Phys. Rev. Lett. 64 (1990) 2691.
[239] V.F. Maisi, Y.A. Pashkin, S. Kafanov, J.-S. Tsai, J.P. Pekola, Parallel pumping of electrons, New J. Phys. 11 (2009) 113057.
[240] A. Fujiwara, Y. Takahashi, Manipulation of elementary charge in silicon charge-coupled device, Nature 410 (2001) 560.
[241] A. Fujiwara, N. Zimmerman, Y. Ono, Y. Takahashi, Current quantization due to a single-electron transfer in Si-wire charge-coupled devices, Appl. Phys. Lett. 84 (8) (2003).
[242] A. Fujiwara, K. Nishiguchi, Y. Ono, Nanoampere charge pump by single-electron ratchet using silicon nanowire metal-oxide-semiconductor field-effect transistor, Appl. Phys. Lett. 92 (4) (2008) 042102, https://doi.org/10.1063/1.2837544.
[243] Y. Ono, Y. Takahashi, Electron pump by a combined single-electron field-effect transistor structure, Appl. Phys. Lett. 82 (2003) 1221.
[244] M. Blumenthal, B. Kaestner, L. Li, S. Giblin, T. Janssen, M. Pepper, D. Anderson, G. Jones, D. Ritchie, Gigahertz quantized charge pumping, Nat. Phys. 3 (2007) 343–347.

[245] B. Kaestner, V. Kashcheyevs, S. Amakawa, M.D. Blumenthal, L. Li, T.J.B.M. Janssen, G. Hein, K. Pierz, T. Weimann, U. Siegner, H.W. Schumacher, Single-parameter nonadiabatic quantized charge pumping, Phys. Rev. B 77 (2008) 153301.
[246] B. Kaestner, C. Leicht, V. Kashcheyevs, K. Pierz, U. Siegner, H.W. Schumacher, Single-parameter quantized charge pumping in high magnetic fields, Appl. Phys. Lett. 94 (1) (2009) 012106, https://doi.org/10.1063/1.3063128.
[247] S.P. Giblin, S.J. Wright, J.D. Fletcher, M. Kataoka, M. Pepper, T.J.B.M. Janssen, D.A. Ritchie, C.A. Nicoll, D. Anderson, G.A.C. Jones, An accurate high-speed single-electron quantum dot pump, New J. Phys. (2010) 073013.
[248] X. Jehl, B. Roche, M. Sanquer, R. Wacquez, M. Vinet, T. Charron, S. Djordjevic, L. Devoille, Multi-charge pumping at 1 GHz with a hybrid metal/semiconductor device, in: Conference on Precision Electromagnetic Measurements, Washington, DC, July 1–6, 2012, pp. 250–251.
[249] X. Jehl, B. Voisin, T. Charron, P. Clapera, S. Ray, B. Roche, M. Sanquer, S. Djordjevic, L. Devoille, R. Wacquez, M. Vinet, Hybrid metal-semiconductor electron pump for quantum metrology, Phys. Rev. X 3 (2013) 021012.
[250] F. Stein, D. Drung, L. Fricke, H. Scherer, F. Hohls, C. Leicht, M. Götz, C. Krause, R. Behr, E. Pesel, K. Pierz, U. Siegner, F.J. Ahlers, H.W. Schumacher, Validation of a quantized-current source with 0.2 ppm uncertainty, Appl. Phys. Lett. 107 (2015) 103501.
[251] F. Stein, H. Scherer, T. Gerster, R. Behr, M. Götz, E. Pesel, C. Leicht, N. Ubbelohde, T. Weimann, K. Pierz, H.W. Schumacher, F. Hohls, Robustness of single-electron pumps at sub-ppm current accuracy level, Metrologia 54 (2017) S1.
[252] G. Yamahata, S.P. Giblin, M. Kataoka, T. Karasawa, A. Fujiwara, Gigahertz single-electron pumping in silicon with an accuracy better than 9.2 parts in 10^7, Appl. Phys. Lett. 109 (2016) 013101.
[253] R. Zhao, A. Rossi, S.P. Giblin, J.D. Fletcher, F.E. Hudson, M. Möttönen, M. Kataoka, A.S. Dzurak, Thermal-error regime in high-accuracy gigahertz single-electron pumping, Phys. Rev. Appl. 8 (2017) 044021.
[254] S.P. Giblin, M. Kataoka, J.D. Fletcher, P. See, T.J.B.M. Janssen, J.P. Griffiths, G.A.C. Jones, I. Farrer, D.A. Ritchie, Towards a quantum representation of the ampere using single electron pumps, Nat. Commun. 3 (2012) 930, https://doi.org/10.1038/ncomms1935.
[255] V. Kashcheyevs, B. Kaestner, Universal decay cascade model for dynamic quantum dot initialization, Phys. Rev. Lett. 104 (2010) 186805, https://doi.org/10.1103/PhysRevLett.104.186805.
[256] J.D. Fletcher, M. Kataoka, S.P. Giblin, S. Park, H.-S. Sim, P. See, D.A. Ritchie, J.P. Griffiths, G.A.C. Jones, H.E. Beere, T.J.B.M. Janssen, Stabilization of single-electron pumps by high magnetic fields, Phys. Rev. B 86 (2012) 155311, https://doi.org/10.1103/PhysRevB.86.155311.
[257] L. Fricke, M. Wulf, B. Kaestner, V. Kashcheyevs, J. Timoshenko, P. Nazarov, F. Hohls, P. Mirovsky, B. Mackrodt, R. Dolata, T. Weimann, K. Pierz, H.W. Schumacher, Counting statistics for electron capture in a dynamic quantum dot, Phys. Rev. Lett. 110 (2013) 126803.
[258] L. Fricke, M. Wulf, B. Kaestner, F. Hohls, P. Mirovsky, B. Mackrodt, R. Dolata, T. Weimann, K. Pierz, U. Siegner, H.W. Schumacher, Self-referenced single-electron quantized current source, Phys. Rev. Lett. 112 (2014) 226803.
[259] N. Johnson, J.D. Fletcher, D.A. Humphreys, P. See, J.P. Griffiths, G.A.C. Jones, I. Farrer, D.A. Ritchie, M. Pepper, T.J.B.M. Janssen, M. Kataoka, Ultrafast voltage sampling using single-electron wavepackets, Appl. Phys. Lett. 110 (10) (2017) 102105, https://doi.org/10.1063/1.4978388.
[260] BIPM, The BIPM key comparison database (KCDB), Calibration and Measurement Capabilities – CMCs (Appendix C), DC current database. https://kcdb.bipm.org.
[261] D. Drung, C. Krause, Ultrastable low-noise current amplifiers with extended range and improved accuracy, IEEE Trans. Instrum. Meas. 66 (2017) 1425.
[262] D. Drung, C. Krause, U. Becker, H. Scherer, F. Ahlers, Ultrastable low-noise current amplifier: a novel device for measuring small electric currents with high accuracy, Rev. Sci. Instrum. 86 (2015) 024703.
[263] D. Drung, C. Krause, S.P. Giblin, S. Djordjevic, F. Piquemal, O. Séron, F. Rengnez, M. Götz, E. Pesel, H. Scherer, Validation of the ultrastable low-noise current amplifier as travelling standard for small direct currents, Metrologia 52 (2015) 756.
[264] W. Poirier, F. Lafont, S. Djordjevic, F. Schopfer, L. Devoille, A programmable quantum current standard from the Josephson and the quantum Hall effects, J. Appl. Phys. 115 (2014) 044509.
[265] I.M. Mills, P.J. Mohr, T.J. Quinn, B.N. Taylor, E.R. Williams, Redefinition of the kilogram: a decision whose time has come, Metrologia 42 (2005) 71–80.
[266] B. Kibble, A measurement of the gyromagnetic ratio of the proton by the strong field method, in: Atomic Masses and Fundamental Constants, vol. 5, Plenum Press, 1976, pp. 545–551.
[267] D. Haddad, F. Seifert, L.S. Chao, A. Possolo, D.B. Newell, J.R. Pratt, C.J. Williams, S. Schlamminger, Measurement of the Planck constant at the national institute of standards and technology from 2015 to 2017, Metrologia 54 (2017) 633.
[268] B.M. Wood, C.A. Sanchez, R.G. Green, J.O. Liard, A summary of the Planck constant determinations using the NRC Kibble balance, Metrologia 54 (2017) 399.
[269] M. Thomas, D. Ziane, P. Pinot, R. Karcher, A. Imanaliev, F.P.D. Santos, S. Merlet, F. Piquemal, P. Espel, A determination of the Planck constant using the LNE Kibble balance in air, Metrologia 54 (4) (2017) 468–480.
[270] F. Kuchar, R. Meisels, G. Weimann, W. Schlapp, Microwave Hall conductivity of the two-dimensional electron gas in GaAs–$Al_xGa_{1-x}As$, Phys. Rev. B 33 (1986) 2965.
[271] O. Viehweger, K.B. Efetov, Frequency-dependent deformation of the Hall plateaux, J. Phys. Condens. Matter 3 (1986) 1675.
[272] F. Delahaye, Accurate AC measurements of the quantized Hall resistance from 1 Hz to 1.6 kHz, Metrologia 31 (5) (1995) 367–373.
[273] B.P. Kibble, J. Schurr, A novel double-shielding technique for ac quantum Hall measurement, Metrologia 45 (2008) L25.
[274] F. Overney, B. Jeanneret, B. Jeckelmann, Effects of metallic gates on ac measurements of the quantum Hall resistance, IEEE Trans. Instrum. Meas. 52 (2003) 574.
[275] F.J. Ahlers, B. Jeannneret, F. Overney, J. Schurr, B.M. Wood, Compendium for precise ac measurements of the quantized Hall resistance, Metrologia 46 (2009) R1.
[276] F. Overney, B. Jeanneret, B. Jeckelmann, B.M. Wood, J. Schurr, The quantized Hall resistance: towards a primary standard of impedance, Metrologia 43 (2006) 409.
[277] J. Schurr, F.J. Ahlers, G. Hein, K. Pierz, The ac quantum Hall effect as a primary standard of impedance, Metrologia 44 (2007) 15.
[278] R. Haddad, Ph.D. thesis, George Washington University, Washington, DC, USA, 1969.
[279] D.L.H. Gibbings, A design for resistors of calculable a.c./d.c. resistance ratio, Proc. IEEE 110 (1963) 335.
[280] R.D. Cutkosky, Techniques for comparing four-terminal-pair admittance standards, J. Res. NBS 74C (1970) 63.
[281] F. Overney, B. Jeanneret, Impedance bridges: from Wheatstone to Josephson, Metrologia 55 (2018) S119.
[282] F. Overney, N.E. Flowers-Jacobs, B. Jeanneret, A. Rüfenacht, A.E. Fox, J.M. Underwood, A.D. Koffman, S.P. Benz, Josephson-based full digital bridge for high-accuracy impedance comparisons, Metrologia 53 (2016) 1045.
[283] S. Bauer, R. Behr, T. Hagen, O. Kieler, J. Lee, L. Palafox, J. Schurr, A novel two-terminal-pair pulse-driven Josephson impedance bridge linking a 10 nf capacitance standard to the quantized Hall resistance, Metrologia 54 (2017) 152.
[284] D.R. White, R. Galleano, A. Actis, H. Brixy, M.D. Groot, J. Dubbeldam, A.L. Reesink, F. Edler, H. Sakurai, R.L. Shepard, J.-C. Gallop, The status of Johnson noise thermometry, Metrologia 33 (4) (1996) 325, http://stacks.iop.org/0026-1394/33/i=4/a=6.
[285] J.B. Johnson, Thermal agitation of electricity in conductors, Nature 119 (1927) 50.
[286] J.B. Johnson, Thermal agitation of electricity in conductors, Phys. Rev. 32 (1928) 97–109, https://doi.org/10.1103/PhysRev.32.97, https://link.aps.org/doi/10.1103/PhysRev.32.97.
[287] S.P. Benz, J.M. Martinis, P.D. Dresselhaus, S.W. Nam, An ac Josephson source for Johnson noise thermometry, IEEE Trans. Instrum. Meas. 52 (2) (2003) 545–549, https://doi.org/10.1109/TIM.2003.811687.

[288] S.W. Nam, S.P. Benz, P.D. Dresselhaus, W.L. Tew, D.R. White, J.M. Martinis, Johnson noise thermometry measurements using a quantized voltage noise source for calibration, IEEE Trans. Instrum. Meas. 52 (2) (2003) 550–554, https://doi.org/10.1109/TIM.2003.811686.
[289] S.P. Benz, A. Pollarolo, J. Qu, H. Rogalla, C. Urano, W.L. Tew, P.D. Dresselhaus, D.R. White, An electronic measurement of the Boltzmann constant, Metrologia 48 (3) (2011) 142, http://stacks.iop.org/0026-1394/48/i=3/a=008.
[290] D.R. White, S.P. Benz, Constraints on a synthetic-noise source for Johnson noise thermometry, Metrologia 45 (1) (2008) 93, http://stacks.iop.org/0026-1394/45/i=1/a=013.
[291] N.E. Flowers-Jacobs, A. Pollarolo, K.J. Coakley, A.E. Fox, H. Rogalla, W.L. Tew, S.P. Benz, A Boltzmann constant determination based on Johnson noise thermometry, Metrologia 54 (5) (2017) 730, http://stacks.iop.org/0026-1394/54/i=5/a=730.
[292] C. Urano, K. Yamazawa, N.-H. Kaneko, Measurement of the Boltzmann constant by Johnson noise thermometry using a superconducting integrated circuit, Metrologia 54 (6) (2017) 847, http://stacks.iop.org/0026-1394/54/i=6/a=847.
[293] J. Qu, S.P. Benz, K. Coakley, H. Rogalla, W.L. Tew, R. White, K. Zhou, Z. Zhou, An improved electronic determination of the Boltzmann constant by Johnson noise thermometry, Metrologia 54 (4) (2017) 549, http://stacks.iop.org/0026-1394/54/i=4/a=549.
[294] J.E. Mooij, Y.V. Nazarov, Superconducting nanowires as quantum phase-slip junctions, Nat. Phys. 2 (2006) 169–172.
[295] C.H. Webster, J.-C. Fenton, T.T. Hongisto, S.P. Giblin, A.B. Zorin, P.A. Warburton, NbSi nanowire quantum phase-slip circuits: dc supercurrent blockade, microwave measurements, and thermal analysis, Phys. Rev. B 87 (2013) 144510, https://doi.org/10.1103/PhysRevB.87.144510.
[296] O.V. Astafiev, L.B. Ioffe, S. Kafanov, Y.A. Pashkin, K.Y. Arutyuno, D. Shahar, O. Cohen, J.S. Tsai, Nature 484 (2012) 355.
[297] S.E. de Graaf, S.T. Skacel, T. Hönigl-Decrinis, R. Shaikhaidarov, H. Rotzinger, S. Linzen, M. Ziegler, U. Hübner, H.-G. Meyer, V. Antonov, E. Il'ichev, A.V. Ustinov, A.Y. Tzalenchuk, O.V. Astafiev, Nat. Phys. 14 (2018) 590–594.
[298] M.R. Connolly, K.L. Chiu, S.P. Giblin, M. Kataoka, J.D. Fletcher, C. Chua, J.-P. Griffiths, G.A.C. Jones, V.I. Falko, C.G. Smith, T.J.B.M. Janssen, Gigahertz quantized charge pumping in graphene quantum dots, Nat. Nanotechnol. 8 (2013) 417.
[299] Y. Cao, V. Fatemi, S. Fang, K. Watanabe, T. Taniguchi, E. Kaxiras, P. Jarillo-Herrero, Unconventional superconductivity in magic-angle graphene superlattices, Nature 556 (2018) 43.
[300] S. Oh, The complete quantum Hall trio, Science 340 (2013) 150.
[301] F.D.M. Haldane, Model for a quantum Hall effect without Landau levels: condensed-matter realization of the parity anomaly, Phys. Rev. Lett. 61 (1988) 2015.
[302] M. Konig, S. Wiedmann, C. Brune, A. Roth, H. Buhmann, L.W. Molenkamp, X.-L. Qi, S.-C. Zhang, Quantum spin Hall insulator state in HgTe quantum wells, Science 318 (2007) 766.
[303] E.J. Fox, I.T. Rosen, Y. Yang, G.R. Jones, R.E. Elmquist, X. Kou, L. Pan, K.L. Wang, D. Goldhaber-Gordon, Part-per-million quantization and current-induced breakdown of the quantum anomalous Hall effect, Phys. Rev. B 98 (2018) 075145.
[304] C.-Z. Chang, W. Zhao, D.Y. Kim, H. Zhang, B.A. Assaf, D. Heiman, S.-C. Zhang, C. Liu, M.H.W. Chan, J.S. Moodera, High-precision realization of robust quantum anomalous Hall state in a hard ferromagnetic topological insulator, Nat. Mater. 14 (2015) 473.
[305] C.-Z. Chang, J. Zhang, X. Feng, J. Shen, Z. Zhang, M. Guo, K. Li, Y. Ou, P. Wei, L.-L. Wang, Z.-Q. Ji, Y. Feng, S. Ji, X. Chen, J. Jia, X. Dai, Z. Fang, S.-C. Zhang, K. He, Y. Wang, L. Lu, X.-C. Ma, Q.-K. Xue, Experimental observation of the quantum anomalous Hall effect in a magnetic topological, Science 340 (2013) 167.
[306] A.J. Bestwick, E.J. Fox, X. Kou, L. Pan, K.L. Wang, D. Goldhaber-Gordon, Precise quantization of the anomalous Hall effect near zero magnetic field, Phys. Rev. Lett. 114 (2015) 187201.
[307] M. Götz, K.M. Fijalkowski, E. Pesel, M. Hartl, T. Schreyeck, M. Winnerlein, S. Grauer, H. Scherer, K. Brunner, C. Gould, F.J. Ahlers, L.W. Molenkamp, Precision measurement of the quantized anomalous Hall resistance at zero magnetic field, Appl. Phys. Lett. 112 (2018) 072102.
[308] Joint research project SEQUOIA 17FUN04 of the European Metrology Programme for Innovation and Research (EMPIR), https://www.euramet.org/research-innovation.